DOCTORAL THESIS

UNIVERSITÀ DEGLI STUDI DI NAPOLI FEDERICO II

DIPARTIMENTO DI INGEGNERIA ELETTRONICA E DELLE TECNOLOGIE DELL'INFORMATIONE

PH.D COURSE IN INFORMATION TECHNOLOGY AND ELECTRICAL ENGINEERING

LIGHT-MATTER INTERACTION IN OPEN SYSTEMS: FROM NANOPARTICLES TO ATOMS

ROBERTO TRICARICO

Coordinator of the Ph.D course
Prof. Daniele RICCIO

Supervisor
Prof. Carlo FORESTIERE

Co-supervisor
Prof. Darrick CHANG

Alla mia stupenda famiglia,
origine e fonte inesauribile della mia forza

Abstract

In this doctoral thesis, we are going to present three selected topics on light-matter interaction in open systems. The activity of chapters 1 and 2 has been developed under the supervision of Prof. Carlo Forestiere at the University of Naples Federico II, in the Department of Information Technology and Electrical Engineering. Chapter 3 has been developed under the supervision of Prof. Darrick Chang at the Institute of Photonic Sciences in Castelldefels (Barcelona).
The three chapters can be read independently and their content is organized as follows.

In **chapter 1** we discuss the full-retarded light-scattering by homogeneous and isotropic nanoparticles, both in the plasmonic and in the dielectric case. We do it by introducing a modal expansion for the scattered field, whose basis elements do not depend on the material constituting the scattering object. As a matter of fact, by solving a permittivity independent auxiliary eigenvalue problem, it is possible to generate a set of *material independent modes* (MIMs) that are able to efficiently reconstruct the scattered field. The eigenvalues of the aforementioned problem are the *eigen-permittivities* of the nanoparticle and we say that a given MIM resonates when the corresponding eigenpermittivity approaches the permittivity of the scatterer. This *material picture* allows a clear separation of the roles played by shape and material in the scattering problem: the shape determines the basis elements of the expansion and the material weighs their contribution to the scattered pattern.

In **chapter 2** we provide a full-retarded quantum theory of the plasmon excitations in arbitrarily shaped metal nanoparticles and dimers. The continuous energy oscillation between the kinetic energy of the free electrons in the metal and the Coulomb energy associated to the charge accumulation on the surface of the nanoparticle, is the physical origin of the electrostatic

plasmon resonances. In the long-wavelength limit, the electron fluid motion oscillates without decaying and, providing a modal expansion for the electron displacement field, a canonical quantization procedure can be applied to define the *plasmons*: quasiparticles describing the collective motion of the electrons. When we exit the quasistatic regime and enter the full-retarded one, the nanoparticles start to radiate power to infinity and, as a consequence, these oscillations shift in energy and decay in time. At the quantum level, this process is described by the plasmon-photon interaction Hamiltonian that we rigorously derive and discuss in its various approximations. Eventually, we provide non-perturbative formulas to compute the radiative decay rate and the frequency shift of the plasmon excitations, valid for arbitrarily shaped metal nanoparticles and dimers in the full-retarded regime. These formulas do not use full-wave modal expansions but only electrostatic ones, and it makes them efficient tools to compute these quantities.

In **chapter 3** we discuss Rydberg ensembles of atoms, in the electromagnetic induced transparency setup, as a possible route to realize photon-photon nonlinear interaction. Thanks to the blockade mechanism provided by Rydberg atoms, a single photon is indeed able to saturate the atomic response of a considerably large portion of the ensemble, that appears opaque to a second incoming one. While the continuous wave response of such a medium was largely studied in the past, the pulse dynamics has been explored only recently. Interestingly, it has been observed that the transient light can be more antibunched than the CW one. Our goal is to understand what the physical origin of this behaviour is, and whether this effect actually reflects a stronger nonlinearity.

Publications

1. Carlo Forestiere, Giovanni Miano, Guglielmo Rubinacci, Antonello Tamburrino, Roberto Tricarico, and Salvatore Ventre. Volume Integral Formulation for the Calculation of Material Independent Modes of Dielectric Scatterers. *IEEE Transactions on Antennas and Propagation*, 66(5): 2505-2514, May 2018.

2. Carlo Forestiere, Giovanni Miano, Mariano Pascale, and Roberto Tricarico. A Full-Retarded Spectral Technique for the Analysis of Fano Resonances in a Dielectric Nanosphere. In Kamenetskii E., Sadreev A., Miroshnichenko A. (eds) Fano Resonances in Optics and Microwaves. *Springer Series in Optical Sciences, vol. 219*, Nov 2018.

3. Carlo Forestiere, Giovanni Miano, Mariano Pascale, and Roberto Tricarico. Directional scattering cancellation for an electrically large dielectric sphere. *Optics Letters*, 44(8):1972-1975, Apr 2019.

4. Carlo Forestiere, Giovanni Miano, Mariano Pascale, and Roberto Tricarico. Electromagnetic Scattering Resonances of Quasi-1-D Nanoribbons. *IEEE Transactions on Antennas and Propagation*, 67(8):5497-5506, Aug 2019.

5. Carlo Forestiere, Giovanni Gravina, Giovanni Miano, Mariano Pascale, and Roberto Tricarico. Electromagnetic modes and resonances of two-dimensional bodies. *Phys. Rev. B*, 99(15):155423, Apr 2019.

6. Pascale Mariano, Giovanni Miano, Roberto Tricarico, and Carlo Forestiere. Full-wave electromagnetic modes and hybridization in nanoparticle dimers. *Sci. Reports*, 9(1):14524, Oct 2019.

7. Carlo Forestiere, Giovanni Miano, Guglielmo Rubinacci, Antonello Tamburrino, Roberto Tricarico, and Salvatore Ventre. Magnetoqua-

sistatic resonances of small dielectric objects. *Phys. Rev. Research*, 2(1): 013158, Feb 2020.

8. Carlo Forestiere, Giovanni Miano, Mariano Pascale, and Roberto Tricarico. Quantum Theory of Radiative Decay Rate and Frequency Shift of Surface Plasmons in Arbitrarily Shaped Nanoparticles. *arXiv:2001.11926*, Jan 2020.

Chapter 1 is based on the activities of publications 1-7; Chapter 2 on the activity of publication 8; Chapter 3 contains unpublished work.

Contents

Chapter 1

Material independent modes for the electromagnetic scattering

Modal expansion in open resonators

The analysis and the engineering of the response of a nanostructure to an external electromagnetic field can be considerably improved through the development of a proper modal theory. The description in terms of modes and resonances, which solely depend on the inherent properties of the nanostructure, can indeed bring new deep insights into the physics of the scattering, compared to the direct solution of the scattering problem. On one side, it enables a rigorous understanding of the scattering patterns and of its interference phenomena in terms of well-identified modes. On the other side, it suggests how to tailor the excitation or which material is more suited to achieve a prescribed scattering feature, such as the maximization of a given modal response or the vanishing of the backscattering for example.

The modal description of closed electromagnetic systems, such as waveguides or cavities, is well-known and doesn't present ambiguities [1]. On the contrary, when the electromagnetic field is not confined to a bounded domain, as in the scattering case, this description is more challenging. Often the resonances of a body are found by illuminating it with a frequency-tunable probe field and checking the peaks of the scattered power spectrum. The corresponding electric field distributions are denoted as "modes". This oversimplified approach is flawed because not all the modes can be excited by a fixed incident field and exploiting moreover, a given peak can result from the interplay between more modes and, so, a correct analysis of the interference phenomena

cannot be done. Rigorous approaches are possible and differ one from the other according to the choice of the modes. The most used classes of modes are the quasi normal modes (QNMs) [2–4] and the characteristic modes [5]. The former modes depend on the material and on the geometry of the scatterer. They are not orthogonal in the usual sense and they diverge exponentially at large distances [3]. Because of that, a proper normalization process is needed [6, 7]. The latter depend on the frequency, on the material, and on the geometry of the scatterer. However, they are real and verify a weighted orthogonality.

Throughout this thesis chapter, we are going to introduce a third possible choice, the so called material independent modes (MIMs) [8, 9]. These modes do depend on the geometry of the scatterer and on the incident frequency, but do not depend on the material constituting the object. They are not orthogonal in the usual sense but verify a bi-orthogonality relation. Moreover, they do not diverge at infinity and, so, no normalization is needed. Over the years, MIMs have been calculated in the quasistatic limit [10–14], long wavelength limit [8], for the scalar Mie scattering [15]. They have been also derived within the quasistatic [16] and retarded [17] single dipole approximation. More recently, MIMs have been derived for the full-retarded vector scattering by homogeneous spheres [9], by coated spheres [18], by arbitrary shaped nanoparticles [19], by quasi-1D nanoribbons [20], by flat slabs [21], and by 2D bodies [22]. The MIM choice induces a natural separation of the roles played by the geometry and by the material in the scattering process: the shape dictates the modes; the material, which only appears in the coefficients, weights their contribution to the scattered field. Moreover, the coefficients of the expansion are simple rational functions of the permittivity and this has suggested a straightforward methodology to design the permittivity of the object to pursue a prescribed tailoring of the scattered field, including the cancellation of the backscattering, the suppression of a given multipolar order, and the maximization of the scattered field in the near-field zone [9, 23].

Furthermore, it has been also shown that the investigation of the eigenvalues (which essentially are *eigenpermittivities*) associated to the MIMs unveils important structural properties of the resonances [24], which suggest to subdivide the modes in two classes: the *plasmonic modes* and the *photonic modes*. When the linear dimension of the nanostructure is much smaller than the incident wavelength, no power is radiated to infinity, the modes do not decay in time, and the system can be described either by an electro-quasistatic approximation of the Maxwell's equations or by a magneto-quasistatic one. In this limit, the plasmonic modes present a quasi-electrostatic nature [25], while the

photonic modes a magneto-quasistatic one [26]; and they respectively resonate in plasmonic material and in high index dielectrics.

In this thesis chapter, the general definition of the MIM problem is introduced (section 1.1) and discussed in its main differences with the widely adopted quasi normal modes (section 1.1.1). A comparison between material independent modes and quasi normal modes is carried out in the one-dimensional case. Then, in sections 1.2 and 1.3, we devote our attention to the fundamental analytic case of the scattering by an isolated sphere. After that, in section 1.4, we apply the MIM method to the analysis of the scattering by a Si sphere and by a Ag sphere (section 1.4.1) and then to the material design to minimize the back-scattering (section 1.4.2). This chapter is mostly a redrafting of [19][1], with some additional insights.

1.1 Material independent modes

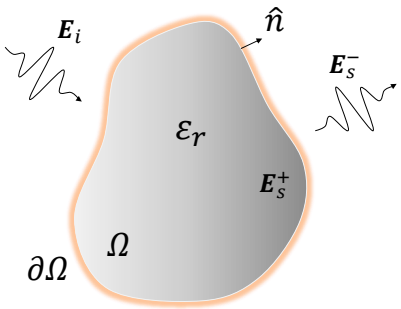

Figure 1.1: Sketch of the homogeneous scatterer.

We now consider the electromagnetic scattering by a homogeneous object occupying a regular region Ω of the space, with boundary $\partial\Omega$, sketched in figure 1.1. The object is excited by a time harmonic electromagnetic field incoming from infinity $\mathrm{Re}\left\{\mathbf{E}_i\left(\mathbf{r}\right)e^{-i\omega t}\right\}$. The medium is a non-magnetic isotropic

[1] Copyright (2018) by Springer Nature.

homogeneous dielectric with relative permittivity $\varepsilon_r(\omega)$, surrounded by vacuum. Let $\mathbf{E}_S^+$ and $\mathbf{E}_S^-$ be the scattered electric fields in Ω and $\mathbb{R}^3\backslash\bar{\Omega}$, respectively[2]. The Maxwell's equations lead to

$$\nabla^2\mathbf{E}_S^+ + k_0^2\varepsilon_r(\omega)\,\mathbf{E}_S^+ = k_0^2\left[1-\varepsilon_r(\omega)\right]\mathbf{E}_i \text{ in } \Omega, \tag{1.1}$$

$$\nabla^2\mathbf{E}_S^- + k_0^2\mathbf{E}_S^- = \mathbf{0} \qquad \text{in } \mathbb{R}^3\backslash\bar{\Omega}, \tag{1.2}$$

$$\hat{\mathbf{n}}\times\left(\mathbf{E}_S^- - \mathbf{E}_S^+\right) = \mathbf{0} \qquad \text{on } \partial\Omega, \tag{1.3}$$

$$\hat{\mathbf{n}}\times\left(\nabla\times\mathbf{E}_S^- - \nabla\times\mathbf{E}_S^+\right) = \mathbf{0} \qquad \text{on } \partial\Omega, \tag{1.4}$$

where $k_0 = \omega/c_0$, c_0 is the light velocity in vacuum and $\hat{\mathbf{n}}$ is the outgoing normal to $\partial\Omega$. Equations (1.1)-(1.4) have to be solved with the radiation conditions for the scattered field, namely the regularity and Silver-Müller condition at infinity:

$$\mathbf{E}_S^+ = o\left(\frac{1}{r}\right) \quad \nabla\times\mathbf{E}_S^+ = o\left(\frac{1}{r}\right), \quad \mathbf{E}_S^+ + \frac{1}{ik_0}\hat{\boldsymbol{r}}\times\nabla\times\mathbf{E}_S^+ = o\left(\frac{1}{r}\right), \tag{1.5}$$

which constraint the scattered field to be an outgoing wave. This problem has a unique solution if $\mathrm{Im}\{\varepsilon_r\} > 0$ [27].

This scattering problem is linear so it is useful to reduce it to an algebraic form. The idea that we are going to use can be well understood by looking at the following finite dimensional problem: $(A+\beta)\,x = b$, with A self-adjoint. It can be solved directly, by writing $x = (A+\beta)^{-1}\,b$, or it can be solved in a "modal" way. That is to say, we first solve the eigenproblem $-Ax = \lambda x$. Then, said $\{x_i\}_i$ a basis of orthogonal eigenvectors and $\{\lambda_i\}_i$ the corresponding eigenvalues, we derive the following expansion for the solution:

$$x = \sum_i c_i x_i = \sum_i \frac{1}{\beta-\lambda_i}\frac{\langle x_i|b\rangle}{\langle x_i|x_i\rangle}\,x_i. \tag{1.6}$$

We proceed in a similar way for the scattering problem and, instead of solving (1.1)-(1.5) directly, we introduce the following auxiliary eigenvalue problem:

$$-k_0^{-2}\,\nabla^2\mathbf{C} = \gamma\mathbf{C} \qquad \text{in } \Omega, \tag{1.7}$$

with the requirement for the eigenmodes $\mathbf{C}$ to verify the (1.2)-(1.5)[3]. The spectrum of the operator $-\nabla^2$ in Ω with the conditions (1.2)-(1.5) is countably

[2] $\bar{\Omega}$ is the closure of Ω.

[3] Let us notice that this problem can be written in a more compact and comfortable form by introducing the exterior outgoing Calderón operator $\mathcal{C}^e$ [27]. It takes the tangential component

infinite, we denote it with $\{\gamma_n\}_{n\in\mathbb{N}}$, and it is made of complex eigenvalues with $\mathrm{Im}\{\gamma_n\} < 0$. As often happens when we deal with open systems, the operator is not self-adjoint. However, it is possible to reach an expansion like (1.6) observing that the conditions (1.2)-(1.5) make the Laplacian operator symmetric; and so that the following statement holds: given two eigenmodes $\mathbf{C}_r$ and $\mathbf{C}_s$ corresponding to two eigenvalues γ_r and γ_s, even if they are not orthogonal in the usual sense, i.e. $\langle \mathbf{C}_r, \mathbf{C}_s\rangle_\Omega \neq 0$, where

$$\langle \mathbf{A}, \mathbf{B}\rangle_V = \iiint_V \mathbf{A}^* \cdot \mathbf{B} dV, \tag{1.11}$$

they verify [9]:

$$\langle \mathbf{C}_r^*, \mathbf{C}_s\rangle_\Omega = 0 \qquad \text{if } \gamma_r \neq \gamma_s. \tag{1.12}$$

Thus, the solution of the problem (1.1)-(1.5) can be expressed in the form:

$$\mathbf{E}_S^+ = (1-\varepsilon_r)\sum_{n=1}^{\infty} \frac{1}{\varepsilon_r - \gamma_n} \frac{\langle \mathbf{C}_n^*, \mathbf{E}_i\rangle_\Omega}{\langle \mathbf{C}_n^*, \mathbf{C}_n\rangle_\Omega} \mathbf{C}_n. \tag{1.13}$$

The eigenvalues γ_n and the eigenfunctions $\mathbf{C}_n$ are permittivity (i.e. material) independent, they only depend on the geometry of the scatterer and on the frequency we are working at. Thus, from this expansion we can appreciate the different roles played by the geometry and by the material in the scattering problem: the geometry dictates the shape of the available scattering patterns through the $\mathbf{C}_n$; the material weights the contribution of each pattern to the total scattered field. And it is worth noticing that it appears in the multiplicative factors only in the simple form: $1/(\varepsilon_r - \gamma_n)$. It gives us the chance to define a natural notion of *material resonance* according to which, a given material independent mode $\mathbf{C}_r$ resonates when the relative permittivity of the object ε_r approaches the corresponding eigenvalue γ_n. In particular, assuming a material of ε_r arbitrarily close to a given γ_n and an incident field $\mathbf{E}_i$ able to excite

---

of the scattered electric field on $\partial\Omega$, i.e. $\hat{\mathbf{n}} \times \mathbf{E}_S^-\big|_{\partial\Omega}$, where $\mathbf{E}_S^-$ is solution of the scattering problem, and returns the tangential component of its curl $\hat{\mathbf{n}} \times \nabla \times \mathbf{E}_S^-\big|_{\partial\Omega}$, ensuring that the (1.2)-(1.5) are verified:

$$\mathcal{C}^e\left\{\hat{\mathbf{n}} \times \mathbf{E}_S^-\big|_{\partial\Omega}\right\} = \hat{\mathbf{n}} \times \nabla \times \mathbf{E}_S^-\big|_{\partial\Omega}. \tag{1.8}$$

This operator, thus, folds the entire problem inside the bounded domain Ω:

$$-k_0^{-2}\nabla^2\mathbf{C} = \gamma\mathbf{C} \qquad \text{in } \Omega \tag{1.9}$$

$$\mathcal{C}^e\{\hat{\mathbf{n}} \times \mathbf{C}\} = \hat{\mathbf{n}} \times \nabla \times \mathbf{C} \qquad \text{on } \partial\Omega. \tag{1.10}$$

$\mathbf{C}_n$ (we need $\langle \mathbf{C}_n^*, \mathbf{E}_i \rangle_\Omega \neq 0$), the scattering response will be dominated by the single mode $\mathbf{C}_n$.

Because of that, the eigenvalues γ_n are indeed *eigen-permittivities* and it is important to study what are their real and imaginary parts. As a matter of fact, it will tell us whether it is possible or not, for a given material, to match a particular resonance condition. It can be proved that [9]:

$$\gamma_n = \frac{1}{\|\mathbf{C}_n\|_\Omega^2} \left[\frac{\|\nabla \times \mathbf{C}_n\|_{\mathbb{R}^3}^2}{k_0^2} - \|\mathbf{C}_n\|_{\mathbb{R}^3 \setminus \bar{\Omega}}^2 - i \oiint_{S_\infty} \frac{|\mathbf{C}_n|^2}{k_0} \mathrm{dS} \right], \tag{1.14}$$

where $\|\mathbf{A}\|_V^2 = \langle \mathbf{A}, \mathbf{A} \rangle_V$, and S_∞ is $\lim_{R \to \infty} S_R$, where S_R is a sphere of radius R containing the scatterer. From here we see that $\mathrm{Re}\{\gamma_n\}$ does not have a definite sign while $\mathrm{Im}\{\gamma_n\}$ is negative and proportional to the contribution of the corresponding mode to the power radiated to infinity. The undefined sign of $\mathrm{Re}\{\gamma_n\}$ corresponds to the existence of both modes able to resonate in plasmonic materials, the *plasmonic modes* ($\mathrm{Re}\{\gamma_n\} < 0$), and modes able to resonate in dielectrics, the *photonic modes* ($\mathrm{Re}\{\gamma_n\} > 0$). $\mathrm{Im}\{\gamma_n\} < 0$ is the necessary condition to lose the uniqueness of the solution in the scattering probem. From the physical point of view, it implies that, in the retarded regime, no passive material can perfectly match the condition $\varepsilon_r = \gamma_n$, and so we can only aim to minimize the distance between ε_r and γ_n. Let's observe that the above definition of plasmonic and photonic modes can sound a bit unsatisfactory if we observe that $\mathrm{Re}\{\gamma_n\}$ can change sign as the frequency varies, while the fundamental nature of the corresponding mode doesn't. So, to give a less ambiguous classification of the modes, we can look at their behaviour in the quasistatic limit. When the incident wavelength is much bigger than the linear dimension of the object, the modes do not radiate power to infinity anymore and, thus, the imaginary part of γ_n goes to zero and the resonance condition can be, at least in theory, perfectly matched. Therefore, the classification of the modes is refined as follows: the ones that at the quasistatic limit resonates in plasmonic material and the ones that resonate in high index dielectrics. Both types of resonances can be computed by solving a proper quasistatic problem that predicts their existence and that is extremely simpler than the full-wave one. The plasmonic resonances have the well-known electroquasistatic origin, deeply investigated in plasmonics over time [25]. The high-index dielectric resonances have a magneto-quasistatic origin, that only very recently has been highlighted [26]. This magneto-quasistatic picture is novel and could play an important role in the future developments of the scattering theory, since high-index dielectric are receiving great attention in the recent

period as a possible alternative to the plague of the losses in the metals. The magneto-quasistatic problem represents a huge simplification in the study of these resonances, compared to the full-wave methods today used.

1.1.1 Differences between material independent modes and quasi normal modes

Since the open systems are often investigated by using quasi normal modes [2, 4], it is instructive to highlight the major differences between QNMs and MIMs.

The QNMs are solution of the following eigenvalue problem:

$$-\boldsymbol{\nabla}^2\mathbf{F}^+ = \frac{\xi^2}{c^2}\varepsilon_r\mathbf{F}^+ \qquad \text{in } \Omega, \tag{1.15}$$

$$-\boldsymbol{\nabla}^2\mathbf{F}^- = \frac{\xi^2}{c^2}\mathbf{F}^- \qquad \text{in } \mathbb{R}^3\backslash\bar{\Omega}, \tag{1.16}$$

$$\hat{\mathbf{n}}\times\left(\mathbf{F}^- - \mathbf{F}^+\right) = \mathbf{0} \qquad \text{on } \partial\Omega, \tag{1.17}$$

$$\hat{\mathbf{n}}\times\left(\boldsymbol{\nabla}\times\mathbf{F}^- - \boldsymbol{\nabla}\times\mathbf{F}^+\right) = \mathbf{0} \qquad \text{on } \partial\Omega, \tag{1.18}$$

with the Silver-Müller conditions at infinity, namely

$$\mathbf{F}^- + \frac{c}{i\xi}\hat{\mathbf{r}}\times\boldsymbol{\nabla}\times\mathbf{F}^- = o\left(\frac{1}{r}\right), \tag{1.19}$$

where the eigenvalues ξ constitute a countable infinite set.

The two problems are somehow dual. In the MIM case, the eigenmodes and the eigenvalues depend upon the shape and the frequency but do not depend on the material. In the QNM case, the eigenmodes and the eigenvalues depend upon the shape and the material but do not depend on the frequency. The two modal approaches respectively corresponds to the following two different pictures of the scattering problem: the *material picture*, where the frequency is fixed and the material properties are studied; the *frequency picture* where the material is fixed and the frequency response is analyzed. One approach could be better than the other according to the needs. For example, the dependence of ξ and $\mathbf{F}$ on the permittivity makes the QNMs unattractive for the material design of an object to achieve a prescribed tailoring of the scattered field. This is because the expansion in terms of QNMs of the electric field solution of the inhomogeneous scattering problem is a very complicated function of the permittivity. On the contrary, once that the material constituting the nanostructure is chosen, a frequency study is straightforward using the

QNM approach while it is more challenging with the MIM method. However, if our purpose is the complete understanding of the nanostructure both from the material point of view and from the frequency behaviour, the MIMs appear much more convenient than the QNMs. Indeed, while in the MIM case, to have a complete description in frequency, we have to provide a modal expansion for the half-axis $\omega > 0$, in the QNM case, to have a complete description from the material point of view, we have to do it for the half-plane $\mathrm{Im}\{\varepsilon_r\} > 0$.

Mowever, there is another important difference to mention: in the QNM case, the spectral parameter ξ appears in the Silver-Müller conditions at infinity, while in the MIM case the spectral parameter γ doesn't. This consideration, together with the property $\mathrm{Im}\{\xi_n\} > 0$, has the consequence that the QNMs diverge exponentially at large distances [3]. Therefore, to be used in any practical application, they need to be normalized [7]. The problem of the normalization of the QNMs, which essentially coincides with the problem of finding the coefficients of the expansion for the scattered field, is an active research area and we don't want to get into details [4]. We will simply show an easy one-dimensional example of it. However, it is crucial to point out that, on the contrary, the material independent modes are bounded and approach zero at infinity. Thus, no normalization is needed. This is a direct consequence of the fact that, in the MIM case, the spectral parameter does not appear in the radiation condition at infinity. As a matter of fact, even if it is true that the differential operator itself admits the dual interpretation material/frequency, this is absolutely false for the radiation condition. Indeed, it contains only the frequency, since the scatterer in bounded in space. This particular reason is already enough to make the material picture favourite over the frequency one, at least in the case of homogeneous and isotropic objects.

Eventually, it is important to observe that the MIMs cannot be applied in the general case of a non-homogeneous medium, i.e. $\varepsilon_r(\mathbf{r})$, unless it does not have a particular one-parameter dependence. On the other side, the QNMs are perfect for these kind of situations and the normalization is the prize to pay, in order to provide a modal expansion of such non-homogeneous open systems.

One-dimensional case

In order to exemplify the differences between QNMs and MIMs, we consider the one-dimensional problem of the electromagnetic scattering by a one-dimensional slab[4].

[4]The QNM case was derived in [4].

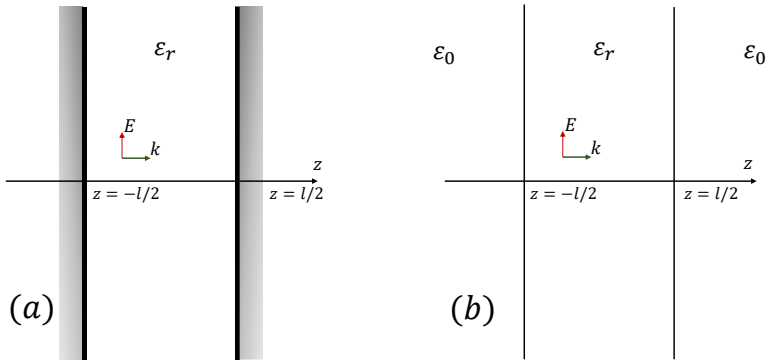

Figure 1.2: Sketch of the one-dimensional case. Closed resonator in (a), open resonator in (b).

Closed resonator. First, we consider the case of a dielectric slab of permittivity ε_r, bounded at $z = \pm l/2$ by two infinite perfect electric conductors (ideal mirrors). The slab is illuminated by a transverse incident field propagating along the z-axis and linearly polarized along the x-axis: $\mathbf{E}_i = E_i\hat{\boldsymbol{x}}$. We denote the total field as $\mathbf{E}_{tot} = E_{tot}\hat{\boldsymbol{x}}$ and the scattered field as $\mathbf{E}_s = E_s\hat{\boldsymbol{x}} = \mathbf{E}_{tot} - \mathbf{E}_i$. For $z \in [-l/2, +l/2]$, the incident field is solution of the Maxwell's equation in vacuum:

$$\frac{d^2E_i}{dz^2} + \frac{\omega^2}{c_0^2}E_i = 0, \tag{1.20}$$

while the total field E_{tot} verifies:

$$\begin{aligned} &\frac{d^2E_{tot}}{dz^2} + \varepsilon_r\frac{\omega^2}{c_0^2}E_{tot} = 0 \\ &E_{tot}|_{z=\pm l/2} = 0, \end{aligned} \tag{1.21}$$

and thus E_s is obtained by solving the following problem:

$$\begin{aligned} &\frac{d^2E_s}{dz^2} + \varepsilon_r\frac{\omega^2}{c_0^2}E_s = (1-\varepsilon_r)\frac{\omega^2}{c_0^2}E_i, \\ &E_s|_{z=\pm l/2} = 0. \end{aligned} \tag{1.22}$$

In the **material picture**, we look for the values of permittivity ε_r of the slab in correspondence of which the problem (1.22) has source-free solutions. Thus, we consider the following auxiliary eigenvalue problem:

$$\begin{aligned} &-\frac{1}{k_0^2}\frac{d^2C_n}{dz^2} = \gamma_n C_n \\ &C_n|_{z=\pm l/2} = 0. \end{aligned} \tag{1.23}$$

The eigenvalues constitute a countable infinite set $\{\gamma_n = n\pi/x\}_n$, where $x = 2\pi l/\lambda$ is the size parameter of the slab; while the corresponding even and odd eigenmodes are sinusoidal functions:

$$\{\cos(x\sqrt{\gamma_n}z/l)\}_{n\in\mathbb{N}_e}\,,\ \{\sin(x\sqrt{\gamma_n}z/l)\}_{n\in\mathbb{N}_o}\,. \tag{1.24}$$

We can explicitly notice how these modes do not depend on ε_r.

The modes are, in this case, orthogonal in the usual sense

$$\langle C_n, C_m\rangle = \int_{-l/2}^{l/2} C_n(z)C_m(z)dz = \delta_{n,m}\langle C_n, C_n\rangle \tag{1.25}$$

and, thanks to that, we can derive the following expansion for the solution of the non-homogeneous problem (1.22):

$$E_s = (1-\varepsilon_r)\sum_n \frac{1}{\varepsilon_r - \gamma_n}\frac{\langle C_n, E_i\rangle}{\langle C_n, C_n\rangle}C_n. \tag{1.26}$$

In the above expression the dependence on the material and on the geometry are separated.

In the **frequency picture** we look for the values of frequency in correspondence of which the problem (1.22) has non-trivial source free solution. Thus, we consider the following eigenvalue problem:

$$\begin{aligned} &-\frac{c_0^2}{\varepsilon_r}\frac{d^2E_i}{dz^2} = \xi_n^2 C_n, \\ &C_n|_{\pm l/2} = 0, \end{aligned} \tag{1.27}$$

whose eigenvalues are $\left\{\xi_n = \frac{n}{2}\frac{1}{R}\omega_c\right\}_n$ where $\omega_c = 2\pi c_0/l$ is the characteristic frequency, and whose even and odd eigenmodes are:

$$\left\{\cos\left(2\pi\sqrt{\varepsilon_n}\frac{\xi_n}{\omega_c}z/l\right)\right\}_{n\in\mathbb{N}_e},\ \left\{\sin\left(2\pi\sqrt{\varepsilon_n}\frac{\xi_n}{\omega_c}z/l\right)\right\}_{n\in\mathbb{N}_o}. \tag{1.28}$$

Now, the orthogonality of the modes:

$$\langle F_n, F_m \rangle = \int_{-l/2}^{l/2} F_n(z) F_m(z) dz = \delta_{n,m} \langle F_n, F_n \rangle \tag{1.29}$$

brings to this other expansion:

$$E_s = (1 - \varepsilon_r) \sum_n \frac{\omega^2}{\xi_n^2 - \omega^2} \frac{\langle F_n, E_i \rangle}{\langle F_n, F_n \rangle} F_n. \tag{1.30}$$

In a closed resonator, the operator is self-adjoint and the two pictures are perfectly equivalent.

Open resonator. We now remove the two mirrors and consider the ε_r slab embedded in free-space. The electromagnetic field is no longer confined within the resonator but can leak outsize. Also in this case, we assume a transverse electromagnetic field.

The equations for E_{tot}, E_i and E_s inside the slab are the same as before, while outside the fields simply propagate $\left(d^2/dz^2 + \omega^2/c_0^2\right) = 0$. Then, at $z = \pm l/2$ the tangential components of the fields have to be continuous.

$$\frac{d^2 E_s^+}{dz^2} + \varepsilon_r \frac{\omega^2}{c_0^2} E_s^+ = (1 - \varepsilon_r) \frac{\omega^2}{c_0^2} E_i \quad \text{when } |z| < l/2 \tag{1.31}$$

$$\frac{d^2 E_s^-}{dz^2} + \frac{\omega^2}{c_0^2} E_s^- = 0 \quad \text{when } |z| > l/2 \tag{1.32}$$

$$E_s^{(+)}\Big|_{\pm l/2} = E_s^{(-)}\Big|_{z=\pm l/2}. \tag{1.33}$$

This problem can be folded from the z-axis to the segment $[-l/2, l/2]$, and re-written in the following compact form[5]:

$$\frac{d^2 E_s^+}{dz^2} + \varepsilon_r \frac{\omega^2}{c_0^2} E_s^+ = (1 - \varepsilon_r) \frac{\omega^2}{c_0^2} E_i \qquad \text{when } |z| < l/2 \tag{1.34}$$

$$E_s^+\big|_{\pm l/2} = \mp \frac{c_0}{i\omega} \left.\frac{dE_s^+}{dz}\right|_{z=\pm l/2}. \tag{1.35}$$

In the **material picture** we assume the frequency assigned, and we look for the values of permittivity in correspondence of which the problem (1.34-1.35)

[5]Let us notice that this is an example of a concrete use of the Calderon operator, which in this case takes the form (1.35).

has non trivial solution. We solve the auxiliary eigenvalue problem:

$$-\frac{1}{k_0^2}\frac{d^2C_n}{dz^2} = \gamma_n C_n \quad \text{when } |z| < l/2 \tag{1.36}$$

$$C_n|_{\pm l/2} = \mp\frac{1}{ik_0}\left.\frac{dC_n}{dz}\right|_{z=\pm l/2}. \tag{1.37}$$

The eigenpermittivity are the solution of the equation:

$$e^{ik_0\sqrt{\gamma_n}2l_c} = \Gamma^2(\gamma_n) \tag{1.38}$$

where $\Gamma = \frac{1-\sqrt{\varepsilon_r}}{1+\sqrt{\varepsilon_r}}$, whose even and odd eigenmodes are:

$$C_{n\in\mathbb{N}_e} = \begin{cases} \cos\left(\sqrt{\gamma_n}\frac{x}{2}\right)e^{+ix\left(\frac{z}{l}+\frac{1}{2}\right)}, & \text{for } z < -l/2 \\ \cos\left(\sqrt{\gamma_n}\frac{x}{2}\right), & \text{for } |z| < -l/2 \\ \cos\left(\sqrt{\gamma_n}\frac{x}{2}\right)e^{+ix\left(\frac{z}{l}-\frac{1}{2}\right)} & \text{for } z > l/2 \end{cases} \tag{1.39}$$

$$C_{n\in\mathbb{N}_o} = \begin{cases} -\sin\left(\sqrt{\gamma_n}\frac{x}{2}\right)e^{-ix\left(\frac{z}{l}+\frac{1}{2}\right)}, & \text{for } z < -l/2 \\ \sin\left(\sqrt{\gamma_n}\frac{x}{2}\right), & \text{for } |z| < -l/2 \\ \sin\left(\sqrt{\gamma_n}\frac{x}{2}\right)e^{+ix\left(\frac{z}{l}-\frac{1}{2}\right)} & \text{for } z > l/2 \end{cases}, \tag{1.40}$$

where we have introduced the size parameter $x = 2\pi l/\lambda$. These modes are bounded for all $z \in \mathbb{R}$ and, thanks to the following relation:

$$\langle C_n^*, C_m\rangle = \int_{-l/2}^{l/2} C_n C_m dz = \langle C_n^*, C_n\rangle\delta_{n,m}, \tag{1.41}$$

we obtain the expansion:

$$E_s = (1-\varepsilon_r)\sum_n \frac{1}{\varepsilon_r - \gamma_n}\frac{\langle C_n^*, E_i\rangle}{\langle C_n^*, C_n\rangle}C_n. \tag{1.42}$$

The associated *material resonance* of a given mode n corresponds to choose an ε_r that minimazes the quantity $|(\varepsilon_r - \gamma_n)/(1-\varepsilon_r)|$.

If we now approach the problem in the **frequency picture**, the following eigenvalue problem has to be solved:

$$-\frac{c_0^2}{\varepsilon_r}\frac{d^2C_n}{dz^2} = \xi_n^2 C_n \quad \text{when } |z| < l/2 \tag{1.43}$$

$$C_n|_{\pm l/2} = \mp\frac{c_0}{i\xi_n}\left.\frac{dC_n}{dz}\right|_{z=\pm l/2}, \tag{1.44}$$

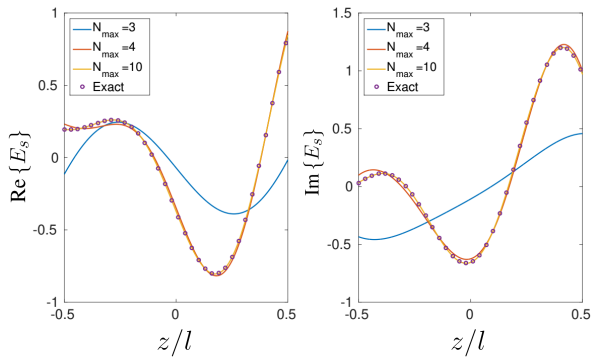

Figure 1.3: Electric field scattered by a dielectric slab of thickness l and $\varepsilon_r = 1.5$, assuming an incident wavelength of $\lambda = l$. The transverse excitation has unitary intensity. The MIM expansion using 3, 4, and 10 modes is compared with the exact solution.

and the eigenvalues ξ_n enter in the boundary condition.
Its eigenmodes are:

$$F_{n\in\mathbb{N}_e} = \begin{cases} \cos\left(\pi\frac{\xi_n}{\omega_0}\sqrt{\varepsilon_r}\right) e^{+i2\pi\frac{\xi_n}{\omega_c}\left(\frac{z}{l}+\frac{1}{2}\right)} & \text{for } z < -l/2 \\ \cos\left(2\pi\frac{\xi_n}{\omega_c}\sqrt{\varepsilon_r}\frac{z}{l}\right) & \text{for } |z| < l/2 \\ \cos\left(\pi\frac{\xi_n}{\omega_0}\sqrt{\varepsilon_r}\right) e^{-i2\pi\frac{\xi_n}{\omega_c}\left(\frac{z}{l}-\frac{1}{2}\right)} & \text{for } z > l/2, \end{cases} \tag{1.45}$$

$$F_{n\in\mathbb{N}_o} = \begin{cases} -\sin\left(\pi\frac{\xi_n}{\omega_0}\sqrt{\varepsilon_r}\right) e^{+i2\pi\frac{\xi_n}{\omega_c}\left(\frac{z}{l}+\frac{1}{2}\right)} & \text{for } z < -l/2 \\ \sin\left(2\pi\frac{\xi_n}{\omega_c}\sqrt{\varepsilon_r}\frac{z}{l}\right) & \text{for } |z| < l/2 \\ \sin\left(\pi\frac{\xi_n}{\omega_0}\sqrt{\varepsilon_r}\right) e^{-i2\pi\frac{\xi_n}{\omega_c}\left(\frac{z}{l}-\frac{1}{2}\right)} & \text{for } z > l/2. \end{cases} \tag{1.46}$$

Since ξ_n is complex and $\mathrm{Im}\{\xi_n\} > 0$, they are unbounded. So, in order to provide a proper expansion on the scattered field an extra-step, compared to the MIM case, has to be done. Using the Lorentz reciprocity principle, we can derive the following orthogonal relation [4]:

$$\int_{-l/2}^{l/2} \varepsilon_0\varepsilon_r F_n F_m - \mu_0 H_n H_m dz = 0 \quad \text{for } n \neq m, \tag{1.47}$$

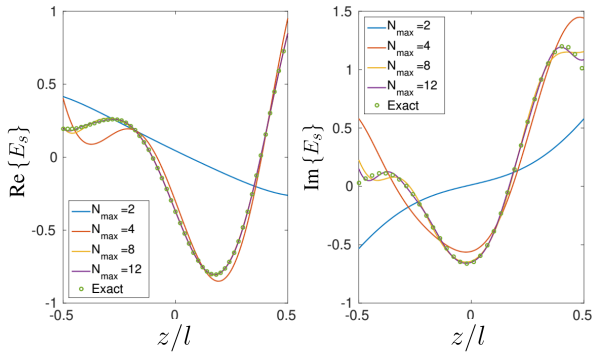

Figure 1.4: Electric field scattered by a dielectric slab of thickness l and $\varepsilon_r = 1.5$, assuming an incident wavelength of $\lambda = l$. The transverse excitation has unitary intensity. The QNM expansion using 2, 4, 8, and 12 modes is compared with the exact solution.

where $H_n = -\frac{i}{\omega\mu_0}\partial_z F_n$ is the magnetic field associated to the eigenmode F_n. Using this property, it is possible to derive the following expansion for the scattered field [4]:

$$E_s = (1-\varepsilon_r)\sum_n \frac{\omega}{\omega-\xi_n}\left(\int_{-l/2}^{l/2} E_i F_n dz\right) F_n. \tag{1.48}$$

The *resonance frequency* of a given mode n is the $\omega \in \mathbb{R}$ minimizing the quantity $|(\omega-\xi_n)/\omega|$.

In figures 1.3 and 1.4 we study the scattered electric field by a dielectric slab of thickness l and permittivity $\varepsilon_r = 1.5$, when an incident field of wavelength $\lambda = l$ is propagating. The transverse excitation has unitary intensity. In figure 1.3, we compare the MIM expansion truncating the number of modes up to $N_{max} = 3,\ ,4,$ and 10, with the direct (analytic) solution of the scattering problem and we find that it is perfectly satisfactory already for $N_{max} = 10$. In figure 1.4, we compare the QNM expansion using 2, 4, 8, and 12 modes with the exact solution. It is apparent that, by increasing the number of modes in the representation, the agreement with the exact solution improves. Nevertheless, it is worth to point out that, even by using $N_{max} = 12$ basis functions, there is still disagreement on the slab boundaries between the exact solution and the QNM expansion. Therefore, it appears, in this simple example, that the MIMs are more suitable for the representation of the scattered field than

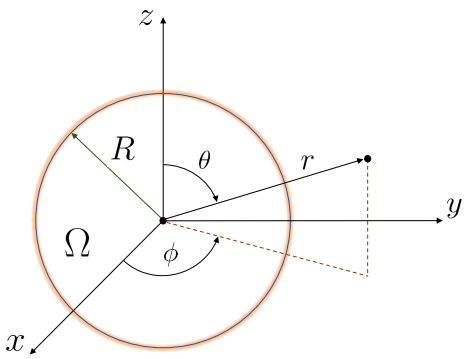

Figure 1.5: Spherical coordinate system centred on the sphere of size parameter x occupying the region Ω. We denote with r the radial distance, and with θ and ϕ the polar and azimuthal angles, respectively.

the QNMs quasi-normal-modes, since they guarantee the convergence to the exact solution with a minor number of modes.

1.2 Scattering by a sphere

We now apply this theory to the most representative and investigated scenario within the study of the scattering by nanoparticles: the scattering by a single sphere. Thus, let's assume that the region Ω is a sphere of radius R, sketched in figure 1.5, with size parameter $x = 2\pi\, R/\lambda$, where λ is the incident wavelength. We can write the material independent modes inside Ω as expansions of vector spherical wave functions (VSWFs are defined in Appendix A) [28]:

$$\mathbf{C}\left(\mathbf{r}\right) = \sum_{n=1}^{\infty}\sum_{m=0}^{n}\Big\{C_{emn}\mathbf{M}^{(1)}_{emn}\left(\sqrt{\gamma}k_0\mathbf{r}\right) + C_{omn}\mathbf{M}^{(1)}_{omn}\left(\sqrt{\gamma}k_0\mathbf{r}\right) + D_{emn}\mathbf{N}^{(1)}_{emn}\left(\sqrt{\gamma}k_0\mathbf{r}\right) + D_{omn}\mathbf{N}^{(1)}_{omn}\left(\sqrt{\gamma}k_0\mathbf{r}\right)\Big\}, \quad (1.49)$$

where the subscripts e and o denote even and odd, and the superscript (1), appended to the VSWFs, denotes that the radial dependence is given by the

Bessel function $j_n^{(1)}(\cdot)$, which are regular at the origin. Their expansion it the external region $\mathbb{R}^3\backslash\bar{\Omega}$ can be written as:

$$\mathbf{C}(\mathbf{r}) = \sum_{n=1}^{\infty}\sum_{m=0}^{n}\Big\{B_{emn}\mathbf{M}_{emn}^{(3)}(k_0\mathbf{r}) + B_{omn}\mathbf{M}_{omn}^{(3)}(k_0\mathbf{r}) + A_{emn}\mathbf{N}_{emn}^{(3)}(k_0\mathbf{r}) + A_{omn}\mathbf{N}_{omn}^{(3)}(k_0\mathbf{r})\Big\}, \quad (1.50)$$

where the superscript (3), appended to the VSWFs, denotes that the radial dependence is given by the Hankel function $h_n^{(1)}(\cdot)$, which satisfies the Silver-Müller condition at infinity.

By enforcing the continuity of the tangential components of $\mathbf{C}$ and $\boldsymbol{\nabla}\times\mathbf{C}$ on the surface of the sphere and exploiting the orthogonality of the VSWFs, we derive the eigenvalues and the eigenvectors of the problem. The former are an infinite countable set which is union of two subsets $\{\alpha_{nl}\}_{(n,l)\in\mathbb{N}^2}$ and $\{\beta_{nl}\}_{(n,l)\in\mathbb{N}^2}$, whose computation is traced back to the problem of finding the roots of two classes of power series. The procedure and the corresponding power series can be found in [19]. The eigenspaces corresponding to the eigenvalues α_{nl} and β_{nl} are spanned by the eigenfunctions:

$$\mathbf{C}_{\substack{e\\o}pmnl}^{(\alpha)} = \begin{cases} \mathbf{N}_{\substack{e\\o}mn}^{(1)}\left(\sqrt{\alpha_{nl}}k_0\mathbf{r}\right) & \mathbf{r}\in\Omega \\ \frac{\sqrt{\alpha_{nl}}j_n\left(\sqrt{\alpha_{nl}}x\right)}{h_n^{(1)}(x)}\mathbf{N}_{pmn}^{(3)}(k_0\mathbf{r}) & \mathbf{r}\in\mathbb{R}^3\backslash\bar{\Omega} \end{cases}, \quad (1.51)$$

$$\mathbf{C}_{\substack{e\\o}pmnl}^{(\beta)} = \begin{cases} \mathbf{M}_{\substack{e\\o}mn}^{(1)}\left(\sqrt{\beta_{nl}}k_0\mathbf{r}\right) & \mathbf{r}\in\Omega \\ \frac{j_n\left(\sqrt{\beta_{nl}}x\right)}{h_n^{(1)}(x)}\mathbf{M}_{pmn}^{(3)}(k_0\mathbf{r}) & \mathbf{r}\in\mathbb{R}^3\backslash\bar{\Omega} \end{cases}. \quad (1.52)$$

The modes $\mathbf{C}_{pmnl}^{(\alpha)}$ have no radial magnetic field component and are therefore called *electric type* or TM modes. Vice versa the modes $\mathbf{C}_{pmnl}^{(\beta)}$ have no radial electric field component and are denoted as *magnetic type* or TE modes. The modal indices p, m, n, l have the following meaning. The subscript $p\in\{e,o\}$ distinguishes between even and odd modes with respect to the azimuthal dependence. The numbers $n\in\mathbb{N}$ and $0\le m\le n$ define the angular dependence of the mode: m defines the number of oscillations along the azimuth, n is associated with the number of lobes of the mode amplitude at any given radial distance. In particular, the modes with $n=1$ are the dipolar modes, those with $n=2$ are the quadrupolar modes, and so on. The mode number $l\in\mathbb{N}$ gives the number of maxima of the mode amplitude along the radial direction inside

the sphere. We denote the electric and magnetic modes as *fundamental* when $l = 1$, and as *higher order* modes when $l \geq 2$.

It is worth noting that higher order electric modes and magnetic modes are not contemplated by the electrostatic resonance theory [14] but they have a magneto-quasistatic origin [26]. This difference corresponds to another classification of the modes, different form the aforementioned electric/magnetic or TM/TE. This is the classification of the modes according to their quasistatic bahaviour introduced in section 1.1, the fundamental electric modes are plasmonic modes, while the high order electric modes and the magnetic modes are photonic modes. This subdivision can also be understood by looking at figure 1.6, where we plot the spatial profile of some modes. We see that the fundamental electric (TM with $l = 1$) have the typical dipole, quadrupole, octupole caracter, with their wells and sources. While the higher order electric type (TM with $l > 1$) and the magnetic type (TE) show a completely different vortex profiles.

Let us consider an external excitation $\mathbf{E}_i$, assumed to be solenoidal and solution of the Maxwell's equations in vacuum. Thus, it can be represented within the spherical region Ω in terms of the eigenmodes $\mathbf{C}^{(\alpha)}_{pmnl}(\mathbf{r})$ and $\mathbf{C}^{(\beta)}_{pmnl}(\mathbf{r})$:

$$\mathbf{E}_i(\mathbf{r}) = \sum_{pmnl} \left(A_{pmnl}\mathbf{C}^{(\alpha)}_{pmnl}(\mathbf{r}) + B_{pmnl}\mathbf{C}^{(\beta)}_{pmnl}(\mathbf{r}) \right) \qquad \forall \mathbf{r} \in \Omega, f \quad (1.53)$$

where $\sum_{pmnl} = \sum_{p\in\{e,o\}} \sum_{n=1}^{\infty} \sum_{m=0}^{n} \sum_{l=1}^{\infty}$, and

$$A_{pmnl} = \frac{\langle \mathbf{C}^{(\alpha)_*}_{pmnl}, \mathbf{E}_i \rangle_\Omega}{\langle \mathbf{C}^{(\alpha)_*}_{pmnl}, \mathbf{C}^{(\alpha)}_{pmnl} \rangle_\Omega}, \qquad B_{pmnl} = \frac{\langle \mathbf{C}^{(\beta)_*}_{pmnl}, \mathbf{E}_i \rangle_\Omega}{\langle \mathbf{C}^{(\beta)_*}_{pmnl}, \mathbf{C}^{(\beta)}_{pmnl} \rangle_\Omega}, \qquad (1.54)$$

Therefore, it is straightforward to obtain the scattered field inside the sphere by using (1.13):

$$\mathbf{E}^+_S(\mathbf{r}) = (\varepsilon_r - 1) \sum_{pmnl} \left(\frac{A_{pmnl}}{\alpha_{nl} - \varepsilon_r} \mathbf{C}^{(\alpha)}_{pmnl}(\mathbf{r}) + \frac{B_{pmnl}}{\beta_{nl} - \varepsilon_r} \mathbf{C}^{(\beta)}_{pmnl}(\mathbf{r}) \right). \qquad (1.55)$$

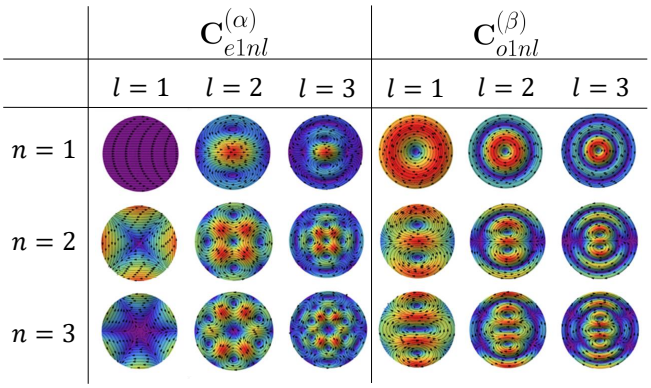

Figure 1.6: Projections of the material independent modes of an isolated sphere over a section of the sphere.

1.3 Resonances in a homogeneous sphere

From the expansion (1.55) it is possible to deduce the general properties of the scattering resonances of a sphere. For passive materials ($\mathrm{Im}\{\varepsilon_r\} \geq 0$), the quantities $|\alpha_{nl} - \varepsilon_r|$ and $|\beta_{nl} - \varepsilon_r|$ do not vanish as ω varies for a given R, because $\mathrm{Im}\{\alpha_{nl}\} < 0$ and $\mathrm{Im}\{\beta_{nl}\} < 0$. Nevertheless, the mode amplitudes $A_{pmnl}/(\alpha_{nl} - \varepsilon_r)$ and $B_{pmnl}/(\beta_{nl} - \varepsilon_r)$ reach their maximum when, for a given R and $\varepsilon_r\,(x)$, the residua $r^{(\alpha)}_{nl}$ and $r^{(\beta)}_{nl}$ are minimum as x varies, namely:

$$\begin{aligned} r^{(\alpha)}_{nl} &= |\varepsilon_r\,(x) - \alpha_{nl}\,(x)| = \underset{x}{\text{Minimum}}, \\ r^{(\beta)}_{nl} &= |\varepsilon_r\,(x) - \beta_{nl}\,(x)| = \underset{x}{\text{Minimum}}, \end{aligned} \tag{1.56}$$

respectively. These are the conditions that maximize the contribution of the modes $\mathbf{C}^{(\alpha)}_{pmnl}$ and $\mathbf{C}^{(\beta)}_{pmnl}$ as x varies, and define the resonance frequencies of the modes, i.e. $\omega = c/R\,x$, and do not depend on the excitation. In other words, eq. (1.55) exemplifies that, for a fixed frequency, when the scatterer's material closely approaches an eigenvalue, the corresponding mode undergoes a boost, namely a *resonance* in a *material picture*. This picture is dual with respect to the *frequency picture*, where the material is instead fixed and the frequency plays the role of the spectral parameter. The material picture is par-

ticularly relevant in light of the latest advances in the design/fabrication techniques of metamaterials, which are enabling the effective value of material's permittivity and permeability to be engineered with increasing precision.

We denote the specific values of x that minimize the residua introduced in (1.56) as $x_{nl}^{(\alpha)}$ and $x_{nl}^{(\beta)}$, the corresponding values of the poles as $\hat{\alpha}_{nl}$ and $\hat{\beta}_{nl}$, and the minimum residua as $\hat{r}_{nl}^{(\alpha)}$ and $\hat{r}_{nl}^{(\beta)}$. The width of a mode is related to the minimum value of the residuum. Specifically, a larger residuum is associated to a *wider* resonance. Thus, according to the needs, we can fix a given threshold ρ a priori and say *narrow* a mode verifying $\hat{r}_{nl} < \rho$, and *broad* otherwise.

We recall that both α_{nl} and β_{nl} are independent of the sphere's permittivity, but they only depend on the size parameter x. Therefore, they can be exhaustively described by the loci they span in the complex plane as a function of x. The resulting diagrams are *universal*, because they apply to any homogeneous sphere, and represent an invaluable tool to investigate the resonances of the nanoparticles.

The real part of α_{nl} and β_{nl} can be either positive or negative. If negative, the condition (1.56) can be satisfied by metals in the visible spectral range ($\mathrm{Re}\{\varepsilon_r\} < 0$), causing a *plasmon resonances*. If positive, the condition (1.56) is verified by dielectrics ($\mathrm{Re}\{\varepsilon_r\} \geq 0$), causing a *photonic resonances*.

In figure 1.7 (a), we plot the locus spanned by the eigenvalue α_{11}, which is associated with the fundamental electric dipole $\mathbf{C}_{pm11}^{(\alpha)}$ shown in figure 1.6. For $x \ll 1$, α_{11} approaches the value -2, in agreement with the Fröhlich condition [29]. This is consistent with equation (1.14) that shows that $\mathrm{Re}\{\gamma_n\} < 0$ in the quasi-electrostatic limit where $\boldsymbol{\nabla} \times \mathbf{C}_n \approx \mathbf{0}$. Therefore, for finite values of x, the condition (1.56) applied to the fundamental dipole represents the natural extension of the Fröhlich condition to the full-retarded case. By increasing x, both the real and the imaginary part of α_{11} move toward more negative values. The decrease of the real part implies, for low losses Drude metals, a red shift of the corresponding resonant frequency [30]. When $x \approx 0.72$, the quantity $\mathrm{Re}\{\alpha_{11}\}$ reaches a minimum and then starts increasing. For larger x, α_{11} lies in fourth quadrant of the complex plane. Then, $\mathrm{Re}\{\alpha_{11}\}$ increases until $x \approx 2$ where it reaches the maximum value of 0.48, and eventually α_{11} asymptotically approaches the origin of the complex plane.

The loci spanned the α_{1l} with $l = 2, 3, 4, 5$, shown in figure 1.7 (b), manifest a very different nature. In fact, α_{1l} always lies in the fourth quadrant of the complex plane irrespectively of the mode order $l \geq 2$. Moreover, for $x \to 0$, the real part of α_{1l} increases, while $\mathrm{Im}\{\alpha_{1l}\}$ approaches zero. This

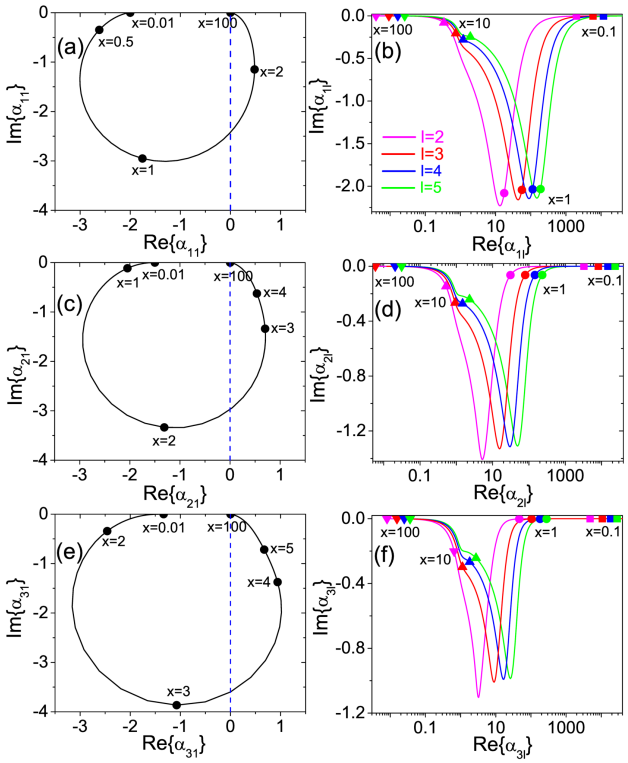

Figure 1.7: Universal loci spanned in the complex plane by the eigenvalues α_{nl} of the electric type eigenmodes of a dielectric sphere by varying its size parameter $x \in [0.01, 100]$. We show the eigenvalues of the fundamental (a) and higher order dipole modes (b), fundamental (c) and higher order (d) quadrupole modes, fundamental (e) and higher order (f) octupole modes. The panels (a,c,e) are in linear scale. The panels (b,d,f) are in semilog scale. (Adapted from [9]. Copyright (2016) by the American Physical Society.)

fact means that, in order these modes to be excited in the quasistatic limit, we need high index dielectrics. By increasing x, Re $\{\alpha_{1l}\}$ moves toward smaller values, while the imaginary part decreases and reaches a minimum. Eventually, α_{1l} approaches the origin of the complex plane for very high values of x.

In figures 1.7 (c) and (e), we plot the loci spanned by α_{21} and α_{31} of the fundamental ($l = 1$) electric quadrupole and octupole eigenmodes. In this case, for $x \to 0$, the eigenvalues α_{21} and α_{31} approach respectively the

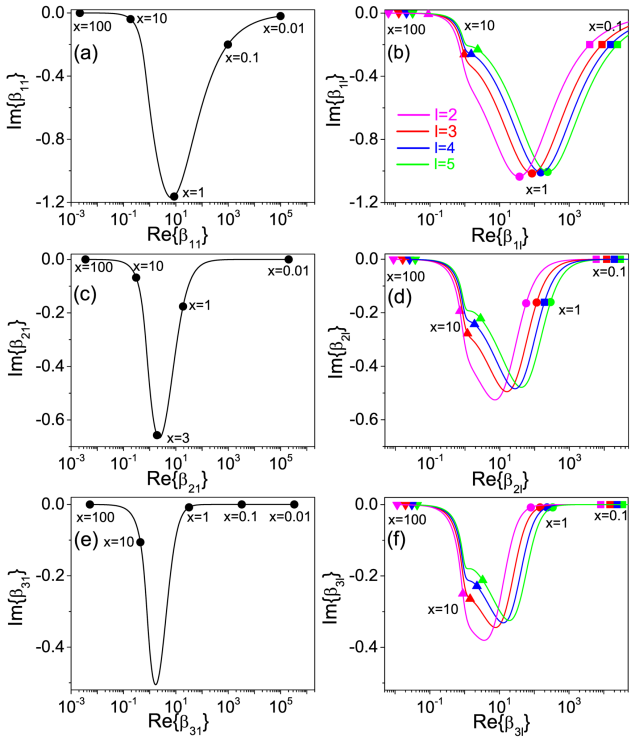

Figure 1.8: Universal loci spanned in the complex plane by the eigenvalues β_{nl} of the magnetic-type eigenmodes of a dielectric sphere by varying its size parameter $x \in [0.01, 100]$. We show the eigenvalues of the fundamental (a) and higher order (b) dipole modes, fundamental (c) and higher order (d) quadrupole modes, fundamental (e) and higher order (f) octupole modes. The panels (a,c,e) are in linear scale. The panels (b,d,f) are in semilog scale. (Adapted from [9]. Copyright (2016) by the American Physical Society.)

values -1.5 and -1.33, which agree with the electro-quasistatic approximation [13,14]. In figures 1.7 (d) and (f), we show the loci of higher order electric quadrupole and octupole modes, which display a behavior similar to higher order electric dipole modes.

Let us now consider the eigenvalues β_{nl} of the magnetic type eigenmodes. The eigenvalues of both the fundamental magnetic eigenmodes, i.e. β_{n1} shown in figure 1.8 (a,c,e) for $n = 1, 2, 3$, and higher order magnetic eigenmodes, i.e. β_{nl} shown in figure 1.8 (b,d,f) for $l = 2, 3, 4, 5$, exhibit the same behavior of the eigenvalue of higher order electric modes. We see that they share the same behaviour of the higher order electric modes.

In conclusion, the loci spanned by the eigenvalues associated with the fundamental electric dipole $\mathbf{C}^{(\alpha)}_{pm11}$, quadrupole $\mathbf{C}^{(\alpha)}_{pm21}$, and octupole $\mathbf{C}^{(\alpha)}_{pm31}$ are confined in a limited region of the complex plane, because $-3 \leq \mathrm{Re}\{\alpha_{11}\} \leq 0.48$, $-2.94 \leq \mathrm{Re}\{\alpha_{21}\} \leq 0.71$, and $-3.1578 \leq \mathrm{Re}\{\alpha_{31}\} \leq 1.0176$, respectively. Therefore, according to the definition given before, these modes are *broad* for spheres with moderately positive permittivity, e.g. Si ($\varepsilon_r \approx 16$). Instead, they may be *narrow* for metal spheres in the visible spectral range, whose permittivity belongs to the second quadrant of the complex plane. These are the *plasmonic* modes. On the contrary, the loci spanned by higher order electric modes and by all the magnetic modes always belong to the fourth quadrant of the complex plane, for any value of x. Thus, they are *broad* in metal sphere and may be *narrow* in particles with moderately positive permittivity. These are the *photonic* modes.

1.4 Analysis and synthesis using material independent modes

Here we want to show how to use the above framework in the analysis of the scattering by nanoparticles and in the material synthesis of them. We will use the simple case of the scattering by an isolated sphere, but it has already been shown how everything can be applied to quasi-1D resonators [20], surfaces [22], coated-sphere [18, 31], dimers [32] and arbitrarily shaped nanoparticles [33]. To start, let us observe that, due to the bi-orthogonality property of Eq. (1.12), we have

$$\langle \mathbf{C}^{(\delta)_*}_{pmnl},\ \mathbf{C}^{(\delta')}_{p'm'n'l'} \rangle_\Omega = 0 \qquad \forall \left(\delta, p, m, n, l\right) \neq \left(\delta', p', m', n', l'\right), \quad (1.57)$$

where $\delta, \delta' \in \{\alpha, \beta\}$. Moreover, due to the spherical symmetry, we also have that a subset of the modes is orthogonal on every spherical surface:

$$\int_0^{2\pi}\int_0^{\pi}\left(\mathbf{C}^{(\delta)}_{pmnl}\right)^* \cdot \mathbf{C}^{(\delta')}_{p'm'n'l'}\sin(\theta)\,d\theta d\phi = 0 \qquad \forall\,(\delta,p,m,n) \neq \left(\delta',p',m',n'\right). \tag{1.58}$$

In particular, the plasmonic modes are orthogonal in power, and thus they cannot interfere in the total scattered power. While, in general, since the material independent modes only verify the (1.12), they do interfere.

Coupling with a plane wave

Let us assume that the incident field is a x-polarized plane wave propagating along the z-axis:

$$\mathbf{E}_i(\mathbf{r}) = \mathbf{E}_0 e^{ikz}\,\hat{\mathbf{e}}_x. \tag{1.59}$$

It can be shown that the scattered field takes the form [9]:

$$\begin{aligned}
\mathbf{E}_S^+(\mathbf{r}) &= (\varepsilon_r - 1)\sum_{n=1}^{\infty} E_n \sum_{l=1}^{\infty}\left[\frac{B_{nl}}{\beta_{nl}-\varepsilon_r}\mathbf{M}^{(1)}_{o1n}\left(\sqrt{\beta_{nl}}\,k_0\mathbf{r}\right)\right.\\
&\quad\left. -i\frac{A_{nl}}{\alpha_{nl}-\varepsilon_r}\mathbf{N}^{(1)}_{e1n}\left(\sqrt{\alpha_{nl}}\,k_0\mathbf{r}\right)\right]\\
\mathbf{E}_S^-(\mathbf{r}) &= (\varepsilon_r - 1)\sum_{n=1}^{\infty} \frac{E_n}{h_n^{(1)}(x)} \sum_{l=1}^{\infty}\left[\frac{B_{nl} j_n\left(\sqrt{\beta_{nl}}\,x\right)}{\beta_{nl}-\varepsilon_r}\mathbf{M}^{(3)}_{o1n}\left(k_0\mathbf{r}\right)\right.\\
&\quad\left. -i\frac{A_{nl}\sqrt{\alpha_{nl}}\,j_n\left(\sqrt{\alpha_{nl}}\,x\right)}{\alpha_{nl}-\varepsilon_r}\mathbf{N}^{(3)}_{e1n}\left(k_0\mathbf{r}\right)\right],
\end{aligned} \tag{1.60}$$

where: :

$$A_{nl} = \frac{\langle \mathbf{N}^{(1)*}_{e1n}\left(\sqrt{\alpha_{nl}}k_0\mathbf{r}\right), \mathbf{N}^{(1)}_{e1n}\left(k_0\mathbf{r}\right)\rangle_\Omega}{\langle \mathbf{N}^{(1)*}_{e1n}\left(\sqrt{\alpha_{nl}}k_0\mathbf{r}\right), \mathbf{N}^{(1)}_{e1n}\left(\sqrt{\alpha_{nl}}k_0\mathbf{r}\right)\rangle_\Omega}, \tag{1.61}$$

$$B_{nl} = \frac{\langle \mathbf{M}^{(1)*}_{o1n}\left(\sqrt{\beta_{nl}}k_0\mathbf{r}\right), \mathbf{M}^{(1)}_{o1n}\left(k_0\mathbf{r}\right)\rangle_\Omega}{\langle \mathbf{M}^{(1)*}_{o1n}\left(\sqrt{\beta_{nl}}k_0\mathbf{r}\right), \mathbf{M}^{(1)}_{o1n}\left(\sqrt{\beta_{nl}}k_0\mathbf{r}\right)\rangle_\Omega}. \tag{1.62}$$

As reference result, we consider the solution of the problem using the standard Mie theory [28]. The scattered field has the following expansion in terms

of VSWFs:

$$\mathbf{E}_S^- = \sum_{n=1}^{n_{max}} E_n \left(i a_n \mathbf{N}_{e1n}^{(3)}(k_0\mathbf{r}) - b_n \mathbf{M}_{o1n}^{(3)}(k_0\mathbf{r}) \right), \tag{1.63}$$

where a_n and b_n are the Mie scattering coefficients, which can be found in [28], and $E_n = i^n(2n+1)/\left[n(n+1)\right]$. It is worth noting that the Mie coefficients a_n and b_n are complicated functions of ε_r. It makes the material design through Mie theory much more complex than the one using the material independent modes, which we will be shown in section 1.4.2.

According to the definition of the scattering cross-section σ_{sca} given in [28], the following expressions for σ_{sca} holds:

$$\sigma_{sca} = \frac{1}{x^2} \sum_{n=1}^{n_{max}} \left(\Big| \sum_{l=1}^{l_{max}} u_{nl} \Big|^2 + \Big| \sum_{l=1}^{l_{max}} v_{nl} \Big|^2 \right), \tag{1.64}$$

$$\sigma_{sca} = \frac{2}{x^2} \sum_{n=1}^{n_{max}} (2n+1) \left(|a_n|^2 + |b_n|^2 \right), \tag{1.65}$$

where the coefficients u_{nl} and v_{nl} can be found in [19]. In figure 1.9 we validate the expansion (1.60) by comparing these two scattering cross-sections. All the details can be found in [19]. We plot σ_{sca} for $x = \pi$ (a) and $x = 2\pi$ (b) as a function of ε_r. In figure 1.9 (a) we plot the scattering efficiency of the sphere with $x = \pi$, truncating the inner sum of (1.64) to $l_{max} = 1$ (blue line) and to $l_{max} = 3$ (red line). When only the fundamental modes ($l_{max} = 1$) are considered, we have agreement with the standard Mie theory only for small values of ε_r, while increasing l_{max} to 3 the results of the two approaches closely agree. The scattering efficiency of the sphere with size parameter $x = 2\pi$ is shown in figure 1.9 (b). Here, we truncated the inner sum to $l_{max} = 3$ (blue line) and to $l_{max} = 6$ (red line). Although for $l_{max} = 3$ it is apparent a moderate disagreement with the Mie theory, for $l_{max} = 6$ the outcomes of the two approaches become almost indistinguishable.

1.4.1 Resonances and interferences in the scattering by Si and Ag spheres

As an example of the efficiency of the MIM method in the analysis of nanostructures, we compare the spectrum of the scattered patterns by a sphere of silicon (Si) of $R = 100$ nm and by a sphere of silver (Ag) of $R = 60$ nm. We describe the Ag permittivity $\varepsilon_{r,Ag}$ by using experimental data [34], while for

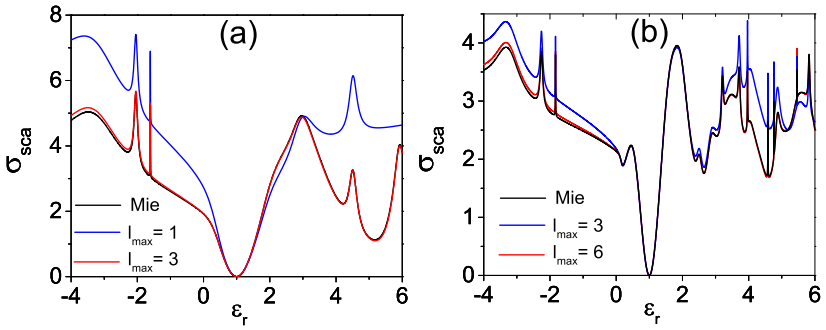

Figure 1.9: Scattering efficiency σ_{sca} of a dielectric sphere with size parameter $x = \pi$ (a) and $x = 2\pi$ (b) excited by a linearly polarized plane wave, as a function of $\varepsilon_r \in [-4, 6]$ calculated using equation (1.64) and with the standard Mie theory, equation (1.65). In all the calculations we have assumed $n_{max} = 10$. (Panel (b) was adapted from [9]. Copyright (2016) by the American Physical Society.)

Si we employ a constant permittivity, i.e. $\varepsilon_{r,Si} = 16$. First of all, in tables 1.1 and 1.2 we list, for some representative modes of the investigated spheres, the quantities $x_{nl}^{(\alpha)}$ and $x_{nl}^{(\beta)}$, which are the values of x minimizing the residua introduced in (1.56). We also show the corresponding values of the poles $\hat{\alpha}_{nl}$ and $\hat{\beta}_{nl}$, and the minimum residua $\hat{r}_{nl}^{(\alpha)}$ and $\hat{r}_{nl}^{(\beta)}$. The resonant frequencies can be immediately obtained from $x_{nl}^{(\alpha)}$ and $x_{nl}^{(\beta)}$ by using the relation $\omega = c/R\, x$. We highlight in bold the narrow modes, fixing a threshold of $\rho = 5$. We searched for the minima in the range $x \in [0.01, 100]$ and $x \in [0.19, 1.08]$ for Si and Ag, respectively.

For the Si sphere, table 1.1 shows that the minimum residua associated with the plasmon modes (fundamental electric modes) are roughly one order of magnitude larger than the ones associated to the photonic modes (higher order electric modes and to the magnetic modes). For this reason, the fundamental electric modes are *broad*, while the higher order electric modes and the magnetic modes are *narrow*. Furthermore, table 1.1 shows that the real parts of the poles associated to the higher order electric modes and to the magnetic modes all approach the value of $\varepsilon_{r,Si} = 16$.

For Ag particles exactly the opposite happens. Table 1.2 shows that the residua exhibited by the photonic modes are much larger than the ones of the

Table 1.1: Values of x minimizing the residua, corresponding poles and residua for a 100 nm Si sphere. (Adapted from [24]. Copyright (2017) by IOP Publishing.)

n	l	$x_{nl}^{(\alpha)}$	$\hat{\alpha}_{nl}$	$\hat{r}_{nl}^{(\alpha)}$	$x_{nl}^{(\beta)}$	$\hat{\beta}_{nl}$	$\hat{r}_{nl}^{(\beta)}$
1	1	2.20	0.48 - 0.96 i	15.6	**0.75**	**16.2 - 1.07 i**	**1.08**
1	2	**1.06**	**16.3 - 2.15 i**	**2.17**	**1.55**	**15.9 - 0.96 i**	**0.97**
2	1	2.99	0.70 - 1.33 i	15.3	**1.09**	**16.2 - 0.21 i**	**0.27**
2	2	**1.38**	**16.0 - 0.31 i**	**0.31**	**1.89**	**16.0 - 0.45 i**	**0.45**
3	1	3.86	1.00 - 1.67 i	15.1	**1.42**	**15.9 - 0.04 i**	**0.07**

Table 1.2: Values of x minimizing the residua, corresponding poles and residua for a 60 nm Ag sphere. (Adapted from [24]. Copyright (2017) by IOP Publishing.)

n	l	$x_{nl}^{(\alpha)}$	$\hat{\alpha}_{nl}$	$\hat{r}_{nl}^{(\alpha)}$	$x_{nl}^{(\beta)}$	$\hat{\beta}_{nl}$	$\hat{r}_{nl}^{(\beta)}$
1	1	**0.92**	**-2.42 - 2.61 i**	**3.0**	1.08	7.6 - 1.17 i	8.55
1	2	1.25	11.8 - 2.2 i	10.3	1.08	33.0 - 1.04 i	33.9
2	1	**1.0**	**-2.03 - 0.11 i**	**0.35**	1.08	16.5 - 0.20 i	17.4
2	2	1.25	19.8 - 0.19 i	17.6	1.08	50.5 - 0.19 i	51.3

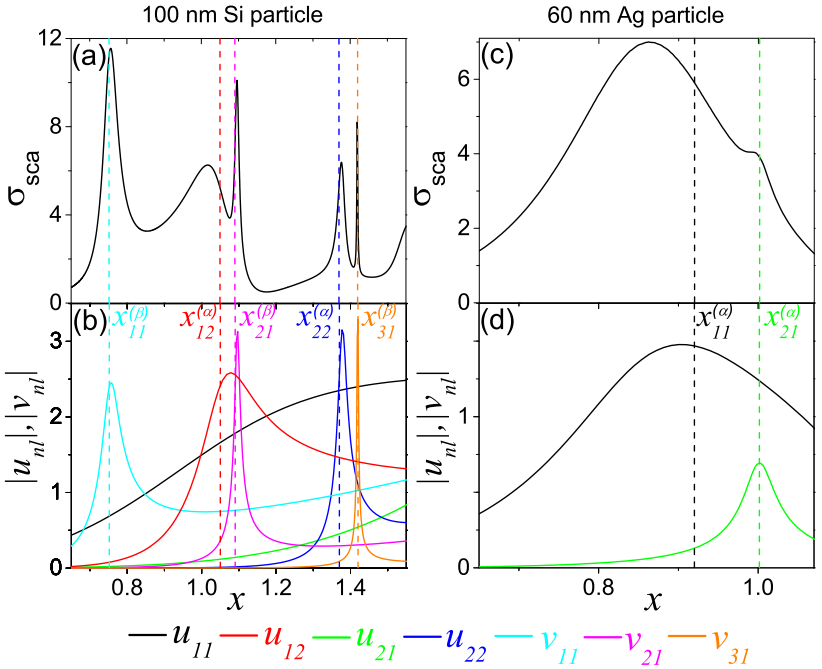

Figure 1.10: Scattering efficiency σ_{sca} of the investigated Si (a) and Ag (c) spheres as function of x. Absolute value of the coefficients u_{nl} and v_{nl} as a function of x for Si (b) and Ag (d) spheres. The vertical dashed lines represent the resonance positions $x_{nl}^{(\alpha)}$ and $x_{nl}^{(\beta)}$, as listed in the third and sixth columns of tables 1.1, 1.2. (Adapted from [24]. Copyright (2017) by IOP Publishing.)

plasmonic modes. In particular, the former modes are *broad*, while the latter are *narrow*.

In conclusion, the narrow modes in metal and silicon spheres constitute two disjoint sets. This fact explains why silicon and metal nano-sphere of comparable size exhibit remarkably different resonant behaviours. In particular, magnetic type modes are always broad in metal spheres, regardless of x.

We now investigate the scattering efficiency σ_{sca} of Si and Ag spheres as a function of the size parameter x, when they are excited by a linearly polarized plane wave. Due to the symmetry of $\mathbf{E}_i$, only even electric modes and odd magnetic modes with $m = 1$ are excited (the ones that we have shown in figure 1.6). In figure 1.10 we plot σ_{sca} of the 100 nm Si (a) sphere and of the

60 nm Ag (c) sphere as a function of x. In figure 1.10 (b) and (d) we show the absolute value of the coefficients u_{nl} and v_{nl} for the Si and Ag spheres, respectively, as a function of the electric size x. We also show with vertical dashed lines the resonant values of x, namely $x_{nl}^{(\alpha)}$ and $x_{nl}^{(\beta)}$, as listed in the third and sixth columns of tables 1.1 and 1.2. We recall that $x_{nl}^{(\alpha)}$ and $x_{nl}^{(\beta)}$ are the values of x in correspondence of which the amplitudes of $\mathbf{C}_{e1nl}^{(\alpha)}$ and $\mathbf{C}_{o1nl}^{(\beta)}$, respectively, are maximized.

Now, we describe σ_{sca} of the Si nanosphere, shown in figure 1.10 (a). All σ_{sca} peaks but one can be attributed to the dominant contribution of a single resonant mode. In particular, the first peak from left occurs exactly at $x_{11}^{(\beta)}$, where the contribution of the fundamental magnetic dipole $\mathbf{C}_{o111}^{(\beta)}$ is maximum. This fact is also demonstrated by figure 1.10 (b), where v_{11} is also peaked in correspondence of $x_{11}^{(\beta)}$ and it is dominant compared to the remaining coefficients.

Instead, no mode resonates in correspondence of the second peak. This peak is localized at $x = 1.02$ and originates from the positive interplay between two off-resonance modes, namely the fundamental electric dipole $\mathbf{C}_{e111}^{(\alpha)}$ and the second order electric dipole $\mathbf{C}_{e112}^{(\alpha)}$, as demonstrated by figure 1.10 (b), where u_{11} and u_{12} have comparable magnitude. The third σ_{sca} peak is caused by the fundamental magnetic quadrupole $\mathbf{C}_{o121}^{(\beta)}$. The fourth peak is due to second order electric dipole $\mathbf{C}_{e122}^{(\alpha)}$, and the fifth one to the fundamental magnetic octupole $\mathbf{C}_{o131}^{(\beta)}$.

The scattering dip enclosed by peaks 2 and 3 at $x = 1.076$, and the corresponding Fano lineshape of σ_{sca} originates from the destructive interference between the *broad* fundamental electric dipole $\mathbf{C}_{e111}^{(\alpha)}$ and the *narrow* second order electric dipole $\mathbf{C}_{e112}^{(\alpha)}$, which are not orthogonal. In correspondence of this dip, the values of the coefficients are $u_{11} = 0.78 - 0.95i$ and $u_{12} = 0.063 + 1.83i$. We point out that, although the scattering dip is in the close proximity of the third peak, the magnetic quadrupole $\mathbf{C}_{o121}^{(\beta)}$ isn't responsible for it, because it is orthogonal to both $\mathbf{C}_{e111}^{(\alpha)}$ and $\mathbf{C}_{e112}^{(\alpha)}$ due to equation (1.58), and interference cannot take place. In conclusion, the scattering efficiency of a Si sphere features a Fano lineshape, where the dip is due to the interference between the fundamental and the first order electric dipoles, while the peak is due to the fundamental magnetic quadrupole mode.

We now investigate the role played by the fundamental electric dipole $\mathbf{C}_{e111}^{(\alpha)}$ in the scattering from a Si sphere. This mode is broad. Neverthe-

less, this mode significantly contributes to the scattering efficiency, because the coefficient A_{11} of expansion (1.60) is very large compared to A_{nl} and B_{nl} of the remaining modes. This is due to the fact that the fundamental dipole $\mathbf{C}_{e111}^{(\alpha)}$ more easily couples with the exciting plane wave and more strongly radiates into the far field. It is possible to qualitatively compare the σ_{sca} spectrum shown in figure 1.10 (a) for a $R = 100\ nm$ Si sphere with the dark-field scattering spectrum measured by Kuznetsov et al. [35] for a $R = 91\ nm$ Si sphere laying on a Si substrate. The experimental and theoretical peaks are found into one to one correspondence. Next, we investigate the σ_{sca} spectrum of the Ag nanosphere. It can be completely described by considering only the fundamental electric dipole and electric quadrupole, namely $\mathbf{C}_{e111}^{(\alpha)}$ and $\mathbf{C}_{e121}^{(\alpha)}$. These modes are narrow and the peak associated with the mode $\mathbf{C}_{e111}^{(\alpha)}$ is *wider* compared to $\mathbf{C}_{e121}^{(\alpha)}$, due to large imaginary part of the pole $\hat{\alpha}_{nl}$, as shown in table 1.2. Moreover, we found no Fano lineshapes in the spectrum, due to the orthogonality of the fundamental electric modes according to equation 1.58.

An analysis in terms of near field electric and magnetic patterns can be found in [19].

1.4.2 Back-scattering cancellation

As an example of how to use the MIM method to design a proper material to achieve a desired scattering feature, we show the cancellation of the back-scattering. This is an interesting problem that roots in the first work of Kerker et al. [36], where they first demonstrated the suppression of the back-scattering in magneto-dielectric spheres of arbitrary size with $\varepsilon = \mu$. In that case, cancellation of the backward scattering results from the destructive interference between magnetic and electric multipoles of corresponding order. More recently, Nieto et al. [37] predicted that, when the scattering response of a *small* non-magnetic sphere is dominated by the multipolar orders associated with magnetic and electric dipoles, vanishing backscattering can result from their destructive interference. This scenario, that generalizes the Kerker's condition, has been experimentally observed both in the microwaves [38] and in the visible spectral range [39, 40]. An additional extension of the Kerker's conditions, that describes the suppression of the backscattering from a sphere when excited by a local dipole source, has also been introduced in Ref. [41]. Furthermore, the generalized Kerker conditions have been also verified in subwavelength metal-dielectric core-shell particles [42], core shell nanowires [43], silicon nanodisks [44], and to particles with cylindrical symmetry [45]. The cancel-

lation of the backscattering have been also achieved in a nanoring antenna by balancing the electric dipole and quadrupole [46], and in a core-shell particle by balancing multipoles of different orders [47].

The cancellation of the backscattering is often associated with an enhanced directionality of the scattering, which may have a great impact in optical wireless nano-antenna links. Here we want to show the backscattering cancellation from a dielectric sphere is also possible even when the size of the particle is comparable with the incident wavelength and many scattering orders are involved. Moreover, recently we have proven that it is also possible to cancel the back-scattering of a dielectric sphere 10 times bigger that the incident wavelength, by designing a proper surface coating of finite conductivity [31].

Here, we solve the exercise for a single dielectric spere illuminated by a x-polarized plane wave of unit intensity, propagating along the z-axis. The radiation pattern is defined by [48]:

$$\mathbf{E}_S^{\infty}(\theta,\phi) = \lim_{r\to\infty}\left[re^{-ik_0 r}\mathbf{E}_S^{-}(r,\theta,\phi)\right]. \tag{1.66}$$

Due to symmetry consideration, the only non-vanishing component of the radiation pattern in the backscattering direction ($\theta=\pi$) is $\mathbf{E}_S^{\infty}\cdot\mathbf{i}_\theta$. Our task is to find the zeros of $\mathbf{E}_S^{\infty}\cdot\mathbf{i}_\theta$ as a function of ε_r. It results [19]:

$$\mathbf{E}_S^{\infty}\cdot\mathbf{i}_\theta(\varepsilon_r) = \frac{\varepsilon_r-1}{k_0}\sum_{n=1}^{\infty}\sum_{l=1}^{\infty}\left\{\frac{\delta_{nl}(x,\theta,\phi)}{\beta_{nl}(x)-\varepsilon_r}+\frac{\gamma_{nl}(x,\theta,\phi)}{\alpha_{nl}(x)-\varepsilon_r}\right\} \quad , \tag{1.67}$$

where:

$$\begin{aligned}
\gamma_{nl}(x,\theta,\phi) &= -iE_n\frac{\sqrt{\alpha_{nl}}\,j_n\left(\sqrt{\alpha_{nl}}x\right)}{h_n^{(1)}(x)}A_{nl}\mathbf{N}_{e1n}^{(\infty)}(\theta,\phi)\cdot\mathbf{i}_\theta,\\
\delta_{nl}(x,\theta,\phi) &= E_n\frac{j_n\left(\sqrt{\beta_{nl}}x\right)}{h_n^{(1)}(x)}B_{nl}\mathbf{M}_{o1n}^{(\infty)}(\theta,\phi)\cdot\mathbf{i}_\theta,
\end{aligned} \tag{1.68}$$

$E_n = i^n(2n+1)/[n(n+1)]$, A_{nl} and B_{nl} are given by (1.61)-(1.62) and (see Appendix A):

$$\begin{aligned}
\mathbf{M}_{o1n}^{(\infty)} &= \lim_{r\to\infty}\left[k_0re^{-ik_0r}\mathbf{M}_{o1n}^{(3)}\right]\\
\mathbf{N}_{e1n}^{(\infty)} &= \lim_{r\to\infty}\left[k_0re^{-ik_0r}\mathbf{N}_{e1n}^{(3)}\right].
\end{aligned} \tag{1.69}$$

Therefore, we put all the terms in the sum of equation 1.67 over a common denominator, obtaining a rational function of ε_r and we zero the resulting numerator, which is a polynomial in ε_r. This is a general property of the MIM

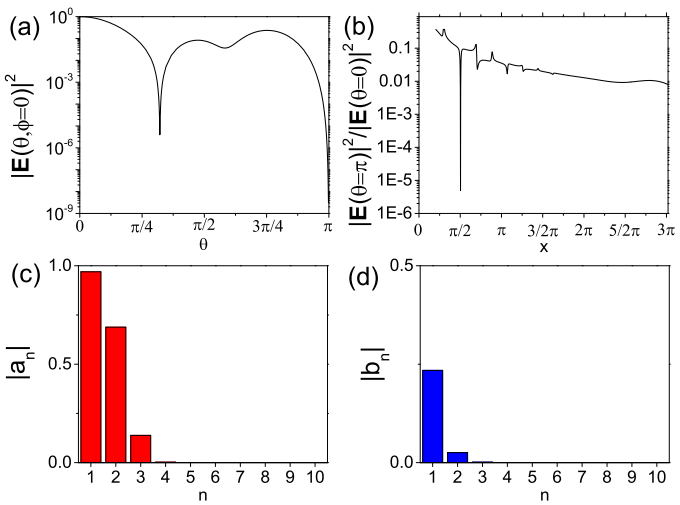

Figure 1.11: (a) Squared magnitude of the radiation pattern for $\phi = 0$ as a function of the angle θ for the sphere of size parameter $x = \pi/2$. (b) Ratio between the squared magnitudes of the electric field in the back- and forward-scattering direction as a function of the size parameter x. (c)-(d) Magnitude of Mie coefficients (which appears in equation (1.63)) for the sphere of size parameter $x = \pi/2$. All the calculations have been performed with the standard Mie theory assuming $n_{max} = 10$. The permittivity of the sphere is the designed value $\varepsilon_r = -1.475 + 5.937 \cdot 10^{-3} i$.

approaches. Indeed, as a direct consequence of the structure of the auxiliary eigenvalue problem, a general task always reduces to the problem of *finding the roots of a polynomial*.

We apply this procedure to find the permittivity of a homogeneous sphere of radius $R = \lambda/4$ that cancels the backscattering. We set $x = \pi/2$, $\theta = \pi$ and $\phi = 0$ in the expression (1.67) truncated with $n_{max} = 10$ and $l_{max} = 8$. Among the different solutions, we choose $\varepsilon_r = -1.475 + 5.937 \cdot 10^{-3} i$. To validate this result, we plot in figure 1.11 (a) the squared magnitude of the radiation pattern of the sphere with the designed permittivity as a function of the angle θ for $\phi = 0$, computed by using the standard Mie theory with $n_{max} = 10$. We achieved a ratio between the back- and the forward- scattered power of -53dB. It is worth noting that the achieved backscattering suppression originates from a complex interplay between the electric dipole, electric quadrupole and magnetic dipole multipolar scattering orders. This fact is demonstrated with the help of figures 1.11 (c) and (d) where we show the magnitude of the Mie coefficients (which appears in equation (1.63)). In figure 1.11 (b) we show in a semi-logarithmic scale the ratio between the backscattering and the forward scattering as a function of the size parameter x for the sphere with the designed value of permittivity. As expected, in correspondence of the $x = \pi/2$ this ratio has a dip.

Now, following the same algorithm, we find the permittivity of a homogeneous sphere of radius $R = \lambda$ that cancels the backscattering. Among the different solutions, we choose the only one that is physically realizable by a passive material, i.e. $\varepsilon_r = -2.2747 + 8.188 \cdot 10^{-2} i$. Then, we plot in figure 1.12 (a) the squared magnitude of the radiation pattern of the sphere with $x = 2\pi$ with the designed permittivity as a function of the angle θ for $\phi = 0$ computed by using the standard Mie theory with $n_{max} = 10$. We achieved a ratio between the back- and the forward- scattered power of -54dB. In this case, since the size of the sphere is equal to the incident wavelength, many electric and magnetic modes take part in the interference. This fact is demonstrated by figure 1.12 (c) and (d) where we show that the magnitude of the Mie coefficients, as defined by equation (1.63), is significant up to the multipoles of order 9. In figure 1.12 (b) we show, in a semi-logarithmic scale, the ratio between the backscattering and the forward scattering as a function of the size parameter x for the sphere of the designed value of permittivity. As expected, we note that in correspondence of the $x = 2\pi$ this curve has a dip.

This method can be also used to design the permittivity of the sphere to pursue many different goals, including zeroing or focusing a given field com-

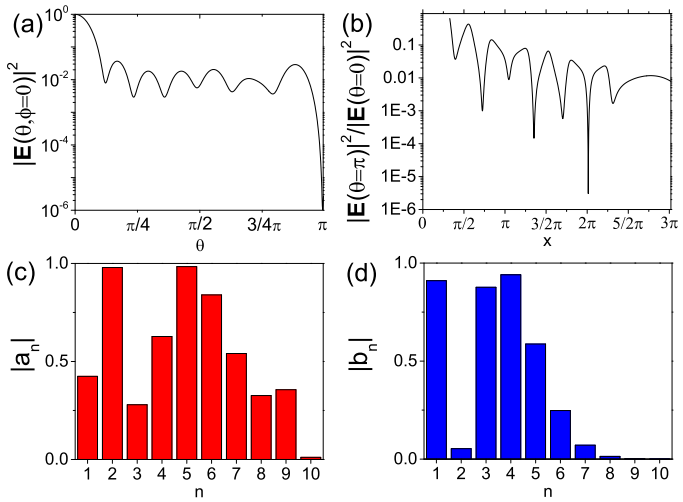

Figure 1.12: (a) Squared magnitude of the radiation pattern for $\phi = 0$ as a function of the angle θ for the sphere of size parameter $x = 2\pi$. (b) Ratio between the squared magnitudes of the electric field in the back- and forward-scattering direction as a function of the size parameter x. (c)-(d) Magnitude of Mie coefficients (as defined by equation (1.63)) for the sphere of size parameter $x = 2\pi$. All the calculations have been performed with the standard Mie theory assuming $n_{max} = 10$. The permittivity of the sphere is the designed value $\varepsilon_r = -2.2747 + 8.188 \cdot 10^{-2} i$.

ponent in an arbitrary point of space, in the near or in the far zone. These objectives can be all easily achieved by zeroing a polynomial. Finally, we note that the proposed method leads to high computational burden when $x \gg 1$ because many modes have to be considered to accurately describe the field.

These are some examples of how the material independent modes can be enlightening in the analysis of the scattering by localized nanoparticles and how it is easy to achieve material design of nanostructures in order to tailor a particular scattering pattern. For simplicity, only the test case of an isolated single sphere has been considered, but it is worth to point out that these procedures are totally general as they have been applied in many different and more complex scenarios, such as the scattering by coated spheres [18,31], arbitrarily shaped nanoparticles [33], surfaces [22], and quasi-1D resonators [20]. Moreover, this formalism has been also recently developed in the case of not connected domain, in the specific case of sphere dimers [32]. In this case, this material picture, in addition to its clarifying power, proved also to be the right scenario to study the hybridization problem in the dimer. Indeed, it provided the first complete hybridization theory of dielectric dimers in the full-wave regime.

1.5 Conclusions

In this thesis chapter, we have introduced a full-retarded modal theory for the scattering by nanostructures, with particular reference to the scattering by homogeneous nanoparticles of permittivity $\varepsilon_r(\omega)$.
By solving a proper auxiliary eigenvalue problem, it was possible to derive a set of material independent modes and of eigenpermittivities to represent the scattered field. We have shown how this material picture is able to separate the roles of the geometry and of the material in the scattering process: the former dictates the available scattering patterns by determining the modes; the latter weights their contribution to the scattered field by fixing the coefficients of the expansion. Since the coefficients resulted to be simple rational functions of the ε_r and of the eigenpermittivities, it was possible to strongly simplify the analysis and the synthesis tasks. As a matter of fact, we have shown how convenient it is to study the universal loci spanned by the eigenpermittivities in the complex plane, by varying the ratio between the incident wavelength and the linear dimension of the nanoparticle. It allowed us to define a material resonance condition for the MIMs, an associate criterion to establish if a mode is broad or narrow, and to classify the modes in plasmonic and photonic, according to

their resonance behaviour.

We have started the discussion by comparing the material independent modes decomposition of the scattered field with the more diffused quasi normal modes decomposition. We have shown that, in the case of homogeneous scatterers, the material picture results more convenient than the frequency one because: (i) the material independent modes are bounded, and so no normalization process is needed; (ii) to have a complete material/frequency understanding of the scattering, the QNM expansion has to be computed for each material in the half-plane of Im $\{\varepsilon_r\} > 0$, while the MIM one for each $\omega > 0$.

Then, we have analyzed in detail the scattering by a single sphere. We have computed the modes and we have used the loci of the eigenpermittivities to provide a rigorous understanding of the interference phenomena (including Fano lineshapes) that may take place when a Si/Ag sphere is illuminated by a linearly polarized plane wave. Moreover, we have shown how to use the MIM expansion to perform material design, i.e. to find the best material to achieve a prescribed scattering feature. In particular we have designed a homogeneous sphere, whose scattering in the froward direction exceeds the back one of more than 50 dB.

Even if we have limited our discussion to the general properties of the theory and to the analysis of two easy examples, this full-retarded material independent concept has proven to be enlightening also for several more complicated scenarios. In particular, it has been applied to coated spheres [18], arbitrary shaped nanoparticles [19], quasi-1D nanoribbons [20], and surfaces [22]. In these other cases, however, it is often more efficient to reformulate the scattering problem in an integral form, and working with eigencurrents and eigenconductivities. Moreover, the MIM expansion appears to be very promising in the study of the scattering by nanoparticle arrays. Indeed, it has been already proven to be the right framework to develop a rigorous hybridization theory in the case of a sphere dimer [32]. Eventually, the MIM theory can also play a key role in the future development of the design technique for high-index dielectric nanostructures [26] and, in general, it is the most natural framework to design metamaterials.

Appendix A: Vector Spherical Wave Functions

The explicit expressions of the vector spherical wave functions (VSWF) are [28]:

$$\begin{aligned}
\mathbf{N}_{\substack{e\\o}mn}(k\,\mathbf{r}) &= n(n+1)\begin{pmatrix}\cos m\phi\\ \sin m\phi\end{pmatrix} P_n^m(\cos\theta)\,\frac{z_n(k\,r)}{k\,r}\hat{\mathbf{e}}_r \\
&+ \begin{pmatrix}\cos m\phi\\ \sin m\phi\end{pmatrix}\frac{dP_n^m(\cos\theta)}{d\theta}\frac{1}{k\,r}\frac{d}{dr}\left[r z_n(k\,r)\right]\hat{\mathbf{e}}_\theta \\
&+ m\begin{pmatrix}-\sin m\phi\\ \cos m\phi\end{pmatrix}\frac{P_n^m(\cos\theta)}{\sin\theta}\frac{1}{k\,r}\frac{d}{dr}\left[r z_n(k\,r)\right]\hat{\mathbf{e}}_\phi, \qquad \text{(A1)}\\
\mathbf{M}_{\substack{e\\o}mn}(k\,\mathbf{r}) &= m\begin{pmatrix}-\sin m\phi\\ \cos m\phi\end{pmatrix}\frac{P_n^m(\cos\theta)}{\sin\theta} z_n(k\,r)\,\hat{\mathbf{e}}_\theta \\
&- \begin{pmatrix}\cos m\phi\\ \sin m\phi\end{pmatrix}\frac{dP_n^m(\cos\theta)}{d\theta} z_n(k\,r)\,\hat{\mathbf{e}}_\phi.
\end{aligned}$$

where the subscripts e and o denote even and odd, and $P_n^m(\cdot)$ are the associated Legendre function of the first kind of degree n and order m. Moreover, the superscripts $^{(1)}$ and $^{(3)}$ are appended to the functions $\mathbf{M}_{\substack{e\\o}mn}$ and $\mathbf{N}_{\substack{e\\o}mn}$ to denote the function z_n, namely Bessel functions of the first kind j_n and Hankel functions of the first kind h_n, respectively.

Starting from eqs. (A1) it is possible to derive the expression of (1.69):

$$\begin{aligned}
\mathbf{N}^{(\infty)}_{\substack{e\\o}mn}(\theta,\phi) &= (-i)^n\begin{pmatrix}\cos m\phi\\ \sin m\phi\end{pmatrix}\frac{dP_n^m(\cos\theta)}{d\theta}\hat{\mathbf{e}}_\theta \\
&+ (-i)^n m\begin{pmatrix}-\sin m\phi\\ \cos m\phi\end{pmatrix}\frac{P_n^m(\cos\theta)}{\sin\theta}\hat{\mathbf{e}}_\phi, \\
\mathbf{M}^{(\infty)}_{\substack{e\\o}mn}(\theta,\phi) &= (-i)^{n+1} m\begin{pmatrix}-\sin m\phi\\ \cos m\phi\end{pmatrix}\frac{P_n^m(\cos\theta)}{\sin\theta}\hat{\mathbf{e}}_\theta \\
&- (-i)^{n+1}\begin{pmatrix}\cos m\phi\\ \sin m\phi\end{pmatrix}\frac{dP_n^m(\cos\theta)}{d\theta}\hat{\mathbf{e}}_\phi.
\end{aligned} \qquad \text{(A2)}$$

Chapter 2

Quantum theory of frequency shift and radiative decay rate in arbitrarily shaped metal nanoparticles and dimers

In this thesis chapter, we discuss the mode quantization of the localized surface plasmons in arbitrarily shaped metal nanoparticles and dimers, in the full-retarded regime. We introduce a rigorous canonical quantization scheme that can be applied to arbitrarily shaped objects beyond the quasistatic regime. In particular, we introduce an approximation of the full plasmon-photon Hamiltonian, which is able to describe the retarded quantum dynamics in all the cases of interest for the applications. Moreover, our derivation provides explicit formulas to compute the radiative decay rate and the frequency shift experienced by the plasmon excitations in the full-retarded regime. These formulas are, to the knowledge of the authors, novel, and appear to be more efficient than the available implicit or perturbative method to compute these quantities.

Quantizing plasmon oscillations

During the last two decades, several research groups have investigated the possibility of exploiting the sub-wavelength confinement of light provided by plasmonic nanostructures to enhance the optical response of quantum emit-

ters [49,50]. This focusing mechanism allows the establishment of strong coupling regimes between quantum sources and light, which represents a promising tool to control light at the quantum level [51–53]. As a matter of fact, a proper electromagnetic design of the environment surrounding the quantum source can deeply modify its dynamics, e.g. changing the lifetime of the excited state through the Purcell effect [6,54,55]. Moreover, the quantum nature of the plasmon excitations has been experimentally proven in its wave-particle duality [56, 57], and in its property to preserve the quantum features of the photons that excite them, such as entanglement [58, 59] and sub-Poissonian statistics [60].

Whether we are interested in the fundamental aspects of quantum plasmonics or in its applications to the quantum technology world, the first key point to address is the formulation of an appropriate quantum mechanical description of the surface plasmons. From the pioneering works of Pines [61] and Hopfield [62] on, several mode quantization schemes have been proposed over time [63–72]. The majority of these works deal with the investigation of nanoparticles of canonical shape, e.g. a metal sphere, within the electroquasistatic regime.

Nonetheless, interesting perspectives can be opened by studying the interactions with more complex electromagnetic surroundings, such as arbitrary shaped nanoparticles/dimers, and by considering also full-retarded dynamics. However, these two scenarios add additional difficulties from the quantization point of view. Indeed, a precise computation of the arbitrarily shaped plasmon modes and energies is more complicated with respect to the case of a sphere, where an analytic solution does exist, and so it is rarely faced [66]. In addition, a correct description of the retardation effects requires the modelling of the interaction between the electrostatic plasmon oscillations and the reservoir of radiative electromagnetic modes. This interaction is often accounted in the form "plasmon annihilation/photon creation" and vice versa [67, 69]. However, more careful analyses have shown that, even to capture the correct retarded behaviour slightly out of the QES regime, a more complex description is needed [70].

All these different approaches, pioneered by the work of Hopfield, are microscopic quantization schemes. They are based on modal expansions and invoke canonical quantization, and they are extremely useful because, often in plasmonics, even in the case of open resonators, the dynamics is dominated by a small number of modes[1]. An alternative macroscopic description based

[1]To deal the open dissipative scenario through a purely electromagnetic approach, a proper

on Green's function is possible [68, 73][2], and it can also be combined with a modal description [72][3].

In this thesis chapter, we discuss the mode quantization of the localized surface plasmons (LSPs) in arbitrarily shaped metal nanoparticles and dimers, in the full-retarded regime. We provide a rigorous canonical quantization scheme whose numerical efficiency does not depend on the shape of the objects. In particular, it is shown the existence of a handy approximation of the complete plasmon-photon Hamiltonian able to describe the retarded quantum dynamics in all the cases of interest for the applications. This approximation is validated over the computation of the radiative decay rate and of the frequency shift that the plasmon oscillations undergo because of radiative effects. These quantities can indeed be computed also within classical electrodynamics. Moreover, our derivation provides explicit and effective formulas to compute the radiative decay rate and the frequency shift of the plasmon excitation that, to the knowledge of the authors, are novel, and that appear to be much more efficient than the available implicit or perturbative method to compute these quantities [25]. As a matter of fact, no full-wave modal expansion is needed but only electrostatic ones.

The treatment is organized as follows. In section 2.1, we present the case of a metal nanoparticle (MNP) in the quasi-electrostatic (QES) limit. In this regime, it is indeed possible to properly define the localized plasmons as bosonic quasi-particles emerging from the collective fluid motion of the electrons inside the nanoparticle. Then, in section 2.2, we overcome this limit and consider the full-retarded case, where the resonance frequencies of the plasmon modes shift and, because of radiation, decay in time. At the quantum level, these phenomenology emerges from the exchange of energy between plasmons and photons. The complete process is described by the plasmon-photon Hamiltonian derived at the end of section 2.2. However, the numerical treatment of this Hamiltonian is not easy and, so, there is the need to introduce approximations. This is done in section 2.3, within the widely used rotating-wave approximation (RWA), and then in section 2.4, going beyond this approximation. In section 2.5 some numerical tests for the arbitrarily shaped case are shown and, in section 2.6, some dimer situations are analyzed.

---

definition of modes is needed. The first chapter is entirely devoted to that.

[2] In the third chapter, it is discussed a case where this Green's function method is needed and modal expansions are highly not recommended.

[3] Quasi normal modes are a possible notion of modes for open systems. They are introduced in the first chapter as a comparison to the material independent modes.

2.1 The plasmon oscillations

Let's consider a metal nanoparticle (MNP) occupying a region $\mathcal{B}$, of surface $\mathcal{S}$, in free space (see figure 2.1). We neglect the collisions of the electrons with the lattice and the band transitions. Thus, the electrons are treated as a fluid moving in a positive charged uniform background. Furthermore, we focus on the linear response of the MNP, and we neglect pressure effects. Under these assumptions, the electron fluid motion results to be incomprehensible, and thus the nanoparticle can exhibit only volume density currents inside $\mathcal{B}$ and surface density charges on $\mathcal{S}$, but no local charge accumulation can take place inside the volume $\mathcal{B}$. In the QES limit, the electric field can be written as the gradient of a scalar potential ϕ, and the system can be described by a Lagrangian made of a term accounting for the kinetic energy of the electrons $\mathcal{L}_A$, a term accounting for the electric energy $\mathcal{L}_B$, and an interaction term $\mathcal{L}_C$:

$$\mathcal{L}_{QES} = \mathcal{L}_A + \mathcal{L}_B + \mathcal{L}_C \tag{2.1}$$

$$\mathcal{L}_A = \int_{\mathcal{B}} \frac{1}{2} m_e n_0 \left(\partial_t \boldsymbol{\zeta}\right)^2 d^3\boldsymbol{r} \tag{2.2}$$

$$\mathcal{L}_B = \int_{\mathbb{R}^3} \frac{\epsilon_0}{2} (\nabla\phi)^2 d^3\boldsymbol{r} \tag{2.3}$$

$$\mathcal{L}_C = e n_0 \int_{\mathcal{S}} \phi \zeta_n d^2\boldsymbol{r}, \tag{2.4}$$

where n_0 is the electron density at rest, $-e$ is the electron charge, m_e is the effective electron mass, $\boldsymbol{\zeta}(\boldsymbol{r}, t)$ is the displacement electron field, ζ_n is the normal component of $\boldsymbol{\zeta}$ on $\mathcal{S}$. The field is determined by the motion of the charges that, in turn, is driven by the field itself. This link can be made explicit observing that the following relation holds (see appendix A):

$$\phi(\boldsymbol{r}) = -\frac{e n_0}{4\pi\epsilon_0} \int_{\mathcal{S}} \frac{\zeta_n(\boldsymbol{r}')}{|\boldsymbol{r} - \boldsymbol{r}'|} d^2\boldsymbol{r}'. \tag{2.5}$$

So, the Lagrangian (2.1)-(2.4) can be re-written only in terms of the displacement field $\boldsymbol{\zeta}$:

$$\mathcal{L}_{QES} = \int_{\mathcal{B}} \frac{1}{2} m_e n_0 \left(\partial_t \boldsymbol{\zeta}\right)^2 d^3\boldsymbol{r} - \frac{e^2 n_0^2}{8\pi\epsilon_0} \int_{\mathcal{S}} \int_{\mathcal{S}} \frac{\zeta_n(\boldsymbol{r})\zeta_n(\boldsymbol{r}')}{|\boldsymbol{r} - \boldsymbol{r}'|} d^2\boldsymbol{r} d^2\boldsymbol{r}'. \tag{2.6}$$

In addition to the incomprehensibility, i.e. $\nabla \cdot \boldsymbol{\zeta} = 0$, in the QES limit the fluid motion is also curl-free, i.e. $\nabla \times \boldsymbol{\zeta} = 0$. Thus, the displacement field is harmonic with normal component on the surface of the MNP different from

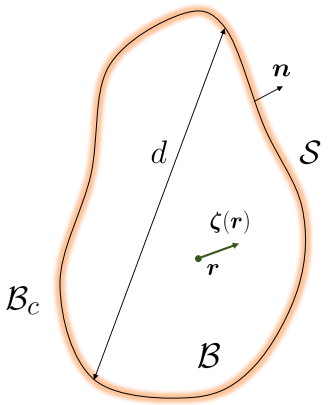

Figure 2.1: Sketch of the metal nanoparticle.

zero, i.e. $\zeta_n \neq 0$ on $\mathcal{S}$. In appendix B, it is shown how to derive a countable basis of modes $\{\boldsymbol{U}_m\}_m$ and a set of frequencies $\{\Omega_m\}_m$ such that, expanding:

$$\boldsymbol{\zeta}(\boldsymbol{r},t) = \sum_m q_m(t)\boldsymbol{U}_m(\boldsymbol{r}) \tag{2.7}$$

into the (2.6), we get:

$$\mathcal{L}_{QES} = \sum_m \left(\frac{M_m \dot{q}_m^2}{2} - \frac{M_m \Omega_m^2 q_m^2}{2} \right), \tag{2.8}$$

where $M_m = m_e n_0 \mathcal{V}_m$, , $\mathcal{V}_m = \langle \boldsymbol{U}_m, \boldsymbol{U}_m \rangle$ and $\langle \boldsymbol{A}, \boldsymbol{B} \rangle = \int_{\mathcal{B}} \boldsymbol{A} \cdot \boldsymbol{B} \; d^3\boldsymbol{r}$. Let's observe that $\{\boldsymbol{U}_m\}_m$ depend on the geometry, while $\{\Omega_m\}_m$ depend both on the geometry and on the material, i.e. on the plasma frequency $\omega_p = \sqrt{\frac{e^2 n_0}{\epsilon_0 m_e}}$.

The (2.8) is the sum of independent harmonic oscillators in the amplitudes $\{q_m\}_m$. These oscillations are the plasmon oscillations, the $\{\boldsymbol{U}_m\}_m$ are the *plasmon fluid modes*, or simply the *plasmon modes*, the $\{\Omega_m\}_m$ are the *plasmon frequencies*, and $\{\mathcal{V}_m\}_m$ and $\{M_m\}_m$ can be respectively called *plasmon volumes* and *plasmon masses*. In the really very low intensity regime, these oscillations are quantized and, if we want to investigate

this fundamental physics, a quantum description of the system must be provided. To do that, we first move to a Hamiltonian description, and then apply a canonical quantization scheme. So, let's first define the conjugate momenta $\left\{p_m = \frac{\partial \mathcal{L}_{QES}}{\partial \dot{q}_m} = M_m \dot{q}_m\right\}_m$ and perform the Legendre transformation of the (2.8):

$$\begin{aligned}\mathcal{H}_{QES}\left(q_m, p_m\right) &= \left[\sum_m p_m \dot{q}_m - \mathcal{L}_{QES}\left(q_m, \dot{q}_m\right)\right]_{q_m, p_m} \\ &= \sum_m \left(\frac{p_m^2}{2M_m} + \frac{M_m \Omega_m^2 q_m^2}{2}\right).\end{aligned} \tag{2.9}$$

Then, let's promote the real amplitudes $\{q_m(t), p_m(t)\}_m$ in the Hamiltonian (2.9) to Hermitian operators $\{\hat{q}_m(t), \hat{p}_m(t)\}_m$ verifying the following commutation relations:

$$[\hat{q}_m(t), \hat{q}_n(t)] = [\hat{p}_m(t), \hat{p}_n(t)] = 0, \quad [\hat{q}_m(t), \hat{p}_n(t)] = i\hbar\delta_{mn}, \tag{2.10}$$

and then define the family of bosonic operators:

$$\begin{aligned}\hat{b}_m &= \frac{1}{2}\left[\sqrt{\frac{2M_m\Omega_m}{\hbar}}\hat{q}_m + i\sqrt{\frac{2}{M_m\Omega_m\hbar}}\hat{p}_m\right] \\ \hat{b}_m^\dagger &= \frac{1}{2}\left[\sqrt{\frac{2M_m\Omega_m}{\hbar}}\hat{q}_m - i\sqrt{\frac{2}{M_m\Omega_m\hbar}}\hat{p}_m\right],\end{aligned} \tag{2.11}$$

that, in turn, verifies:

$$\left[\hat{b}_m(t), \hat{b}_n(t)\right] = \left[\hat{b}_m^\dagger(t), \hat{b}_n^\dagger(t)\right] = 0, \quad \left[\hat{b}_m(t), \hat{b}_n^\dagger(t)\right] = \delta_{mn}. \tag{2.12}$$

The operators $\hat{b}_m^\dagger$ and $\hat{b}_m$ respectively creates and annihilates a quantum of energy $\hbar\Omega_m$, in the oscillating plasmon fluid mode $\boldsymbol{U}_m$. The Hamiltonian (2.9) is now rewritten in this way:

$$\hat{\mathcal{H}}_{EQS} = \sum_m \hbar\Omega_m \left(\hat{b}_m^\dagger \hat{b}_m + \frac{1}{2}\right). \tag{2.13}$$

The quantum state of this system lives in the Fock space of the plasmon oscillations, i.e. the direct sum of the Hilbert spaces where the number of excitation is fixed, and that is spanned by the eigenstates of the Hamiltonian (2.13).

For example, $|n_1\ n_2 \dots\rangle$ is the eigenstate that corresponds to have n_1 excitation in the first plasmon mode, n_2 in the second and so on, and that verifies $\mathcal{H}_{EQS}|n_1\ n_2 \dots\rangle = \hbar\,(n_1\Omega_1 + n_2\Omega_2 + \dots)\,|n_1\ n_2 \dots\rangle$.

The QES limit allows us to give a formal quantum definition of a *localized surface plasmon* or, simply, of a *plasmon*: it is a bosonic quasiparticle describing the collective motion of an electron fluid inside a metal nanoparticle, it has an energy of $\hbar\Omega_m$, a mass of M_m, a volume of $\mathcal{V}_m$, and, in the QES limit, an infinite lifetime[4].

Eventually, for each plasmon oscillation (for each mode), let's introduce the physical object that encodes all the information about its evolution: the plasmon propagator. It is defined as follows:

$$g_m(t) = -\frac{i}{\hbar}\theta(t)\langle\left[\hat{b}_m(t), \hat{b}_m^\dagger(0)\right]\rangle, \tag{2.14}$$

and it is the retarded Green's function[5]:

$$g_{AB}(t) = -\frac{i}{\hbar}\theta(t)\langle\left[\hat{A}(t), \hat{B}(0)\right]\rangle, \tag{2.15}$$

in the operators $A = \hat{b}_m$ and $B = \hat{b}_m^\dagger$. From the Heisenberg equation we get

$$\dot{\hat{b}} = -\frac{i}{\hbar}\left[\hat{b}, \hat{\mathcal{H}}_{QES}\right] = e^{-i\Omega_m t}\hat{b}_m(0), \tag{2.16}$$

and so it follows:

$$g_m(t) = -\frac{i}{\hbar}\theta(t)e^{-i\Omega_m t}, \tag{2.17}$$

that is the evolution of a free (*naked*) propagator.

2.2 Plasmon-photon interaction

The plasmon frequencies $\{\Omega_m\}_m$ depend on the geometry of the MNP but, in general, they are of the same order of magnitude of the plasma frequency ω_p of

[4] It is natural to adapt this definition to the cases where the domain is not finite, e.g. surface plasmon polaritons, or to the case of plasmonic behaviour in objects that are not metals, e.g. graphene.

[5] $\theta(t)$ is the Heaviside step function, i.e. $= 0$ for $t < 0$ and $= 1$ for $t > 1$. The angle brackets represent the average over the initial quantum state. It is worth mentioning that this formalism is extremely powerful at finite temperature. We will use it to study the interaction between plasmons and photons, but it is perfectly suited also for the study of the plasmon-phonon interaction. In this case, the angle brackets would represent the thermal average over the equilibrium state.

the material (see appendix B). Thus, the plasma wavelength $\lambda_p = 2\pi c_0/k_p$ can be used to give a gross regime of validity of the QES discussion. In particular, said d the characteristic length of the nanoparticle, i.e. the maximum distance between two points of the domain, we can assume valid the QES treatment when $d \ll \lambda_p$. As the dimension of the nanoparticle increases, the plasmon excitations couple to the radiation field and decay in time. In other words, they acquire a finite lifetime associated to this radiative damping Γ. Moreover, the characteristic frequencies/energies do not remain the same but they do shift $\Delta\Omega$.

To study the system in this retarded regime, also the vector potential $\boldsymbol{A}(\boldsymbol{r}, t)$ has to be included in the description of the electromagnetic (EM) field. In appendix A it is shown that the full system "MNP+EM" can be described by a Lagrangian made of a free matter term $\mathcal{L}_M$, of a free electromagnetic term $\mathcal{L}_{EM}$, and of an interaction term $\mathcal{L}_I$:

$$\begin{aligned}
\mathcal{L} &= \mathcal{L}_M + \mathcal{L}_{EM} + \mathcal{L}_I && (2.18)\\
\mathcal{L}_M &= \int_{\mathcal{B}} \frac{1}{2} m_e n_0 \left(\partial_t \boldsymbol{\zeta}\right)^2 d^3\boldsymbol{r} && (2.19)\\
&\quad -\frac{e^2 n_0^2}{8\pi\epsilon_0} \int_{\mathcal{S}}\int_{\mathcal{S}} \frac{\zeta_n(\boldsymbol{r})\zeta_n(\boldsymbol{r}')}{|\boldsymbol{r}-\boldsymbol{r}'|} d^2\boldsymbol{r} d^2\boldsymbol{r}' && (2.20)\\
\mathcal{L}_{EM} &= \int_{\mathbb{R}^3} \left[\frac{\epsilon_0}{2}(\partial_t \boldsymbol{A})^2 - \frac{1}{2\mu_0}(\nabla\times\boldsymbol{A})^2\right] d^3\boldsymbol{r} && (2.21)\\
\mathcal{L}_I &= -e n_0 \int_{\mathcal{B}} \boldsymbol{A}\cdot\partial_t\boldsymbol{\zeta} d^3\boldsymbol{r}, && (2.22)
\end{aligned}$$

where we have used the Coulomb gauge ($\nabla\cdot\boldsymbol{A} = 0$).

2.2.1 Matter Lagrangian

Beyond the quasi-static approximation, even if the the electron fluid is still incompressible, it is not curl-free anymore. Nevertheless, it can be written as the sum of a irrotational component, which is the QES one, and of a new rotational component, whose normal derivative on the surface of the nanoparticle is zero. This rotational component can be disregarded in the study of the retardation effects on the plasmon excitations, because it does not affect their dynamics. Thus, we can consider $\mathcal{L}_M = \mathcal{L}_{QES}$ and re-propose the same modal expansion of the QES limit, also in the retarded regime.

2.2.2 Electromagnetic Lagrangian: the photons

The plasmons defined in the QES limit, in the retarded regimes, do not evolve freely anymore. Indeed, they exchange energy with the electromagnetic surrounding. To investigate this mechanism, let's first consider the free electromagnetic Lagrangian as if it were isolated. The vector potential can be expanded in plane waves:

$$\boldsymbol{A}(\boldsymbol{r},t)=\int_{\mathbb{R}_3}\frac{d^3\boldsymbol{q}}{(2\pi)^3}e^{i\boldsymbol{q}\cdot\boldsymbol{r}}\sum_{s=1}^{2}A_{\boldsymbol{q},s}(t)\boldsymbol{e}_{\boldsymbol{q},s}. \tag{2.23}$$

For each wave vector $\boldsymbol{q}$, two orthogonal polarizations $\boldsymbol{e}_{\boldsymbol{q},1}$ and $\boldsymbol{e}_{\boldsymbol{q},2}$ are chosen in such a way that $\boldsymbol{e}_{-\boldsymbol{q},s}=\boldsymbol{e}_{\boldsymbol{q},s}$. Moreover, let's observe that, in order $\boldsymbol{A}(\boldsymbol{r},t)$ to be real, we have $A_{-\boldsymbol{q},s}=A^*_{\boldsymbol{q},s}$. Exploiting the property:

$$\int_{\mathbb{R}^3}\frac{d^3\boldsymbol{r}}{(2\pi)^3}e^{i(\boldsymbol{q}-\boldsymbol{q}')\cdot\boldsymbol{r}}=\delta_{\boldsymbol{q},\boldsymbol{q}'}, \tag{2.24}$$

the (2.21) can be rewritten as an uncountable sum of harmonic oscillators:

$$\mathcal{L}_{EM}=\int_{\mathbb{R}_3}\frac{d^3\boldsymbol{q}}{(2\pi)^3}\sum_{s=1}^{2}\left[\frac{\epsilon_0|\dot{A}_{q,s}|^2}{2}-\frac{\epsilon_0\omega_q^2\,|A_{q,s}|^2}{2}\right]. \tag{2.25}$$

Defining the conjugate momenta $\left\{\Pi_{\boldsymbol{q},s}=\frac{\partial\mathcal{L}_{EM}}{\partial\dot{A}^*_{\boldsymbol{q},s}}=\epsilon_0\dot{A}_{\boldsymbol{q},s}\right\}_{\boldsymbol{q},s}$ and performing the Legendre transformation:

$$\begin{aligned}\mathcal{H}_{EM}\left(A_{\boldsymbol{q},s},\Pi_{\boldsymbol{q},s}\right)=\Bigg[&\int_{\mathbb{R}_3}\frac{d^3\boldsymbol{q}}{(2\pi)^3}\sum_{s=1}^{2}\Pi_{\boldsymbol{q},s}\dot{A}^*_{\boldsymbol{q},s}\\&-\mathcal{L}_{EM}\left(A_{\boldsymbol{q},s},\dot{A}_{\boldsymbol{q},s}\right)\Bigg]_{A_{\boldsymbol{q},s},P_{\boldsymbol{q},s}},\end{aligned} \tag{2.26}$$

we get:

$$\mathcal{H}_{EM}=\int_{\mathbb{R}_3}\frac{d^3\boldsymbol{q}}{(2\pi)^3}\sum_{s=1}^{2}\left[\frac{|\Pi_{q,s}|^2}{2\epsilon_0}+\frac{\epsilon_0\omega_q^2\,|A_{q,s}|^2}{2}\right]. \tag{2.27}$$

Now, the canonical quantization procedure tells us to promote the electromagnetic amplitudes $\{A_{\boldsymbol{q},s},\Pi_{\boldsymbol{q},s}\}_{\boldsymbol{q},s}$ to Hermitian operators, veryfing the following commutation relation rules:

$$\begin{aligned}\left[\hat{A}_{\boldsymbol{q},s}(t),\hat{A}_{\boldsymbol{q}',s'}(t)\right]&=\left[\hat{\Pi}_{\boldsymbol{q},s}(t),\hat{\Pi}_{\boldsymbol{q}',s'}(t)\right]=0,\\\left[\hat{A}^\dagger_{\boldsymbol{q},s}(t),\hat{\Pi}_{\boldsymbol{q}',s'}(t)\right]&=i\hbar\delta_{\boldsymbol{q},\boldsymbol{q}'}\delta_{s,s'}.\end{aligned} \tag{2.28}$$

Then, defining the creation/annihilation bosonic operators for the electromagnetic field:

$$\begin{aligned}\hat{a}_{\boldsymbol{q},s} &= \frac{1}{2}\left[\sqrt{\frac{2\epsilon_0\omega_q}{\hbar}}\hat{A}_{\boldsymbol{q},s} + i\sqrt{\frac{2}{\hbar\epsilon_0\omega_q}}\hat{\Pi}_{\boldsymbol{q},s}\right] \\ \hat{a}^\dagger_{-\boldsymbol{q},s} &= \frac{1}{2}\left[\sqrt{\frac{2\epsilon_0\omega_q}{\hbar}}\hat{A}_{\boldsymbol{q},s} - i\sqrt{\frac{2}{\hbar\epsilon_0\omega_q}}\hat{\Pi}_{\boldsymbol{q},s}\right],\end{aligned} \tag{2.29}$$

that, in turn, verify:

$$\begin{aligned}\left[\hat{a}_{\boldsymbol{q},s}(t), \hat{a}_{\boldsymbol{q}',s'}(t)\right] &= \left[\hat{a}^\dagger_{\boldsymbol{q},s}(t), \hat{a}^\dagger_{\boldsymbol{q}',s'}(t)\right] = 0, \\ \left[\hat{a}_{\boldsymbol{q},s}(t), \hat{a}^\dagger_{\boldsymbol{q}',s'}(t)\right] &= \delta_{\boldsymbol{q},\boldsymbol{q}'}\delta_{s,s'},\end{aligned} \tag{2.30}$$

the (2.27) can be rewritten as:

$$\hat{\mathcal{H}}_{EM} = \int_{\mathbb{R}_3}\frac{d^3\boldsymbol{q}}{(2\pi)^3}\sum_{s=1}^{2}\hbar\omega_q\left(\hat{a}^\dagger_{\boldsymbol{q},s}\hat{a}_{\boldsymbol{q},s} + \frac{1}{2}\right). \tag{2.31}$$

In this derivation, the plane waves are the electromagnetic modes in which we expand the field, and the electromagnetic energy of each plane wave is an integer multiple of the single excitation energy $\hbar\omega_q$. These single excitations are the *photons*, i.e. elementary bosonic particles that mediate the electromagnetic interaction. The operators $\hat{a}^\dagger_{\boldsymbol{q},s}$ and $\hat{a}_{\boldsymbol{q},s}$ create and annihilate, respectively, a photon of energy $\hbar\omega_q$ in a plane wave of wave vector $\boldsymbol{q}$ and polarization s. The (2.31) acts on the Fock space of the electromagnetic field, i.e. the direct sum of the Hilbert spaces of fixed number of photons, spanned by its eigenvectors. For example, $|n_{\boldsymbol{q}_1,s}\, n_{\boldsymbol{q}_2,s}\, \ldots\rangle$ is the eigenstate that correspond to have $n_{\boldsymbol{q}_1,s}$ excitations in the plane wave $(\boldsymbol{q}_1, s)$, $n_{\boldsymbol{q}_2,s}$ excitations in the plane wave $(\boldsymbol{q}_2, s)$ and so on, and that verifies $\mathcal{H}_{EM}|n_{\boldsymbol{q}_1,s}\, n_{\boldsymbol{q}_2,s}\, \ldots\rangle = \hbar\left(n_{\boldsymbol{q}_1,s}\omega_{\boldsymbol{q}_1} + n_{\boldsymbol{q}_2,s}\omega_{\boldsymbol{q}_2} + \ldots\right)|n_{\boldsymbol{q}_1,s}\, n_{\boldsymbol{q}_2,s}\, \ldots\rangle$.

2.2.3 Plasmon-photon Hamiltonian

Once that plasmons and photons have been independently introduced, we can investigate how they interact and, in particular, how this interaction affects the plasmon dynamics. To do that, we have to derive the full plasmon-photon Hamiltonian. So, let's now deal with the complete description (2.18)-(2.22).

Exploiting the harmonic expansion (2.7) of $\boldsymbol{\zeta}$ and the plane waves expansion (2.23) of $\boldsymbol{A}$, the interaction Lagrangian (2.22) reads:

$$\mathcal{L}_I = -en_0 \sum_n \int_{\mathbb{R}_3} \frac{d^3\boldsymbol{q}}{(2\pi)^3} \sum_{s=1}^{2} U^*_{n,s}(\boldsymbol{q}) A_{\boldsymbol{q},s}(t) \dot{q}_n(t), \tag{2.32}$$

where

$$\boldsymbol{U}_n(\boldsymbol{q}) = \int_{\mathcal{B}} d^3\boldsymbol{q} e^{-i\boldsymbol{q}\cdot\boldsymbol{r}} \boldsymbol{U}_n(\boldsymbol{r}) \quad \text{and} \quad U_{n,s}(\boldsymbol{q}) = \boldsymbol{U}_n(\boldsymbol{q}) \cdot \boldsymbol{e}_{\boldsymbol{q},s}. \tag{2.33}$$

Defining the conjugate momenta

$$\Pi_{\boldsymbol{q},s} = \frac{\partial \mathcal{L}}{\partial \dot{A}^*_{\boldsymbol{q},s}} = \frac{\mathcal{L}_{EM}}{\partial \dot{A}^*_{\boldsymbol{q},s}} = \epsilon_0 A_{\boldsymbol{q},s}, \tag{2.34}$$

and

$$p_m = \frac{\partial \mathcal{L}}{\partial \dot{q}_m} = M_m \dot{q}_m - en_0 \int_{\mathbb{R}_3} \frac{d^3\boldsymbol{q}}{(2\pi)^3} \sum_{s=1}^{2} U^*_{m,s}(\boldsymbol{q}) A_{\boldsymbol{q},s}(t) \neq \frac{\partial \mathcal{L}_{QES}}{\partial \dot{q}_m}. \tag{2.35}$$

By using the following Legendre transformation:

$$\begin{aligned} \mathcal{H}\left(q_m, p_m, A_{\boldsymbol{q},s}, \Pi_{\boldsymbol{q},s}\right) = \Bigg[& \sum_m p_m \dot{q}_m + \int_{\mathbb{R}_3} \frac{d^3\boldsymbol{q}}{(2\pi)^3} \sum_{s=1}^{2} \Pi_{\boldsymbol{q},s} \dot{A}^*_{\boldsymbol{q},s} \\ & - \mathcal{L}\left(q_m, \dot{q}_m, A_{\boldsymbol{q},s}, \dot{A}_{\boldsymbol{q},s}\right) \Bigg]_{q_m, p_m, A_{\boldsymbol{q},s}, \Pi_{\boldsymbol{q},s}}, \end{aligned} \tag{2.36}$$

combined with (2.34)-(2.35), we get

$$\hat{\mathcal{H}} = \hat{\mathcal{H}}_M + \hat{\mathcal{H}}_{EM} + \hat{\mathcal{H}}_I + \hat{\mathcal{H}}_{II}, \tag{2.37}$$

where $\hat{\mathcal{H}}_M$ and $\hat{\mathcal{H}}_{EM}$ are the same of (2.9) and (2.27), and

$$\mathcal{H}_I = \sum_m \int_{\mathbb{R}_3} \frac{d^3\boldsymbol{q}}{(2\pi)^3} \sum_{s=1} \frac{en_0}{M_m} p_m U^*_{m,s}(\boldsymbol{q}) A_{\boldsymbol{q},s}(t) \tag{2.38}$$

$$\mathcal{H}_{II} = \sum_m \frac{en_0^2}{2M_m} \left(\int_{\mathbb{R}_3} \frac{d^3\boldsymbol{q}}{(2\pi)^3} \sum_{s=1} U^*_{m,s}(\boldsymbol{q}) A_{\boldsymbol{q},s}(t) \right)^2. \tag{2.39}$$

Rewriting the (2.37) in terms of the creation/annihilation operators (2.11) and (2.29), the Hamiltonian reads[6]:

$$\hat{\mathcal{H}} = \hat{\mathcal{H}}_M + \hat{\mathcal{H}}_{EM} + \hat{\mathcal{H}}_I + \hat{\mathcal{H}}_{II} \tag{2.40}$$

$$\hat{\mathcal{H}}_M = \sum_m \hbar\Omega_m \left(\hat{b}_m^\dagger \hat{b}_m + \frac{1}{2}\right) \tag{2.41}$$

$$\hat{\mathcal{H}}_{EM} = \int_{\mathbb{R}_3} \frac{d^3\boldsymbol{q}}{(2\pi)^3} \sum_{s=1}^{2} \hbar\omega_q \left(\hat{a}_{\boldsymbol{q},s}^\dagger \hat{a}_{\boldsymbol{q},s} + \frac{1}{2}\right) \tag{2.42}$$

$$\hat{\mathcal{H}}_I = \sum_m \int_{\mathbb{R}_3} \frac{d^3\boldsymbol{q}}{(2\pi)^3} \sum_{s=1}^{2} \left[V_{\boldsymbol{q},s}^m \left(\hat{b}_m^\dagger - \hat{b}_m\right) a_{\boldsymbol{q},s} + h.c.\right] \tag{2.43}$$

$$\begin{aligned}\hat{\mathcal{H}}_{II} = \int_{\mathbb{R}_3} \frac{d^3\boldsymbol{q}'}{(2\pi)^3} \int_{\mathbb{R}_3} \frac{d^3\boldsymbol{q}}{(2\pi)^3} \sum_{s=1}^{2}\sum_{s'=1}^{2} \Big[&W_{\boldsymbol{q},\boldsymbol{q}'}^{s,s'} \hat{a}_{\boldsymbol{q},s}\hat{a}_{\boldsymbol{q}',s'} \\ &+ G_{\boldsymbol{q},\boldsymbol{q}'}^{s,s'} \hat{a}_{\boldsymbol{q},s}\hat{a}_{\boldsymbol{q}',s'}^\dagger + h.c.\Big]\end{aligned} \tag{2.44}$$

where

$$V_{\boldsymbol{q},s}^m = i\frac{\hbar\omega_p}{2}\sqrt{\frac{\Omega_m}{\mathcal{V}_m}}\frac{1}{\sqrt{\omega_q}} U_{m,s}^*(\boldsymbol{q}), \tag{2.45}$$

$$W_{\boldsymbol{q},\boldsymbol{q}'}^{s,s'} = \frac{\hbar^2}{4}\frac{\omega_p^2}{\sqrt{\omega_q\omega_{q'}}}\eta(\boldsymbol{q}+\boldsymbol{q}')\boldsymbol{e}_{\boldsymbol{q},s}\cdot\boldsymbol{e}_{\boldsymbol{q}',s'},$$

$$G_{\boldsymbol{q},\boldsymbol{q}'}^{s,s'} = W_{\boldsymbol{q},-\boldsymbol{q}'}^{s,s'}, \tag{2.46}$$

and η is the characteristic function of the set, i.e. $\eta(\boldsymbol{r}) = 1$ if $\boldsymbol{r} \in \mathcal{B}$ and $\eta(\boldsymbol{r}) = 0$ otherwise. Let's notice that $V_{-\boldsymbol{q},s}^m = -V_{\boldsymbol{q},s}^{m*}$.

The (2.40)-(2.44) is the plasmon-photon Hamiltonian. It describes, at the quantum level, the coupling between the electron fluid oscillations, namely

[6] In the derivation there is the need to use the following decomposition of the identity $\sum_m \boldsymbol{U}_m(\boldsymbol{r}) \bigotimes \boldsymbol{U}_m(\boldsymbol{r}')/\mathcal{V}_m = \delta(\boldsymbol{r}-\boldsymbol{r}')\mathbf{1}$. This decomposition is exact only in the subspace of the harmonic modes where we are solving the dynamics. The full decomposition would involve also the rotational modes. There is an equivalent method to derive the Hamiltonian (2.40)-(2.44), that does not need this tricky algebra. It works directly with the displacement and with the electromagnetic fields expliciting their modal expansions only at the end. However, this method involves the use of functional derivatives and the quantization of fields in real space, that are mathematical tools slightly more advanced. This other derivation is sketched in appendix C.

the plasmonic oscillation, and the radiative electromagnetic field, in the full retarded regime. It is made of four terms: the two free terms $\hat{\mathcal{H}}_M$ and $\hat{\mathcal{H}}_{EM}$, an interaction term $\hat{\mathcal{H}}_I$ accounting for the exchange of energy between plasmons and photons, and a second order correction of the electromagnetic energy $\hat{\mathcal{H}}_{II}$, due to the presence of the MNP. This Hamiltonian acts on the plasmon-photon Fock space that is the direct sum of fixed number excitation Hilbert spaces.

This Hamiltonian encodes the physics of the radiative plasmon dynamics in the full retarded regime, at the quantum level. Thus, it might be suited for all the scenarios where plasmon nanoparticles are driven in very low intensity regimes, e.g. interaction with simple quantum dipoles or with complex molecules. In particular, it could give some new insights, especially in strong coupling scenarios, where the quantization of the electromagnetic fields is mandatory.

Nevertheless, dealing with this Hamiltonian is not straightforward and, in the following, we discuss some possible approximations. In particular, we show that, in the majority of cases of interest for applications, H_{II} can be neglected and, moreover, that the plasmon modes can be considered as independent. It is to say that to study the dynamics of a given mode m, the full Hamiltonian (2.40)-(2.44) can be replaced with a single mode one, because the cross-talk with the other modes turns out to be negligible[7]. To validate the approximations, we compute the energy/frequency shifts and the radiative decay rates of the plasmon excitations, due to the plasmon-photon coupling. We will use the sphere case as a test-case scenario, where an analytic treatment is possible (see appendix E). Eventually, these careful analyses will allow us to provide closed formulas for these physical quantities that, to the knowledge of the authors, are somehow novel.

2.3 Rotating-wave approximation

The simplest Hamiltonian able to describe the dynamics is a single plasmon mode Hamiltonian, made of the free plasmon component, of the free electromagnetic component, and of the minimal interaction we can imagine "photon-

[7] This analysis can be found in [74].

annihilation/plasmon-creation" and vice versa:

$$\begin{aligned}\hat{\mathcal{H}}_m = \hbar\Omega_m \hat{b}_m^\dagger \hat{b}_m + \int_{\mathbb{R}_3} \frac{d^3\boldsymbol{q}}{(2\pi)^3} \sum_{s=1}^{2} \hbar\omega_q \hat{a}_{\boldsymbol{q},s}^\dagger \hat{a}_{\boldsymbol{q},s} \\ + \int_{\mathbb{R}_3} \frac{d^3\boldsymbol{q}}{(2\pi)^3} \sum_{s=1}^{2} \left[V_{\boldsymbol{q},s}^m \, \hat{b}_m^\dagger \, \hat{a}_{\boldsymbol{q},s} + V_{\boldsymbol{q},s}^{m*} \, \hat{b}_m \, \hat{a}_{\boldsymbol{q},s}^\dagger \right].\end{aligned} \tag{2.47}$$

The (2.47) is obtained from the (2.40) assuming the modes as independent, neglecting $\mathcal{H}_{II}$ and, in particular, performing the so called rotating-wave approximation, i.e. neglecting the double-creation $\hat{b}_m^\dagger \hat{a}_{\boldsymbol{q},s}^\dagger$ and the double-annihilation $\hat{b}_m \hat{a}_{\boldsymbol{q},s}$ terms in the interaction. The RWA is widely diffused in quantum optics, since these terms tend to oscillate much more rapidly, i.e. $\sim e^{\pm i(\Omega_m+\omega_q)t}$, than the others, i.e. $\sim e^{\pm i(\Omega_m-\omega_q)t}$ [75]. So, the dynamics is somehow coarse-grained to a larger time scale and, most of the times, this is perfectly compatible with the finite resolution of the detectors.

To compute the plasmon propagator, let's consider the following rotated Laplace transform of a generic retarded Green's function (2.15):

$$G_{AB}(z) = \int_{-\infty}^{\infty} g_{AB}(t) e^{izt} \, dt, \tag{2.48}$$

which is analytic in the half-plane $Im[z] > 0$, and whose inverse Laplace transform is:

$$g_{AB}(t) = \int_{ia-\infty}^{ia+\infty} G_{AB}(z) e^{izt} \, \frac{dz}{2\pi i}, \tag{2.49}$$

with $a > 0$. Applying the integration by part and using the Heisenberg equation $\dot{\hat{A}} = -\frac{i}{\hbar}\left[\hat{A}, \hat{\mathcal{H}}\right]$, the (2.48) can be rewritten as follows:

$$G_{AB}(z) = -\frac{\tilde{g}(0)}{iz} + \frac{g_{[\hat{A},H],\hat{B}}(z)}{\hbar z}, \tag{2.50}$$

where

$$\tilde{g}(t) = -\frac{i}{\hbar}\langle \hat{A}(t), \hat{B}(0) \rangle. \tag{2.51}$$

In the EQS case, we have $G_m^{(0)} = [\hbar\,(z - \Omega_m)]^{-1}$, whose inverse Laplace transform is (2.17), and where the apex 0 is used to remember that this propagator is computed without interaction.

As shown in appendix D, the Laplace transform of the dressed propagator g_m, in the rotating wave scenario, can be computed by iteratively applying the property (2.50). It results (see appendix D):

$$G_m(z) = \frac{1}{\hbar z - (\hbar\Omega_m + \Sigma_m^{RWA}(z))}, \tag{2.52}$$

where we have introduced the self-energy of the m-th plasmon mode:

$$\Sigma_m^{RWA}(z) = \frac{1}{\hbar}\int_{\mathbb{R}_3} \frac{d^3\boldsymbol{q}}{(2\pi)^3} \sum_{s=1}^{2} \frac{\left|V_{\boldsymbol{q},s}^m\right|^2}{z - \omega_q}. \tag{2.53}$$

This technique of computing the propagator, since it directly uses the Heisenberg equations, is sometimes called *equation of motion method*.

2.3.1 Dyson's equation

The (2.52) is a particular case of a general expression that the Laplace transform of any propagator, i.e. any $g_{AA^\dagger}$, has. Indeed, it can be proved that any propagator solves the Dyson's equation [76, 77]:

$$G(z) = G^{(0)}(z) + G^{(0)}(z)\Sigma(z)G(z), \tag{2.54}$$

and, assuming $G^{(0)}(z) = \hbar\left[z - \Omega\right]^{-1}$, the (2.54) becomes:

$$G(z) = \frac{1}{\hbar z - (\hbar\Omega + \Sigma(z))}. \tag{2.55}$$

The self-energy $\Sigma(z)$ is a physical quantity that encodes all the interactions of the excitation under investigation with the surrounding environment. Moreover, the dynamics of the excitation at a given time t is, in principle, determined not only by the interactions at time t, but also by the past interactions, as it can be seen from the convolution integral that appears in the inverse Laplace transform of the (2.55):

$$\dot{g} + i\Omega g + \frac{i}{\hbar}\int_0^t \Sigma(t-\tau)g(\tau)d\tau = -\frac{i}{\hbar}\delta(t). \tag{2.56}$$

In many systems of physical interest, these past contributions are, in truth, irrelevant to the dynamics. In these cases, the correct results can be obtained performing an approximation on the dynamical equations that makes the evolution local in time. A dynamics where the past contributions are neglected is

usually called Markovian, and there is not a unique way to derive a Markovian dynamics. A way to do that is to formally substitute $\Sigma(z)$ with its value in the free pole Ω. Indeed, the major contributes to the dynamics come from the frequencies close to free pole and, for this kind of systems, the $\Sigma(z)$ generally varies slowly around it. Thus, it results:

$$\begin{aligned} g_{AB}(t) &= \int_{a-i\infty}^{a+i\infty} \frac{e^{izt}}{\hbar z - (\hbar\Omega + \Sigma(z))} \frac{dz}{2\pi i} \\ &\approx \int_{a-i\infty}^{a+i\infty} \frac{e^{izt}}{\hbar z - (\hbar\Omega + \Sigma(\Omega))} \frac{dz}{2\pi i}. \end{aligned} \tag{2.57}$$

This assumption is equivalent to assume instantaneous interactions in the time domain, i.e. $\Sigma(t) = \delta(t)\Sigma(\Omega)$, and so it brings to the following Markovian evolution:

$$\dot{g} + i\Omega g + \frac{i}{\hbar}\Sigma(\Omega)g = -\frac{i}{\hbar}\delta(t), \tag{2.58}$$

whose solution is:

$$g(t) = -\frac{i}{\hbar}\theta(t)e^{-i[\Omega+\Sigma(\Omega)]t} = -\frac{i}{\hbar}\theta(t)e^{-i[\Omega+\Delta\Omega]t}e^{-\Gamma t}. \tag{2.59}$$

Within these assumptions, the frequency shift is given by the real part of the self energy $\Delta\Omega = Re[\Sigma(\Omega)]/\hbar$, and the decay rate by its imaginary part $\Gamma = Im[\Sigma(\Omega)]/\hbar$.

Let's observe that this *pole approximation* must be computed carefully. As a matter of fact, the $G(z)$ is not analytic in the whole complex plane. Thanks to the presence of $\theta(t)$ in the definition of the retarded Green's function (2.15), we can only be sure that $G(z)$ is analytic in the half-plane of $Im[z] > 0$. Thus, the limit must be done from above, namely:

$$\Sigma(\Omega) = \lim_{\eta\to 0^+} \Sigma(\Omega + i\eta). \tag{2.60}$$

2.3.2 Retarded plasmons

In the case of the plasmon dynamics that we are studying, the approximation (2.57) can be done. From the physical point of view, this can be understood observing that the possible past interactions, which could drive the dynamics of the plasmon excitation at time t, have a very low probability to occur. Indeed, let's for example imagine that the plasmon excitation m, decaying at time $t' < t$, emits a photon of energy $\hbar\Omega_m$. Immediately after the emission, this photon

will propagate away from the nanoparticle at the speed of light. Thus, the chances for the photon to be reabsorbed at time t are essentially zero. The situation radically can change if, for example, we place the nanoparticle close to a photonic crystal, where the photon dispersion relation can be tailored to slow down the propagation speed of the emitted photons and increasing the probability of detecting non-Markovian behaviours. Mathematically, the major contributions to the inverse transform integral come from the z close to Ω_m, and the self-energy (2.53) slowly varies around Ω_m. Applying the (2.60) to the (2.53), we get:

$$\Sigma_m^{RWA}(\Omega_m) = \frac{1}{\hbar}\int_{\mathbb{R}_3}\frac{d^3\boldsymbol{q}}{(2\pi)^3}\sum_{s=1}^{2}\left|V_{\boldsymbol{q},s}^m\right|^2\left(p.v.\frac{1}{\Omega_m-\omega_q}-i\pi\delta(\Omega_m-\omega_q)\right), \tag{2.61}$$

since

$$\lim_{\eta\to 0}\frac{1}{x+i\eta} = \frac{x}{x^2+\eta^2} - i\pi\left[\frac{1}{\pi}\frac{\eta}{x^2+\eta^2}\right] = p.v.\left[\frac{1}{x}\right] - i\pi\delta(x). \tag{2.62}$$

Thus, in this retarded regime, the dressed propagator evolves as follows:

$$g_m(t) = -\frac{i}{\hbar}\theta(t)e^{-i[\Omega_m+\Sigma(\Omega_m)]t} = -\frac{i}{\hbar}\theta(t)e^{-i[\Omega_m+\Delta\Omega_m]t}e^{-\Gamma_m t}. \tag{2.63}$$

Differently from the QES case, the m-th plasmon mode has a finite lifetime given by the inverse of the radiative decay rate:

$$\Gamma_m = \frac{1}{\hbar}Im\left[\Sigma_m^{RWA}(\Omega_m)\right] = \frac{\pi}{\hbar^2}\int_{\mathbb{R}_3}\frac{d^3\boldsymbol{q}}{(2\pi)^3}\sum_{s=1}^{2}\left|V_{\boldsymbol{q},s}^m\right|^2\delta(\Omega_m-\omega_q), \tag{2.64}$$

and its resonance frequency is shifted of:

$$\Delta\Omega_m = \frac{1}{\hbar}Re\left[\Sigma_m^{RWA}(\Omega_m)\right] = \frac{1}{\hbar^2}p.v.\int_{\mathbb{R}_3}\frac{d^3\boldsymbol{q}}{(2\pi)^3}\sum_{s=1}^{2}\frac{\left|V_{\boldsymbol{q},s}^m\right|^2}{\Omega_m-\omega_q}, \tag{2.65}$$

where $p.v.$ indicates that the integral is a Cauchy principal value integral.

Numerical results for a metal sphere

In figure 2.2, we show how the radiative decay rate and the frequency shift of the plasmon modes in a metal sphere change with the increasing of the sphere's dimension. We compare the RWA predictions with the Mie theory calculation

showed in appendix E. We see that, although the RWA qualitative well describes the plasmon dynamics, its quantitative predictions are unsatisfactory. In particular, it fails to predict the correct values of the frequency shift in the retarded-regime, even for small particles. And thus, it won't be able to faithfully reproduce the retarded dynamics in the important case of MNPs slightly out of the QES limit.

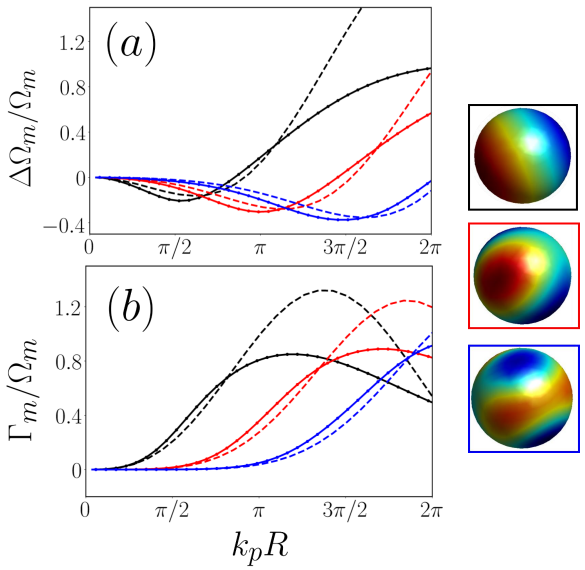

Figure 2.2: Frequency shift (a) and radiative decay rate (b) of the three dipoles (black), of the five quadrupoles (red), and of the seven octupoles (blue) of a metal sphere. The surface charge density of each mode is shown in a box whose color matches the one of the corresponding curves. Comparison between the RWA predictions (dashed lines) of (2.64)-(2.65) and the electrodynamical ones (dotted solid lines) of appendix E, which are based on Mie theory. R is the radius of the sphere and $k_p = 2\pi/\lambda_p$.

2.4 Beyond the rotating-wave approximation

In this section, we go beyond the rotating-wave approximation and show that it is easily possible to fill its shortcomings considering the following Hamilto-

nian:

$$\begin{aligned}\hat{\mathcal{H}}_m = \hbar\Omega_m \hat{b}_m^\dagger \hat{b}_m + \int_{\mathbb{R}_3} \frac{d^3\boldsymbol{q}}{(2\pi)^3} \sum_{s=1}^{2} \hbar\omega_q \hat{a}_{\boldsymbol{q},s}^\dagger \hat{a}_{\boldsymbol{q},s} \\ + \sum_m \int_{\mathbb{R}_3} \frac{d^3\boldsymbol{q}}{(2\pi)^3} \sum_{s=1}^{2} \left[V_{\boldsymbol{q},s}^m \left(\hat{b}_m^\dagger - \hat{b}_m \right) a_{\boldsymbol{q},s} + h.c. \right].\end{aligned} \tag{2.66}$$

The equation of motion method can again be applied to compute the dressed propagator. It leads to the following system:

$$\hbar z G_m(z) = 1 + \hbar\Omega_m G_m(z) + \Psi_m(z)\left[G_m(z) - H_m(z)\right] \tag{2.67}$$

$$\hbar z H_m(z) = -\hbar\Omega_m H_m(z) + \Psi_m(z)\left[G_m(z) - H_m(z)\right], \tag{2.68}$$

where $H_m(z)$ is the Laplace transform of the Green's function:

$$h_m(t) = -\frac{i}{\hbar}\theta(t)\langle\left[\hat{b}_m^\dagger(t), \hat{b}_m^\dagger(0)\right]\rangle, \tag{2.69}$$

and

$$\Psi_m(z) = \frac{1}{\hbar}\int_{\mathbb{R}_3} \frac{d^3\boldsymbol{q}}{(2\pi)^3} \sum_{s=1}^{2} \left|V_{\boldsymbol{q},s}^m\right|^2 \left(\frac{1}{z-\omega_q} - \frac{1}{z+\omega_q} \right). \tag{2.70}$$

As in the above discussed RWA case, also here it is possible to neglect the memory effects and to solve a Markovian dynamics instead. Here, we formally substitute $\Psi(z)$ with its value in the free pole Ω_m. Thus we get (see appendix D):

$$\hbar z G_m(z) = 1 + \hbar\Omega_m G_m(z) + \Psi_m(\Omega_m)\left[G_m(z) - H_m(z)\right] \tag{2.71}$$

$$\hbar z H_m(z) = -\hbar\Omega_m H_m(z) + \Psi_m(\Omega_m)\left[G_m(z) - H_m(z)\right], \tag{2.72}$$

where:

$$\begin{aligned}\Psi_m(\Omega_m) = \frac{1}{\hbar}\int_{\mathbb{R}_3} \frac{d^3\boldsymbol{q}}{(2\pi)^3} \sum_{s=1}^{2} \left|V_{\boldsymbol{q},s}^m\right|^2 \left(p.v.\frac{1}{\Omega_m - \omega_q} \right. \\ \left. - \frac{1}{\Omega_m + \omega_q} - i\pi\delta(\Omega_m - \omega) \right).\end{aligned} \tag{2.73}$$

Within this approximation, the time dynamics is described by the following system of differential equations:

$$\dot{g}_m(t) + i\Omega_m g_m(t) + \frac{i}{\hbar}\Psi_m(\Omega_m)\left[g_m(t) - h_m(t)\right] = -\frac{i}{\hbar}\delta(t) \tag{2.74}$$

$$\dot{h}_m(t) - i\Omega_m h_m(t) + \frac{i}{\hbar}\Psi_m(\Omega_m)\left[g_m(t) - h_m(t)\right] = 0, \tag{2.75}$$

whose eigenvalues are

$$\lambda = \pm\Omega_m \sqrt{1 + \frac{2}{\hbar}\frac{\Psi(\Omega_m)}{\Omega_m}}. \tag{2.76}$$

From the (2.76), we derive the following frequency shifts and radiative decay rates:

$$\begin{aligned} \Delta\Omega_m &= Re\left[\Omega_m \sqrt{1 + \frac{2}{\hbar}\frac{\Psi(\Omega_m)}{\Omega_m}}\right] \\ \Gamma_m &= -Im\left[\Omega_m \sqrt{1 + \frac{2}{\hbar}\frac{\Psi(\Omega_m)}{\Omega_m}}\right]. \end{aligned} \tag{2.77}$$

Numerical results for a metal sphere

In figure 2.3, we show the values of the radiative decay rate and of the frequency shift given by (2.77). By comparing them with the purely electrodynamical computations of appendix E, we find that the agreement is greatly improved compared to the RWA case. In particular, it can be considered exact for $k_p R \leq \pi$. This range of validity is sufficiently large to encourage the use of the Hamiltonian (2.66) in all the cases of practical interest. For gold nanoparticles $\omega_p \simeq 1.37 * 10^{16}$, and so this constraint corresponds to a radius of 144 nm; for silver nanopraticle $\omega_p \simeq 2.17 * 10^{15}$, and so $R = 230$ nm. These spheres are larger than to the usual dimensions of nanoparticles used in plasmonics.

It proves that the Hamiltonian (2.66) correctly predicts the radiative decay rate and the frequency shift that each plasmon mode of an isolated sphere experiences because of retardation effects. These quantities constitutes the eigenvalues of the free evolution, and from them the dynamics can always be reconstructed.

It is important to observe that the classical method of appendix E, which we are using as a comparison, is trivial only in the analytic sphere case, but its extension to arbitrarily shaped MNPs, or to dimers gets immediately much more complex. Indeed, it turns into the challenging numerical problem of finding a suitable electromagnetic modal expansion for the scattering in the full-retarded regime and then studying the resonance conditions. On the contrary, the (2.77) are handy and direct expressions for $\Delta\Omega$ and Γ in the full-retarded

regime, and *they only use QES modal decompositions*. The available perturbative techniques to compute these quantities that resort only to QES modal expansions are manageable slightly out of the QES limit, i.e. to compute the first corrections to these quantities, but become more and more complex as the dimension of the nanoparticle increases [25]. The complexity of the (2.77) does not depend on the dimension of the nanoparticle.

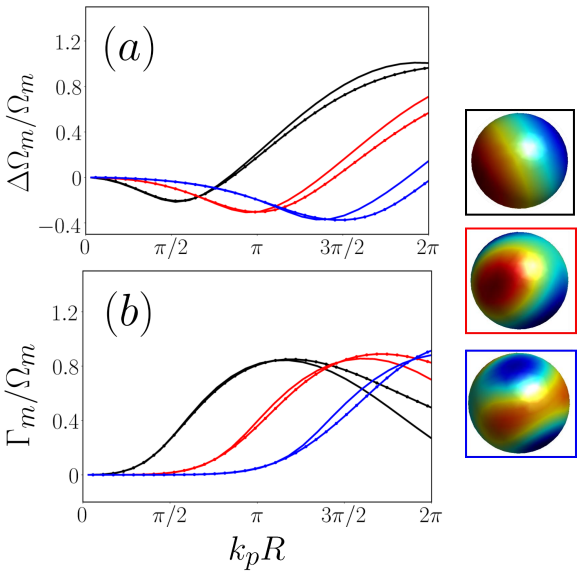

Figure 2.3: Frequency shift (a) and radiative decay rate (b) of the three dipoles (black), of the five quadrupoles (red), and of the seven octupoles (blue) of a metal sphere. The surface charge density of each mode is shown in a box whose color matches the one of the corresponding curves. Comparison between the theoretical prediction (dashed lines) of (2.77), which are derived from (2.66) beyond the RWA, and the electrodynamical results (dotted solid lines) of appendix E, which are based on Mie theory. R is the radius of the sphere and $k_p = 2\pi/\lambda_p$.

2.5 Arbitrarily shaped nanoparticles

The spherical case is an important scenario, where we can easily test our quantum theory. As a matter of fact, as we show in appendix E, it is possible to easily generate reference results using the Mie theory. However, this methodology cannot be directly applied to arbitrarily shaped MNPs, since it exploits the analytical solution of the electromagnetic scattering problem of a sphere. In these other cases, more advanced methods to compute the radiative decay rate and the frequency shift of the plasmon oscillations have to be used. In general, this problem reduces to the much more complicated numerical computation of modes and resonances in the full-retarded regime. This is a huge topic and it has been largely discussed in the first chapter. On the other side, to compute the radiative decay rates and the frequency shifts with equations (2.64)-(2.65) and (2.77), only the use of a quasistatic modal basis is needed and, once that it has been determined as it is shown in appendix B, the computation of these quantities is straightforward. Now we want to show a couple of examples for the arbitrarily shaped case. We show both the predictions of equations (2.64)-(2.65) obtained within the rotating wave approximation and the ones of (2.77) computed beyond this approximation, from Hamiltonian (2.66). In figure 2.4 and 2.5 the cases of an oblate spheroid and of a prolate one are shown. The ratio between the major axis l and the minor one is takes equal to 3.

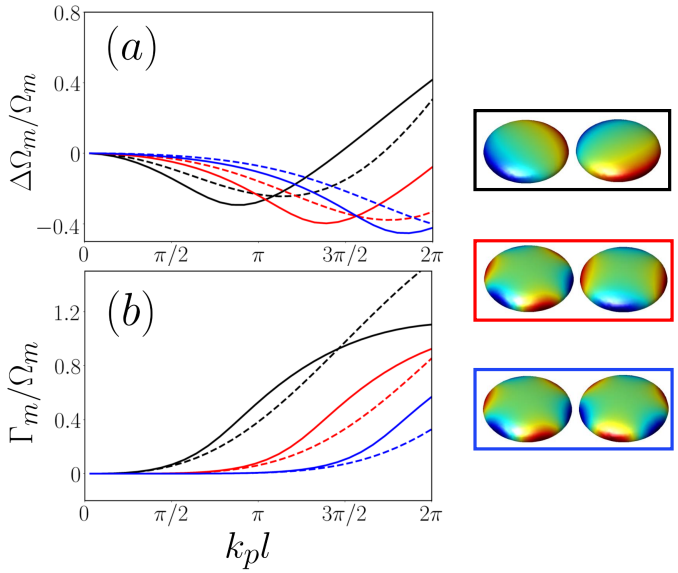

Figure 2.4: Frequency shift (a) and radiative decay rate (b) of the lowest energy plasmon modes of an oblate spheroid. The surface charge density of each mode is shown in a box whose color matches the one of the corresponding curves. The modes in the same box are degenerate. Comparison between the predictions of the RWA (dashed lines) of equations (2.64)-(2.65) and the results of (2.77) (solid lines), which are derived beyond the RWA from (2.66). l is the major semiaxis and it is taken three times bigger than the minor one.

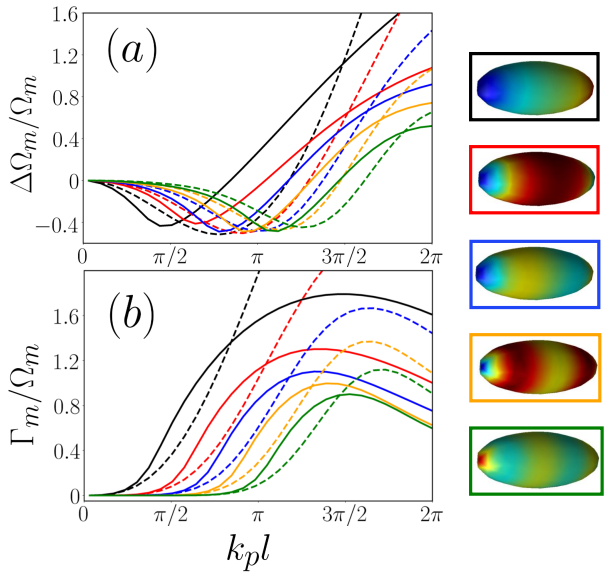

Figure 2.5: Frequency shift (a) and radiative decay rate (b) of the lowest energy plasmon modes of a prolate spheroid. The surface charge density of each mode is shown in a box whose color matches the one of the corresponding curves. The modes in the same box are degenerate. Comparison between the predictions of the RWA (dashed lines) of equations (2.64)-(2.65) and the results of (2.77) (solid lines), which are derived beyond the RWA from (2.66). l is the major semiaxis and it is taken three times bigger than the minor one.

2.6 Quantization in metal nanodimers

Another strong point of the quantum theory that we have developed in this thesis chapter is that its extension to the dimer case is straightforward[8]. As a matter of fact, only the QES modal expansion has to be adapted, while the way to describe the interaction with the radiative photons remains exactly the same. Thus, it does not change the procedure to compute the radiative decay rate and the frequency shift of the plasmon excitations and the formulas (2.64)-(2.65) and (2.77) do not formally vary. Indeed, once that we define a proper quasistatic modal expansion for the electron displacement field inside the dimer, the quantity $V^m_{\boldsymbol{q},s}$ will represent the coupling strength between the plasmon mode $\boldsymbol{U}_m$ and the plane wave of wave number $\boldsymbol{q}$ and polarization $\boldsymbol{e}_{\boldsymbol{q},s}$. Moreover, the QES dimer expansion is an easy extension of the one presented in appendix B for the single nanoparticle. As a matter of fact, the auxiliary eigenvalue problem (2.100) is formally written in the same way of the single particle case, with the only difference that the integration in (2.99) is done on the surface of the two objects. In figure 2.6 we show the radiative decay rate and the frequency shift of the lowest energy plasmon modes in the case of a dimer constituted of two identical metal nanosphere. In figure 2.7 we present the same data for a bow-tie antenna constituted of two equilateral nanoprisms.

[8] We consider the meaningful case of two coupled nanoparticles but everything is perfectly valid for a generic array.

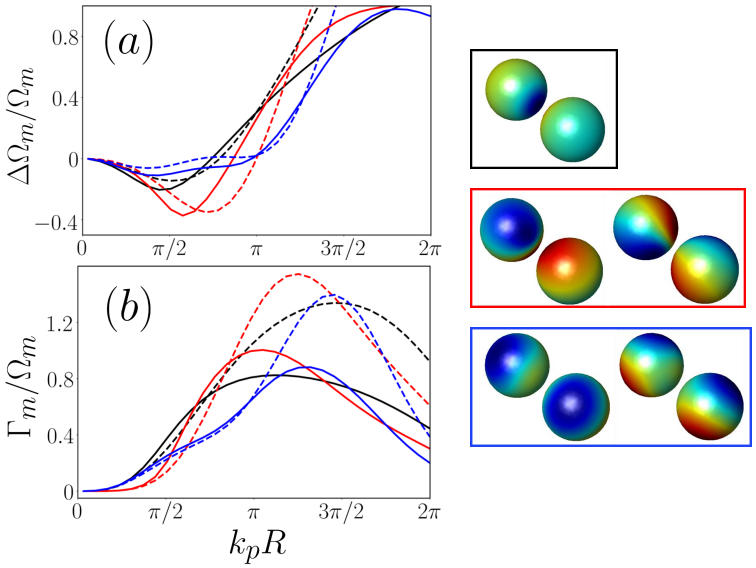

Figure 2.6: Frequency shift (a) and radiative decay rate (b) of the lowest energy plasmon modes in the case of a dimer made of two identical spheres of radius R. The distance between the two spheres is equal to $R/2$. The surface charge density of each mode is shown in a box whose color matches the one of the corresponding curves. The modes in the same box are degenerate. Comparison between the predictions of the RWA (dashed lines) of equations (2.64)-(2.65) and the results of (2.77) (solid lines), which are derived beyond the RWA from (2.66).

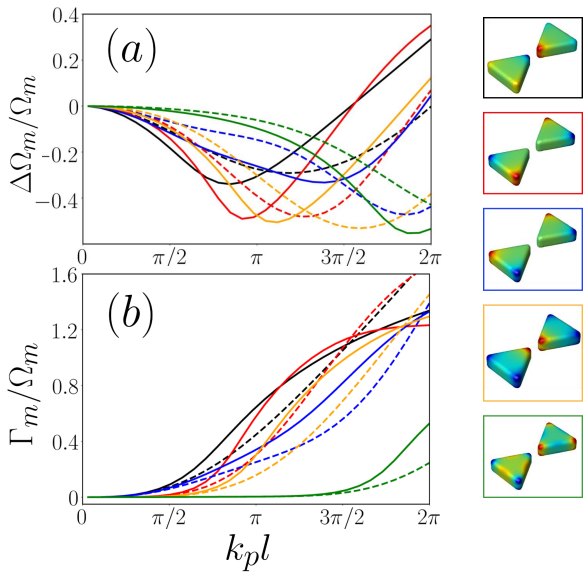

Figure 2.7: Frequency shift (a) and radiative decay rate (b) of the lowest energy plasmon modes in the case of a bow-tie antenna for two different gaps. The bow-tie antenna is constituted by two equilateral nanoprims of edge $2l$, of height $l/2$, and rounded corners of radius of curvature $0.15\ l$. The distance between the two nanoprisms is equal to l. The surface charge density of each mode is shown in a box whose color matches the one of the corresponding curves. Comparison between the predictions of the RWA (dashed lines) of equations (2.64)-(2.65) and the results of (2.77) (solid lines), which are derived beyond the RWA from (2.66).

2.7 Conclusions

In this thesis chapter we have developed a quantization scheme able to describe the quantum dynamics of the plasmon excitations in arbitrarily shaped metal nanoparticles and dimers, in the full-retarded regime. In the QES limit, the electron fluid motion is decomposed into a set of infinite lifetime oscillating modes, whose energies are quantized. Beyond the QES limit, the retardation is described, at the quantum scale, as the exchange of energy between these plasmon excitations and the photons. Because of these interactions, the plasmon energies shift and the plasmon excitations acquire a radiative damping and decay in time.

Our treatment represents an add-on to the existent literature because of the following considerations. Arbitrarily shaped nanoparticles and dimers are rarely treated, from the quantum point of view, out of the QES regime. Most of the retarded analyses of the quantum plasmons that have been proposed over time are either phenomenological or, if rigorous, they limit their attention to the analytic sphere case. The few existing studies of plasmon+photon quantization in the presence of arbitrarily shaped particles are in the frequency domain (e.g. [72]). Our approach instead starts from a time-domain description, and so it could also constitute the starting point to develop efficient methods to study the transient response of metal nanostructures to pulsed classical or quantum light. Moreover, we not only give an appropriate quantum description of more complex cases of great interest for the applications, but we also carry on a critic investigation on the derived plasmon-photon Hamiltonian, showing two key results. First, the widely diffused rotating wave approximation, even if it agrees qualitatively, its quantitative predictions lack in accuracy. Second, we discuss an approximate Hamiltonian able to accurately describe the quantum dynamics of the plasmon excitations in the great majority of the cases of practical interest. Working with this approximate Hamiltonian, we have derived some closed formulas to compute the radiative decay rate and the frequency shift of the plasmon excitations in the full-retarded regime. These formulas appear to be very efficient because they return us these full-retarded quantities, starting from a QES modal decomposition. Thus, they do not need electrodynamical modal expansions and they are not perturbative.

Appendix A: Euler-Lagrange equations

In this section, we briefly comment why the Lagrangian (2.18)-(2.22) properly describes the linear response of a metal nanoparticle assuming the lattice to be a positive charge uniform background and neglecting the pressure effects on the motion of the electrons. Let's write the standard light-matter Lagrangian for an electron fluid subject to a nonholonomic constraint, i.e. being confined inside a fixed region $\mathcal{B}$ [78]:

$$\begin{aligned}
\mathcal{L} &= \mathcal{L}_A + \mathcal{L}_B + \mathcal{L}_C && (2.78)\\
\mathcal{L}_A &= \int_{\mathbb{R}^3} \frac{1}{2} m_e n_0 \left(\partial_t \boldsymbol{\zeta}\right)^2 d^3\boldsymbol{r} && (2.79)\\
\mathcal{L}_B &= \int_{\mathbb{R}^3} \Big[\frac{\epsilon_0}{2}(\partial_t \boldsymbol{A})^2 + \frac{\epsilon_0}{2}(\nabla\phi)^2 + \epsilon_0 \partial_t \boldsymbol{A}\cdot\nabla\phi \\
&\qquad -\frac{1}{2\mu_0}\left(\boldsymbol{\nabla}\times\boldsymbol{A}\right)^2\Big] d^3\boldsymbol{r} && (2.80)\\
\mathcal{L}_C &= -en_0\int_\Omega \boldsymbol{A}\cdot\partial_t\boldsymbol{\zeta} d^3\boldsymbol{r} + en_0\int_{\mathcal{S}}\phi\zeta_n d^2\boldsymbol{r}, && (2.81)
\end{aligned}$$

where $\boldsymbol{A}$ and ϕ are the vector and the scalar potential defined such that $\boldsymbol{B} = \nabla\times\boldsymbol{A}$ and $\boldsymbol{E} = -\partial_t\boldsymbol{A} - \nabla\phi$, and where we have fixed the Coulomb gauge, i.e. $\nabla\cdot\boldsymbol{A} = 0$.

Said $\delta\phi$ a perturbation of the scalar potential, we obtain:

$$\begin{aligned}
\mathcal{L}_B[\phi+\delta\phi] - \mathcal{L}_B[\phi] &= \epsilon_0\int_{\mathbb{R}^3}\nabla\phi\cdot\nabla\delta\phi d^3\boldsymbol{r}\\
&= \epsilon_0\int_{\mathcal{B}}\nabla\phi\cdot\nabla\delta\phi d^3\boldsymbol{r} + \epsilon_0\int_{\mathcal{B}_c}\nabla\phi\cdot\nabla\delta\phi d^3\boldsymbol{r}\\
&= \epsilon_0\int_{\mathcal{B}}\delta\phi\nabla^2\phi d^3\boldsymbol{r} + \epsilon_0\int_{\mathcal{B}_c}\delta\phi\nabla^2\phi d^3\boldsymbol{r}\\
&\quad + \int_{\mathcal{S}}\delta\phi\left[\partial_n\phi^{(\mathcal{B})} - \partial_n\phi^{(\mathcal{B}_c)}\right] d^2\boldsymbol{r}, && (2.82)
\end{aligned}$$

where we have split the integral over the all space $\mathbb{R}^3$ into an integral over $\mathcal{B}$ and an integral over its complement $\mathcal{B}_c = \mathbb{R}^3\backslash\mathcal{B}$. In equation (2.82), ∂_n is the normal outgoing (from $\mathcal{B}$ to $\mathcal{B}_c$) derivative over the surface $\mathcal{S}$, and the value of the field is taken in the region indicated by the apexes. From the Euler-Lagrange equation

$$\partial_t\left[\frac{\delta\mathcal{L}}{\delta\left(\partial_t\phi\right)}\right] = \frac{\delta\mathcal{L}}{\delta\phi}, \qquad (2.83)$$

we obtain:

$$\begin{aligned} \nabla^2\phi &= 0 \quad \text{in } \mathcal{B} && (2.84)\\ \nabla^2\phi &= 0 \quad \text{in } \mathcal{B}_c && (2.85)\\ -en_0\zeta_n &= \epsilon_0\left[\partial_n\phi^{(\mathcal{B})} - \partial_n\phi^{(\mathcal{B}_c)}\right] \quad \text{on } \mathcal{S}, && (2.86) \end{aligned}$$

if we take $\delta\phi$ with support $\mathcal{B}$, $\mathcal{B}_c$, and $\mathcal{S}$, respectively. Since we have fixed the Coulomb gauge, the normal component of the vector potential is continuous on the surface and, the same can be said for its time derivative. Thus, the (2.86) expresses the jump of the normal component of the electric field on the surface of the nanoparticle due to the surface charge.

The Euler-Lagrange equation

$$\partial_t\left[\frac{\delta\mathcal{L}}{\delta\left(\partial_t\boldsymbol{A}\right)}\right] = \frac{\delta\mathcal{L}}{\delta\boldsymbol{A}} \tag{2.87}$$

gives

$$\epsilon_0\partial_t^2\boldsymbol{A} + \epsilon_0\partial_t\nabla\phi = -\frac{1}{\mu_0}\nabla\times\nabla\times\boldsymbol{A} - en_0\partial_t\boldsymbol{\zeta}, \tag{2.88}$$

that is the Ampère-Maxwell equation, while from:

$$\partial_t\left[\frac{\delta\mathcal{L}}{\delta\left(\partial_t\boldsymbol{\zeta}\right)}\right] = \frac{\delta\mathcal{L}}{\delta\boldsymbol{\zeta}} \tag{2.89}$$

we derive

$$m_e n_0\partial_t^2\boldsymbol{\zeta} - en_0\partial_t\boldsymbol{A} = en_0\nabla\phi, \tag{2.90}$$

that is the linearized Euler equation describing the electron fluid dynamics inside the nanoparticle.

From the system (2.84)-(2.86), we have

$$\phi(\boldsymbol{r}) = -\frac{en_0}{4\pi\epsilon_0}\int_{\mathcal{S}}\frac{\zeta_n(\boldsymbol{r}')}{|\boldsymbol{r}-\boldsymbol{r}'|}d^2\boldsymbol{r}'. \tag{2.91}$$

Thus, on the motion, we get

$$\begin{aligned} \int_{\mathbb{R}^3}\frac{\epsilon_0}{2}\left(\nabla\phi\right)^2 d^3\boldsymbol{r} \quad &+ \quad en_0\int_{\mathcal{S}}\phi\zeta_n d^2\boldsymbol{r} = \frac{\epsilon_0}{2}\int_{\mathcal{S}}\phi(\boldsymbol{r})\left[\partial_n\phi^{(\mathcal{B})} - \partial_n\phi^{(\mathcal{B}_c)}\right]d^2\boldsymbol{r}\\ &+ \quad en_0\int_{\mathcal{S}}\phi\zeta_n d^2\boldsymbol{r} = \frac{en_0}{2}\int_{\mathcal{S}}\phi\zeta_n d^2\boldsymbol{r}, \end{aligned} \tag{2.92}$$

and so, observing that

$$\int_{\mathbb{R}^3}\nabla\phi\cdot\partial_t\boldsymbol{A} = \epsilon_0\int_{\mathcal{S}}\phi\left[\partial_t\boldsymbol{A}^{(\mathcal{B})} - \partial_t\boldsymbol{A}^{(\mathcal{B}_c)}\right]_n d^2\boldsymbol{r} = 0, \tag{2.93}$$

we can rewrite the Lagrangian (2.78)-(2.81) in the form (2.18)-(2.22).

Appendix B: Harmonic expansion

In this section, we first discuss the building of a basis of harmonic fields in an arbitrary shaped domain. We do that by adapting, to our framework, an argument of [14] and [25]. Second, we show how to derive the (2.8). Eventually, we provide the analytic case of the sphere.

A possible way to face the problem is to see the harmonic field $\boldsymbol{U}$ inside the MNP, as a truncation to $\mathcal{B}$ of the solution of the following extended problem:

$$\begin{aligned}
\nabla \cdot \boldsymbol{U}(\boldsymbol{r}) &= 0 \quad \text{in } \mathcal{B}, \mathcal{B}_c && (2.94)\\
\nabla \times \boldsymbol{U}(\boldsymbol{r}) &= 0 \quad \text{in } \mathcal{B}, \mathcal{B}_c && (2.95)\\
\left[\boldsymbol{U}^{(\mathcal{B}_c)}(\boldsymbol{r}) - \boldsymbol{U}^{(\mathcal{B})}(\boldsymbol{r})\right] \cdot \boldsymbol{n}(\boldsymbol{r}) &= u(\boldsymbol{r}) \quad \text{on } \mathcal{S} && (2.96)\\
\left[\boldsymbol{U}^{(\mathcal{B}_c)}(\boldsymbol{r}) - \boldsymbol{U}^{(\mathcal{B})}(\boldsymbol{r})\right] \times \boldsymbol{n} &= 0 \qquad \text{on } \mathcal{S}, && (2.97)
\end{aligned}$$

where $\boldsymbol{U}^{(\mathcal{B}_c)} = \boldsymbol{U}|_{\mathcal{B}_c}$, $\boldsymbol{U}^{(\mathcal{B})} = \boldsymbol{U}|_{\mathcal{B}}$, $\boldsymbol{n}$ is the outgoing normal versor on $\mathcal{S}$ and $u(\boldsymbol{r})$ is the jump of the normal component on the surface. As shown in [14], the following relations hold:

$$\boldsymbol{n} \cdot \boldsymbol{U}^{(\mathcal{B})}(\boldsymbol{r}) = -\frac{u(\boldsymbol{r})}{2} + \mathcal{F}\{u\}, \quad \boldsymbol{n} \cdot \boldsymbol{U}^{(\mathcal{B}_c)}(\boldsymbol{r}) = +\frac{u(\boldsymbol{r})}{2} + \mathcal{F}\{u\}, \quad (2.98)$$

where

$$\mathcal{F}\{u\} = \frac{1}{4\pi} \int_{\mathcal{S}} u(\boldsymbol{r}') \frac{(\boldsymbol{r}' - \boldsymbol{r}) \cdot \boldsymbol{n}(\boldsymbol{r})}{|\boldsymbol{r}' - \boldsymbol{r}|^3} d^2\boldsymbol{r}'. \quad (2.99)$$

Then, let's consider the eigenvalue problem:

$$\mathcal{F}\{u\} = \frac{1}{2\gamma} u, \quad (2.100)$$

and call U_m the field associated to the eigenfunction u_m and to the eigenvalue

γ_m. The following relations hold:

$$\boldsymbol{n} \cdot \boldsymbol{U}_m^{(\mathcal{B})}(\boldsymbol{r}) = \frac{1}{2}\left(\frac{1}{\gamma_m} - 1\right) u_m(\boldsymbol{r}) \quad \text{on } \mathcal{S}, \tag{2.101}$$

$$n \cdot \boldsymbol{U}_m^{(\mathcal{B}_c)}(\boldsymbol{r}) = \frac{1}{2}\left(\frac{1}{\gamma_m} + 1\right) u_m(\boldsymbol{r}) \quad \text{on } \mathcal{S}, \tag{2.102}$$

$$\int_{\mathcal{B}} \boldsymbol{U}_m^{(\mathcal{B})}(\boldsymbol{r}) \cdot \boldsymbol{U}_n^{(\mathcal{B})}(\boldsymbol{r}) d^3\boldsymbol{r} = \delta_{nm}\mathcal{V}_m, \tag{2.103}$$

$$\int_{\mathcal{B}_c} \boldsymbol{U}_m^{(\mathcal{B}_c)}(\boldsymbol{r}) \cdot \boldsymbol{U}_n^{(\mathcal{B}_c)}(\boldsymbol{r}) d^3\boldsymbol{r} = \delta_{nm}\frac{\gamma_m + 1}{\gamma_m - 1}\mathcal{V}_m, \tag{2.104}$$

$$\begin{aligned}\int_{\mathcal{S}}\int_{\mathcal{S}} \frac{u_n(\boldsymbol{r})u_m(\boldsymbol{r}')}{4\pi|\boldsymbol{r}-\boldsymbol{r}'|} d^2\boldsymbol{r} d^2\boldsymbol{r}' &= \int_{\mathbb{R}^3} \boldsymbol{U}_m(\boldsymbol{r}) \cdot \boldsymbol{U}_n(\boldsymbol{r}) d^3\boldsymbol{r} \\ &= \left(1 + \frac{\gamma_m + 1}{\gamma_m - 1}\right)\delta_{nm}\mathcal{V}_m.\end{aligned} \tag{2.105}$$

Eventually, the (2.8) is obtained by substituting $\boldsymbol{\zeta}(\boldsymbol{r}, t) = \sum_m q_m(t)\boldsymbol{U}_m(\boldsymbol{r})$ into the (2.6), and exploiting the relations (2.101)-(2.105). The plasmon frequencies are $\Omega_n = \omega_p\sqrt{\frac{1}{2}\left(1 - \frac{1}{\gamma_n}\right)}$.

Sphere case. In the case of a spherical MNP, said R its radius, the harmonic modes can be written as the opposite of the gradient of the following set of scalar fields $\{\phi_{lk}(\boldsymbol{r})\}$:

$$\begin{aligned}\phi_{lk}^{(\mathcal{B})}(r) &= A_{lk}\left(\frac{r}{R}\right)^l Y_l^k(\theta, \phi) \\ \phi_{lk}^{(\mathcal{B}_c)}(r) &= A_{lk}\left(\frac{R}{r}\right)^{l+1} Y_l^k(\theta, \phi),\end{aligned} \tag{2.106}$$

where $Y_l^k(\theta, \phi)$ are the spherical harmonics with $l = 1, 2, \ldots$ and $k = 0, \pm 1, \ldots, \pm l$, and A_{lk} are normalization constants that can be arbitrarily chosen. From the (2.96), we get that:

$$u_{lk}(\boldsymbol{r}) = \partial_r\phi^{(\mathcal{B})} - \partial_r\phi^{(\mathcal{B}_c)} = (2l + 1) R^{l-1} Y_l^k(\theta, \phi), \tag{2.107}$$

and then, exploiting the (2.101), we obtain the plasmon frequencies: $\Omega_{lk} = \omega_p\sqrt{\frac{l}{2l+1}}$. Let's observe that these frequencies do not depend on k, and so we have, for each l, $2l + 1$ degenerate modes, i.e. three dipoles, five quadrupoles, and so on. This is mirror of the spherical symmetry of the MNP.

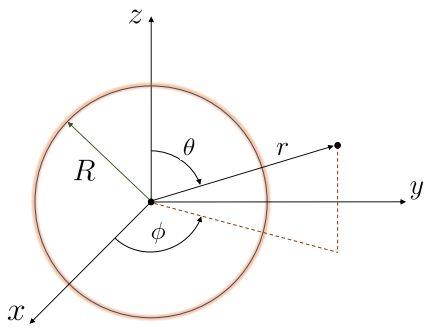

Figure 2.8: Nanosphere and spherical coordinates.

Appendix C: Field quantization

In this section, we briefly sketch the field theory formulation of the full-retarded regime, that does not explicit modal expansions. Starting from the Lagrangian (2.18)-(2.22), we define the conjugate fields $\boldsymbol{\chi}(\boldsymbol{r},t) = \frac{\delta\mathcal{L}}{\delta(\partial_t\boldsymbol{\zeta})}$ and $\boldsymbol{\Pi}(\boldsymbol{r},t) = \frac{\delta\mathcal{L}}{\delta(\partial_t\boldsymbol{A})}$. The Legendre transformation:

$$\begin{aligned}\mathcal{H}\left(\boldsymbol{\zeta},\boldsymbol{\chi},\boldsymbol{A},\boldsymbol{\Pi}\right) = \Bigg[\int_{\mathbb{R}^3}\boldsymbol{\chi}\cdot\left(\partial_t\boldsymbol{\zeta}\right)d^3\boldsymbol{r} + \int_{\mathbb{R}^3}\boldsymbol{\Pi}\cdot\left(\partial_t\boldsymbol{A}\right)d^3\boldsymbol{r} \\ -\mathcal{L}\left(\boldsymbol{\zeta},\partial_t\boldsymbol{\zeta},\boldsymbol{A},\partial_t\boldsymbol{A}\right)\Big]_{\boldsymbol{\zeta},\boldsymbol{\chi},\boldsymbol{A},\boldsymbol{\Pi}},\end{aligned} \tag{2.108}$$

brings to the following Hamiltonian:

$$\begin{aligned}\mathcal{H} = \int_{\mathbb{R}^3}\frac{1}{2m_e n_0}\left[\boldsymbol{\chi}+en_0\boldsymbol{A}\right]^2 d^3\boldsymbol{r} + \int_{\mathbb{R}^3}\Bigg[\frac{1}{2\epsilon_0}\boldsymbol{\Pi}^2 \\ +\frac{1}{2\mu_0}(\nabla\times\boldsymbol{A})^2\Bigg]d^3\boldsymbol{r} + \frac{(en_0)^2}{8\pi\epsilon_0}\int_{\mathcal{S}}\int_{\mathcal{S}}\frac{\zeta_n(\boldsymbol{r})\zeta_n(\boldsymbol{r}')}{|\boldsymbol{r}-\boldsymbol{r}'|}d^2\boldsymbol{r}d^2\boldsymbol{r}'.\end{aligned} \tag{2.109}$$

Eventually, we promote $\boldsymbol{\zeta}$, $\boldsymbol{\chi}$, $\boldsymbol{A}$, and $\boldsymbol{\Pi}$ to field of operators verifying the equal time commutation relation [78]:

$$\begin{aligned}\left[\hat{\boldsymbol{\zeta}}_i(\boldsymbol{r}), \hat{\boldsymbol{\chi}}_j(\boldsymbol{r}')\right] &= i\hbar\delta_{i,j}\delta(\boldsymbol{r}-\boldsymbol{r}') \\ \left[\hat{\boldsymbol{A}}_i(\boldsymbol{r}), \hat{\boldsymbol{\Pi}}_j(\boldsymbol{r}')\right] &= i\hbar\delta^{\perp}_{i,j}(\boldsymbol{r}-\boldsymbol{r}'),\end{aligned} \tag{2.110}$$

where the subscripts refer to the components of the fields and where $\delta^{\perp}$ is the transverse delta function:

$$\delta^{\perp}_{i,j}(\boldsymbol{r}) = \delta_{i,j}\delta(\boldsymbol{r}) + \frac{1}{4\pi}\partial^2_{i,j}\frac{1}{r}. \tag{2.111}$$

Appendix D: Derivation of the propagator's evolution

In this section, we show the steps to derive the system (2.67)-(2.68). Equation (2.52) is a subcase of it. First of all, applying the (2.50) to the plasmon propagator $g_m(t)$, we have:

$$\begin{aligned}\hbar z G_m(z) &= 1 + G_{\left[\hat{b}_m,\mathcal{H}\right]\hat{b}^\dagger_m}(z) = 1 + \hbar\Omega_m G_m(z) \qquad (2.112)\\ &+ \int_{\mathbb{R}_3}\frac{d\boldsymbol{q}^3}{(2\pi)^3}\sum_{s=1}^{2}\left[V^m_{\boldsymbol{q},s}G_{\hat{a}_{\boldsymbol{q},s}\hat{b}^\dagger_m}(z) - V^{m*}_{\boldsymbol{q},s}G_{\hat{a}^\dagger_{\boldsymbol{q},s}\hat{b}^\dagger_m}(z)\right]\\ \hbar z H_m(z) &= G_{\left[\hat{b}_m,\mathcal{H}\right]\hat{b}^\dagger_m}(z) = -\hbar\Omega_m H_m(z) \qquad (2.113)\\ &+ \int_{\mathbb{R}_3}\frac{d\boldsymbol{q}^3}{(2\pi)^3}\sum_{s=1}^{2}\left[V^m_{\boldsymbol{q},s}G_{\hat{a}_{\boldsymbol{q},s}\hat{b}^\dagger_m}(z) - V^{m*}_{\boldsymbol{q},s}G_{\hat{a}^\dagger_{\boldsymbol{q},s}\hat{b}^\dagger_m}(z)\right].\end{aligned}$$

Then, iterating the method, we obtain:

$$\begin{aligned}\hbar z G_{\hat{a}_{\boldsymbol{q},s}\hat{b}^\dagger_m} &= G_{\left[\hat{a}_{\boldsymbol{q},s},\mathcal{H}\right]\hat{b}^\dagger_m}(z)\\ &= \hbar\omega_q G_{\hat{a}_{\boldsymbol{q},s}\hat{b}^\dagger_m} + V^{m*}_{\boldsymbol{q},s}\left[G_m - H_m\right] \qquad (2.114)\\ \hbar z G_{\hat{a}^\dagger_{\boldsymbol{q},s}\hat{b}^\dagger_m} &= G_{\left[\hat{a}^\dagger_{\boldsymbol{q},s},\mathcal{H}\right]\hat{b}^\dagger_m}(z)\\ &= -\hbar\omega_q G_{\hat{a}^\dagger_{\boldsymbol{q},s}\hat{b}^\dagger_m} + V^{m}_{\boldsymbol{q},s}\left[G_m - H_m\right], \qquad (2.115)\end{aligned}$$

from where:

$$\begin{aligned}G_{\hat{a}_{\boldsymbol{q},s}\hat{b}^\dagger_m} &= \frac{V^{m*}_{\boldsymbol{q},s}}{\hbar z - \hbar\omega_q}\left[G_m - H_m\right] \qquad (2.116)\\ G_{\hat{a}^\dagger_{\boldsymbol{q},s}\hat{b}^\dagger_m} &= \frac{V^{m}_{\boldsymbol{q},s}}{\hbar z + \hbar\omega_q}\left[G_m - H_m\right]. \qquad (2.117)\end{aligned}$$

Appendix E: Classical radiative decay rates and frequency shifts

The reference radiative decay rate and the frequency shift of the plasmon oscillations in a spherical MNP can be derived within the framework of classical electrodynamics, adapting the treatment of the scattering by plane waves. In chapter 4 of [28], it is shown that, in order to solve the scattering problem of a sphere illuminated by a linearly polarized plane wave, we have to expand the incident plane wave, the internal field, and the external (in the book scattered) field in vector spherical harmonics. The coefficients of the expansions of the internal and of the external fields are obtained from the linear system that arises by imposing the continuity of the tangential components of the electric field and of the magnetic field. The vector spherical harmonics used in the expansions are divided in two classes: the E-waves and the H-waves. In particular, we are interested in the E-waves. As a matter of fact, for a nanosphere of permittivity $\epsilon(\omega) = 1 - \omega_p^2/\omega^2$, they correspond to the electromagnetic field radiated by the plasmon oscillations of the electron fluid that we are investigating. In the scattering problem, for each E-wave, it has to be solved a 2 by 2 linear system in the form $Ax = b$. A depends on the radius R of the sphere and on its material, while b depends on the incident plane wave.

This treatment can be used to derive the reference quantities we need. Indeed, for $b = 0$, the system admits solutions different from zero if $det(A) = 0$. For each $l = 1, 2, \ldots$ E-waves system, it corresponds to find the ω such that:

$$\frac{h_l^{(1)}(kR)}{\partial_r \left[r h_l^{(1)}(kR) \right]_{r=R}} = \epsilon(\omega) \frac{j_l^{(1)}\left(\sqrt{\epsilon(\omega)} kR \right)}{\partial_r \left[r j_l^{(1)}\left(\sqrt{\epsilon(\omega)} kr \right) \right]_{r=R}}, \tag{2.118}$$

where $j_l^{(1)}$ and $h_l^{(1)}$ are, respectively, the spherical Bessel and Hankel functions of first type, $k = \omega/c_0$, and c_0 is the speed of light. In the limit of $R \to 0$, we can expand the spherical functions in the following way:

$$j_l^{(1)}\left(\sqrt{\epsilon} kR \right) \approx \alpha_l \left(\sqrt{\epsilon} kR \right)^l, \quad h_l^{(1)}(kR) \approx \frac{\beta_l}{(kR)^l}, \tag{2.119}$$

where α_l and β_l are proper constants. We first get $\epsilon(\omega) = -(l+1)/l$ and then the QES plasmon frequencies that we have derived in appendix B: $\Omega_l = \omega_p \sqrt{\frac{l}{2l+1}}$. In the small particle limit, real frequencies Ω_l that verifies the (2.118) do exist. It means that the corresponding E-waves can oscillate without decaying and without the need of an external driving. When the dimension

of the nanoparticle increases, equations (2.118) admit complex $\Omega_l(R)$ as solutions. It means that the corresponding E-waves do decay in time. As reference results for the frequency shift we consider $\Delta\Omega_l(R) = Re\left[\Omega_l(R)\right] - \Omega_l$ and for the radiative decay rate $\Gamma_l = -Im\left[\Omega_l(R)\right]$.

Chapter 3

Nonlinearities in Rydberg-EIT

A gas of Rydberg atoms, in the electromagnetic induced transparency (EIT) setup, has proven in recent years to be a promising approach to realize a highly nonlinear optical medium, where optical pulses interact strongly with each other down to the single-photon level. Thanks to the Rydberg blockade phenomenon, a single photon is indeed able to saturate the atomic response of a considerably large portion of the medium, that appears opaque to a second incoming one. This behaviour was first experimentally proven by T. Peyronel and co-workers in 2012 [79], when they also showed how Rydberg-EIT atomic gases could be used as possible platforms to turn classical light into quantum one. In this work, the authors entirely focused on the continuous wave (CW) response of a Rydberg gas, of which they also gave a complete theoretical explanation. Recently, the C. Adams' lab explored the nonlinear optical properties in the pulsed regime. Interestingly, it was observed that the transient behavior could exhibit a lower anti-bunching signal than the CW one, often associated with a stronger nonlinearity. [80]. The goal of this chapter is to provide a clearer picture of the physical origin of this effect, with the end goal being of determining whether this effect actually reflects a stronger, "useful" nonlinearity.

The treatment is subdivided as follows. In a first introductory part (section 3.1), we briefly review the historical mechanism to generate nonlinearities, based upon the saturation of the atomic response of a medium. The difficulty of realizing single-photon-level nonlinearities is due to the nature of this atom mediated interaction, that is local in space and narrow in time. Then, the physics of the Rydberg atoms, and the ability to effectively realize a long-range photon-photon interaction, is introduced as a novel route to

realize the single-photon nonlinear regime. In a second introductory part (section 3.2), we treat the light-matter interaction, first discussing the absorbing behaviour of a 2-level ensemble of atoms, and then the transparent one of the 3-level EIT setup. Then, the third part (section 3.3) is slightly more technical and it is devoted to introduce the tools to model Rydberg-EIT: the historical Maxwell-Bloch (MB) approach and the newer spin model (SM). The former is a wave equation method where the atomic degrees of freedom are accounted in the Maxwell's equation as a polarization field. The latter traces out the electromagnetic field and solves the effective atomic spin dynamics that arises. Eventually, in the fourth and last part (section 3.4), we present an original discussion on the nonlinearities in Rydberg-EIT, both in the continuous wave regime and in the transient dynamics. We model test scenarios where it is possible to separate the double-excitation evolution from the single-excitation one. The theoretical treatment is endorsed by SM simulations on effective atomic chains.

3.1 Photon-Photon interaction and Rydberg atoms

[1]The intrinsic non-interacting nature of photons makes light a perfect vehicle to transfer data. But it is also the origin of big challenges for what concerns information processing. As a matter of fact, signal processing requires, by definition, interaction, and interaction between photons cannot be deterministically obtained through linear optics. Two photons propagating in linear media, such as vacuum or optical fibers, and manipulated by linear devices, such as beam splitters or waveplates, will never interact with each other.

This is why, a resolute scientific community has been making a huge effort in facing the big challenge to establish a deterministic interaction between photons through nonlinear optics. This is quite an ambitious goal if we give a look at the history of nonlinear optics. Indeed, the observation of nonlinear behaviors was possible only after the development of high power lasers, since most of the optical materials exhibits only linear properties at low power. As a matter of fact, an electric field comparable to the field of the nuclea is needed to modify the index of refraction of a material and to make the propagation power-dependent. Technological improvements over time have made it possible to observe nonlinear phenomena at lower and lower power levels and, «with the advent of the quantum computation, the goal of making this interaction relevant at the few photon scale became more pressing» [81].

[1]We will mostly follow the treatment of [81].

Due to the highly anharmonic energy level spacing associated with the electronic states of an atom, it can effectively be thought as a two-level system, which is only able to emit and absorb single photons of a given, near-resonant frequency at a time. In this sense, a single atom appears to be the most nonlinear object we can think of, where a single photon is, in principle, enough to saturate its optical response. Once saturated, the atom is unable to respond to a second photon; this simple observation made atomic media a preferred approach to realize optical nonlinearities at low powers.

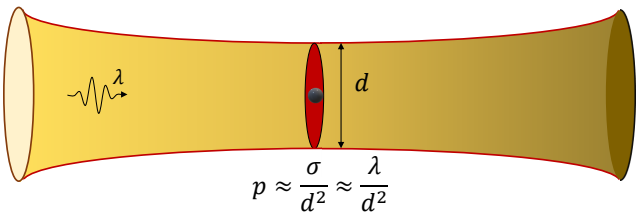

Figure 3.1: Schematic of the probability of interaction between a single atom and a single photon.

However, one can construct a simple argument to see that reaching the single-photon nonlinear regime is difficult. Let's first consider a single atom as a "medium". The probability p for the photon to be scattered by the medium, that in this case is the probability of interaction between the single atom and the single photon, depends on the atom scattering cross section σ and on the "width" d of the photon. The cross section σ is the effective size of the atom seen by the photon and it can be thought, in a more pictorial fashion, as the shadow of the atom in the light. It depends on the wavelength of the incoming photon and has a maximum at the transition wavelength λ, where $\sigma \approx \lambda^2$.

Thus, if we illuminate an atom with a highly focused light beam of diameter d at the transition frequency, we get $p \approx \lambda^2/d^2$ (see figure 3.1). In free space, because of diffraction limit, we always have $d > \lambda$, and this implies that, unless we elaborate something more, real life conditions will give us $p \ll 1$[2]. In order to make p approach 1, we can think of increasing the number of atoms N. Taking $N \approx 1/p$ assures that a single photon travelling through the medium will be absorbed by an atom. Now, if we let two photons propagate, even if we know that they will be both absorbed by the medium, we will not measure any nonlinear effect. Indeed, to measure nonlinearity, they should both approach the *same atom* at the *same time*, or in an interval of time dictated by the lifetime of the excited state. This event has almost the same probability of the single atom case. Thus, in order to saturate the atomic response of the medium, a large number of photons $n \approx N \approx 1/p$ must be used, but in this way we leave the few-photon scale. These space-time constraints to detect nonlinearity are central, as we will explore later, to understand the huge change that Rydberg physics brought to this research field. Indeed, Rydberg atoms will provide us long-range interactions at long time scales.

3.1.1 Rydberg atoms

[3]When an atom is excited to a large principal quantum number state, the corresponding electron is weakly bounded to the ionic core and exhibits a high sensitivity to the external stimuli. As a consequence, it shows features that are very different from the ones of the first excited states. In particular, it exhibits high polarizability, long lifetime, and strong nonlinearities due to the blockade mechanism. The general expression "Rydberg atoms" (RAs) refers to atoms in these quantum states. The energy levels of a generic Rydberg atom are well expressed by the Rydberg formula $E_n = -R/n^{*2}$. Here, R is the Rydberg constant of the atom and n^* is an experimentally measured effective principal quantum number that takes into account the modification of the Coulomb potential due to the presence of the electrons in the core.

The fundamental property of the Rydberg atoms is the huge dimension, indeed, the radius of a RA grows with the principal quantum number and, for n greater than 100, it gets in the order of a micron, 10^4 times bigger than a

[2]For $p \approx 1$, a single photon can undergo a strong attenuation, a reflection or a phase shift because of a single atom. For example, p can be increased by using advanced technique of light focusing [82, 83], sub-wavelength confinement of photons in the form of surface plasmons [57, 60], or cooling and trapping the atom inside an optical cavity [84].

[3]We will mostly follow the treatment of [85] and [81], with some insights from [86] and [87].

ground-state atom. Formally, it can be computed by averaging the module of the position operator of the excited electron over the high n eigenstate: $\langle n|\hat{r}|n\rangle \propto n^2$. As a consequence, the radiative lifetime also increases with n^2, and reaches the remarkable values of hundreds of microseconds already for $n \sim 60$, while the timescale of the first excited states is in the order of tens of nanosecond.

Long lifetime

To understand why a big radius implies a long lifetime in the case of RAs, let's remember that the probability for a transition to occur between two states, $|n_1\rangle$ and $|n_2\rangle$, depends on the corresponding matrix dipole element, namely $\langle n_1|e\hat{r}|n_2\rangle = \int \psi^*_{n_1}(r)e\hat{r}\psi_{n_2}(r)$, and this is true both in the absorption and in the emission process. Since the large Rydberg state barely overlaps with the small ground state, the coupling between these two transitions is very weak. It explains, on one side, why the excitation of the RAs is such a delicate process that has required almost one hundred years from their discovery to be mastered, and, on the other side, it tells us that when an electron is excited to a high n state, it weakly couples to the ground state and, so, this direct transition is unfortunate. Of course, one could observe that, since the others high n states overlap much with the excited Rydberg we are considering, these transitions are favorable and a ladder decay could easily take place. Why, in fact, this ladder decay doesn't happen depends on the number of available vacuum modes in this frequency range. Indeed, an excited electron decays to a lower level through the coupling with the vacuum modes, since a photon at the transition frequency has to be emitted. The density of vacuum modes is not uniform all over the electromagnetic spectrum and, as the wavelength increases, they become fewer and fewer[4]. Typically, the transitions from high n states to the ground could be either in the visible, like the one from the first excited states, or in the ultraviolet, while the ones between two close Rydberg levels are at microwaves or at terahertz and, in these ranges, there are not so many vacuum modes available to support spontaneous emission (see figure 3.2). Taking into account all the possible decay paths from the initial Rydberg state, it can be proved that the lifetime of these states scales as n^2 [85].

This really very long lifetime feature constitutes a first ingredient for the photon-photon interaction. To understand the genesis of the second ingredient,

[4]By quantizing the electromagnetic field in a periodic boundary condition cube, we can derive the following scaling for the number of vacuum modes per unit volume with a wavelength between λ and $\lambda + d\lambda$: $D(\lambda)d\lambda \propto d\lambda/\lambda^4$.

the long-range blockade, we first need to investigate how two Rydberg atoms interact.

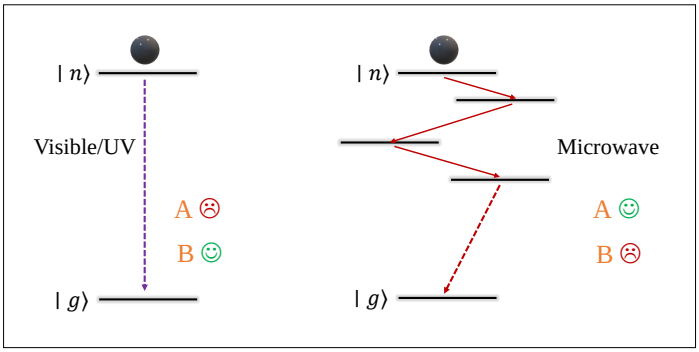

Figure 3.2: Sketch of the two possible decay schemes from a Rydberg level to the ground state. A and B refers to the amplitude of the matrix dipole elements associated to the transitions and to the density of available vacuum modes, respectively.

Dipole-dipole and van der Waals interactions

In order to characterize the interaction between Rydberg atoms, let's first investigate, from the microscopic point of view, how quantum dipoles, in general, talk to each other. We assume two identical atoms at distance R, we name $|nS\rangle$ and $|n_1P\rangle$, with $n > n_1$, the 2 levels involved in the interaction process, and we start from an initial condition where the two atoms are in a different state (see figure 3.3(a)). The QD in $|nS\rangle$, decaying to $|n_1P\rangle$, emits a photon at the transition frequency. This photon propagates toward the second QD that, absorbing it, experiences a transition from $|n_1P\rangle$ to $|nS\rangle$[5]. The photon propagation is described by the dyadic Green's function that, for a transition

[5]Here, we explicit the angular momentum conservation. Since a photon carries an angular momentum of $\hbar$, the transitions must be from different angular momentum levels, e.g. P and S.

wavelength much bigger than the distance between the two QDs, scales as $1/R^3$. This leads to the electrostatic dipole-dipole interaction potential and, whether we can use this limit or not, depends on the transition we are considering. To get an idea, when we consider a real cold atom experiment, the average inter-atomic distance is in the order of the optical wavelength we are working at, or some fractions of it (so from tens to hundreds of nm). Thus, the propagation must be taken into account for transition between first excited states or from them to the ground state, since they are in the near-infrared or in the visible. On the contrary, when we focus on the transition between Rydberg states (where the emitted wavelength is for example in the order of 1 mm for $n \sim 60$) the propagation effects can be completely ignored[6]. This interaction needs a spontaneous emission from $|nS\rangle$ to $|n_1P\rangle$ and the opposite absorption to take place. How likely these two processes are to occur is given by the corresponding matrix dipole element $\langle nP|e\hat{r}|n_1S\rangle$. In the case of $n_1 \sim n$, the dipole matrix element scales as n^2 and so, taking into account also the spatial dependence, this dipole-dipole interaction scales as n^4/R^3.

But this is not the whole story. Indeed, as the principal quantum number increases, the energy levels get closer and closer, and thus we can imagine interactions that involve other levels. Let's, for example, start from an initial condition where both the atoms are in the $|nS\rangle$ state. The above discussed first order process[7] cannot directly take place. Indeed, when the first atom decays from $|nS\rangle$ to $|n_1P\rangle$, the second should go from $|nS\rangle$ to a certain $|n_2P\rangle$ (with $n_2 > n$), whose energy difference with $|nS\rangle$ must be exactly the same as $|nS\rangle$ with $|n_1P\rangle$, in order to conserve the energy. But, due to the complex structure of the atomic energies, it is uncommon to find two equally energy spaced transitions $n_1 \longleftrightarrow n \longleftrightarrow n_2$.

A second order process, where the state $|n_1P, n_2P\rangle$ is only virtually occupied at a very short time scale, and the photon is immediately exchanged back, is instead possible (see figure 3.3(b)). Thanks to the time-energy indetermination principle, the energy defect Δ_E between the quantum states $|n_1P, n_2P\rangle$ and $|nS, nS\rangle$, at short time scale, is not forbidden, and this process doesn't violate the energy conservation. It is worth noting that the limit of very short time scale, and thus the consequent indetermination of the energy, is well posed in the study of this interaction, since the emitted microwave wavelengths of the transitions between Rydberg levels are much bigger than the distance between

[6]This is why the interaction between Rydberg atoms is said to be mediated by virtual photons.

[7]We say "first order" because it involves a single photon propagation. A process involving two propagations will be a second order process.

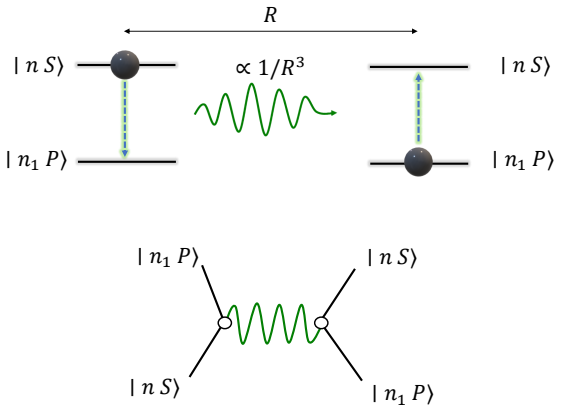

(a) Sketch of the dipole-dipole interaction.

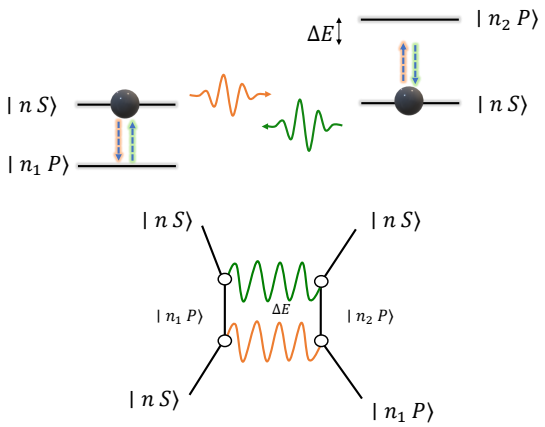

(b) Sketch of the van der Waals interaction.

Figure 3.3: Schematic representations of the interactions between Rydberg atoms, with the corresponding Feynman diagrams.

the interacting atoms, and thus the propagation time is close to zero. We refer to this second order process as van der Waals interaction and its strength can be formally computed via second order perturbation theory, it results to

scale as $n^8/\Delta_E R^6$. We can easily guess that n^8 comes from the fact the 4 processes (whose dipole matrix elements scale as n^2) are required, and that $1/R^6$ depends on the double Green's function propagation. Since the energy spacing Δ_E between two energy levels scales as $1/n^3$, the final scaling for this interaction is n^{11}/R^6. But it is worth pointing out that Δ_E can be controlled by external static fields, and this makes the strength of the Rydberg interaction tunable in the experiments.

Summarizing, as the dipole-dipole interaction, the van der Waals one depends on the distance between the atoms but, in contrast to that, it doesn't ask the atoms to change their state while interacting. Even if both these interactions are present at any atomic level, they become an inexhaustible resource for concrete applications when exploited in the RA case, and this is a direct consequence of the n-scaling laws of the matrix dipole element and of the energy spacing between the levels.

The Rydberg blockade

Now that we have seen how the interactions work in the RA framework, to better visualize their huge potential in the world of applications, we consider the following scenario. Let's imagine to have two atoms at distance R from each other (see figure 3.4), one of the two in a Rydberg state $|r\rangle$ and the other one in the ground state $|g\rangle$. The attempt to excite also the second atom to the $|r\rangle$ state, with a laser properly tuned on the transition frequency, has different outcomes depending on the value of R. If R is big enough, the second atom gets excited as if it were alone but, as R becomes smaller and smaller, its Rydberg energy starts to shift by the effect of the interaction potential with the already populated Rydberg level. We clearly understand that there will be a critical distance, which we call Rydberg radius R_b, at which this transition will be completely decoupled from the laser beam and, from there on, the second atom cannot be excited to the Rydberg state, as long as we do not detune the laser[8]. This is the so-called Rydberg blockade. Given a cloud of

[8]From atom physics we know that the density of states corresponding to a finite lifetime τ excitation is centred at the excitation energy but it is not a delta function. It has a width given by the decay rate of the atom $\Gamma = 1/\tau$. Formally, it can be seen in the emitted light, that is not purely monochromatic, but its spectral lineshape function $g(\omega)$ is a Lorentzian centred at the transition angular frequency and of *full width at half maximum* (FWHM) equal to $\Delta\omega = 1/\tau$ [88]. We can define the Rydberg radius as the distance R_b where the interaction potential is equal to Γ. Here we are referring to the natural broadening of $g(\omega)$, i.e. the one due to the radiation. There are other broadening mechanisms: the collisional broadening (due to the collisions between the atoms) and the Doppler broadening (due to the motion of the atoms) for

atoms in the ground state, shined by a laser tuned at a Rydberg transition, once that an atom is excited to a Rydberg level, the interaction potential will shift all the Rydberg levels of the surrounding atoms within the Rydberg sphere (the sphere of R_b radius) decoupling them from the laser and forcing them to persist in the ground state[9]. The blockade region, in the end, behaves as a "superatom" whose cross section is enhanced, with respect to the single atom one, by a factor equal to the number of atoms within the blockade sphere.

In section 3.1, we have learned the physical genesis of the nonlinearity at the few-photon level, i.e. the saturation of the atomic response, and we have identified the origin of the big challenges in achieving that, i.e. this nonlinearity is local in space (two photons must approach the same atom) and narrow in time (the excited states decay in tens of nanoseconds, and the second photon must arrive within this interval). Now we are ready to appreciate the big change that Rydberg atoms represented for atom physics: they created a nonlocal interaction in space, thanks to the blockade phenomenon[10], at the timescale of microseconds. A single photon approaching a single atom at a certain time is enough to saturate the optical response of the full portion of the medium within the blockade sphere for a considerable time. This nonlinearity at the two-photon level, provided by RAs, is finding many interesting applications in all the branches of quantum optics[11]. As anticipated at the beginning of the chapter, in section 3.4, we will describe how this nonlinear interaction in the EIT setup represents an efficient platform to turn classical light into quantum light.

example.

[9] As we will see later, the situation is slightly different, because the photon state turns into a collective Rydberg excitation rather than a single Rydberg atom but, to develop some first intuitions on the system, these simplified pictures are useful.

[10] R_b is in the order of microns (10^4 times bigger than an excited state atom).

[11] For example, in information theory it allows the building of controlled two photons quantum gates (such as controlled phase gates, i.e. CZ gates) [89, 90]. It is also possible to use this interaction to build deterministic single photon sources [91]. Moreover, thanks to the tunability of the interaction strength, there is room for RAs also in the world of quantum simulator [92], and, thanks to their high sensitivity to the external fields, of course in the world of sensors [93].

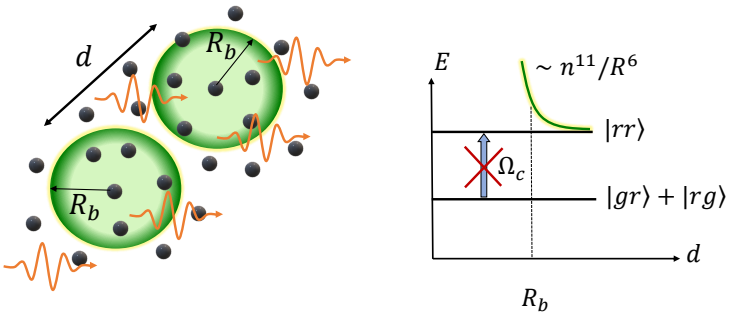

Figure 3.4: Schematic representation of the Rybderg blockade and of the energy shift due to the Rydberg interaction.

3.2 Light-matter interaction in atomic ensembles

In this section, we qualitatively describe how light interacts with an ensemble of atoms. In particular, we focus on 2-level and 3-level media. The formal derivation of the results is performed in section 3.3.1 by using a Maxwell-Bloch approach.

3.2.1 2-level medium

An ensemble of atoms, be it a cloud or a lattice, shined by a probe laser tuned at a particular frequency transition, acts as a 2-level medium, that is to say, from the modelling point of view, an ensemble of quantum dipoles. From now on, the two levels will be the ground state $|g\rangle$ and a first excited state $|e\rangle$. In this process, a portion of light is reflected back to the laser, another portion is transmitted on the other side of the medium and measured by a detector, and the remaining power is scattered in other directions noncollectable by the detector, and so it represents the losses of the system (see figure 3.5(a)). From the microscopic point of view, the atoms, initially in $|g\rangle$, absorbing the incoming photons, experience a transition to $|e\rangle$, and then decay back to $|g\rangle$ re-emitting a

photon at the same frequency either in the detection mode or in 4π (see section 3.3.1). This is why, many times, we refer to the losses of the system as the power absorbed by the atoms, i.e. the light first absorbed by the atoms and then re-scattered away. Indicating with R, T, and L the reflection, transmission and absorption intensity coefficients respectively (i.e. the ratio between the reflected, transmitted or absorbed intensity and the input one), the following relation holds: $R + T + L = 1$ (see figure 3.5(b)). Thus, R, T, and L can be interpreted as the probability for a photon travelling through the medium to be reflected back, transmitted or scattered away.

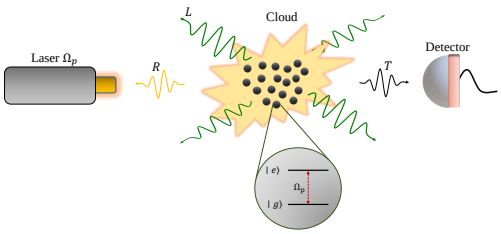

(a) Sketch of the scattering by an atomic 2-level cloud.

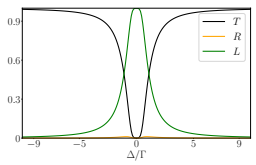

(b) Transmission, reflection and losses of a 2-level ensemble of $OD = 8$.

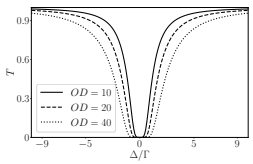

(c) Transmission for different values of the optical depth.

Figure 3.5: 2-level system analysis. The simulations are performed using the effective chain model that will be introduced in section 3.3.2. It is assumed $\Gamma_r = 0.5$.

An excited atom in free space, due to the interaction with the vacuum modes, after an average lifetime τ, spontaneously decays back to the ground state emitting a photon in the dipole mode. We characterize this process with a single number, the total (radiative) decay rate of the excited state: $\Gamma = 1/\tau$. When the atom is shined by the laser, the situation changes and a single number

is not enough to describe the dynamics properly. The isotropy of the free space is broken and, since the laser mode only partially overlaps with the dipole one, we have to distinguish between the probability of decaying into the detection mode and the probability of decaying into the other modes. Thus, we split the total decay rate into two contributes, Γ_1 and Γ' respectively, and we write $\Gamma = \Gamma_1 + \Gamma'$. The subscript 1, used for the decay rate inside the detection mode, underlines that we are implicitly forcing a directionality into the system and, in the case of some experiments, it allows us to build an equivalent 1D system to study it, e.g. an atomic chain. In free space $\Gamma_1/\Gamma' \ll 1$ (i.e. $\Gamma' \simeq \Gamma$), but the value of Γ_1 can be changed by a proper design of the environment surrounding the atoms.

Let's name ω_{eg} the transition frequency from $|g\rangle$ to $|e\rangle$, ω_p the frequency of the probe laser, and $\Delta = \omega_p - \omega_{eg}$ the detuning of the laser. According to Δ, the medium responds to light in different ways. In the far-detuned limit, the photons can cross the ensemble without noticing the atoms and, so, the medium appears transparent to light. On the contrary, at the transition frequency, the probability of interaction is maximum and, as we will prove in section 3.3.1, it corresponds to an absorbing behaviour (see figure 3.5(b)). In particular, for $\Delta = 0$ we measure a minimum in the transmission $T \ll 1$, from where we can define the optical depth (OD) of the ensemble as $OD = -\log(T)$. The optical depth represents the key figure of merit to describe the linear properties of a 2-level medium and it can be successfully theoretically modelled. The expression $T|_{\Delta=0} = e^{-OD}$ is usually called Beer's law and the amplitude of the interval around $\Delta = 0$ where the medium is absorbing grows with OD (as shown in figure 3.5(c)[12]).

Before getting into the formal description of section 3.3, to have an idea on how to model OD, let's consider a N-atom chain in the simplified hypothesis of neglecting multiple scattering, which in the chain case means neglecting reflections (see figure 3.6). Let's consider a continuous wave scenario, weak driving amplitude[13], and let's indicate with E_{n-1} the amplitude of the electric field approaching atom number n from left ($E_0 = E_{in}$, $E_N = E_{out}$). Without reflections, the electric field shining the n-th atom only depends on the portion

[12] From the experimental point of view, the value of a very high OD is obtained by fitting the tails of the transmission plot at large detunings, and not by measuring the transmission at $\Delta = 0$, that approaches zero very fast as OD increases.

[13] As it will be formally clarified later, the intensities, as all the observables depending only on single photon detections, are fully determined by the dynamics in the single-excitation subspace. The dynamics restricted to this subspace is always linear, since the atomic response cannot be saturated by a single photon.

of the transmitted field by the $(n-1)$-th one, that is given by the ratio between Γ_1 and Γ: $E_n = \left(1 - \frac{\Gamma_1}{\Gamma}\right) E_{n-1} = tE_{n-1}$. The transmission coefficient is the ratio between the output and the input intensity $T = \frac{I_{out}}{I_{in}} = \frac{E_{out}^2}{E_{in}^2} = \left(\frac{E_N}{E_0}\right)^2 = t^{2N} = \left(1 - \frac{\Gamma_1}{\Gamma}\right)^{2N} \simeq e^{-OD}$, where $OD = 2N\Gamma_1/\Gamma' \simeq 2N\Gamma_1/\Gamma$, and where the last approximate equality holds since $\Gamma_1/\Gamma \ll 1$, $\Gamma \simeq \Gamma'$[14].

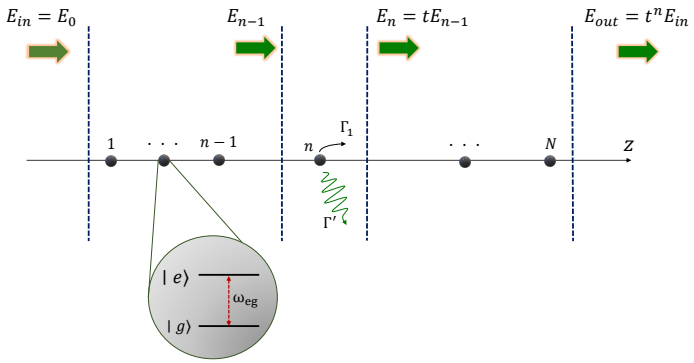

Figure 3.6: Sketch of the transmission through an atomic chain with no reflections.

Using the Maxwell-Bloch approach of section 3.3.1 we will show that the optical depth can also take the following form: $OD \propto NIm[\chi]$, where χ is the susceptibility of the single atom. This expression means that each atom is acting independently of the others. Neglecting multiple scattering and treating the atoms as if they were independent are two faces of the same assumption; the former formulated in terms of absorption/emission of photons, the latter in terms of wave interference. Depending on the problem, it could be useful to look at it in one of the two ways. As we will see later, these assumptions, when well posed, can help us in tackling the complicate problem of solving the light propagation in a 2-level medium. That's the case, for example, of a dilute gas of atoms, where the multiple scatterings are rare and the interferences are averaged out by the motion of the atoms.

[14] A formal and complete description can be found in [94]. We have already mentioned that it is possible to design situations where $\Gamma_1/\Gamma' \gg 1$ [60, 95]; in this case the QD would act as a mirror [96].

3.2.2 3-level medium: electromagnetic induced transparency

A transparency window can be opened in the transmission spectrum by coupling the excited state level $|e\rangle$ to a third more stable one $|s\rangle$, by shining the system with a second laser, namely the control laser, tuned at the frequency transition $\omega_{se} = \omega_s - \omega_e$. Let's say Ω_c and Ω_p the Rabi frequencies of the control field and of the probe field, respectively (see figure 3.7(a)). In the CW regime, a perfect interference phenomenon caused by the two lasers takes place at $\Delta = 0$, and it is such that no atomic population goes to $|e\rangle$, but only $|s\rangle$ is populated. Thus, if as $|s\rangle$ we choose a state whose lifetime is much longer than the time needed by the light to cross the medium, the light propagates through the ensemble without getting scattered away (see transmission, reflection and losses in figure 3.7(b)). The two fields play two profound different roles: Ω_p, being coupled to the ground, excites the atoms and determines the number of excitations within the medium; Ω_c has no influence on the number of excitations but, redistributing the population between $|e\rangle$ and $|s\rangle$, controls the dynamics.

Let's consider a single atom driven by Ω_p and Ω_c. Its quantum state takes the form $|\psi\rangle = c_g|g\rangle + c_e|e\rangle + c_s|s\rangle$, and the complex amplitudes evolve in the following way [97]:

$$\dot{c}_g = i\Omega_p c_e \tag{3.1}$$

$$\dot{c}_e = -\frac{\Gamma}{2}c_e + i\Omega_p c_g + i\Omega_c c_s \tag{3.2}$$

$$\dot{c}_s = i\Omega_c c_e. \tag{3.3}$$

In the steady state (CW), they do not vary, i.e. $\dot{c}_i = 0$, and so it follows that $c_e = 0$ and $c_s = -\frac{\Omega_p}{\Omega_c}c_g$. This interesting 3-level system phenomenon is called electromagnetic induced transparency[15]. As a consequence, a transparency window gets opened in the transmission diagram, compared to the 2-level case. We refer to its width as EIT bandwidth Δ_{EIT} (see figure 3.7). Let's try now to

[15]It is worth mentioning that the induced transparency is, in truth, a general phenomenon that appears every time that two harmonic oscillators are coupled. Let's for example consider two pendula, E and S, coupled by a spring C. Let's assume that E has some internal frictions that make it lossy, while S is lossless. If an external force P drives E in an oscillating fashion, it can be shown that there exists a frequency of transparency, i.e. a frequency at which all the energy goes directly to S, while E doesn't move at all. In this case, the full system appears to be lossless. From Classical Mechanics, we know that this system has two natural modes of oscillation: the two pendula oscillating in phase (ω_1) or in opposition of phase (ω_2). We can understand that, if P drives E at ω_2 it is possible to zero the total force acting on E. As a consequence, E doesn't move (it is transparent) and the oscillation is directly transferred to S.

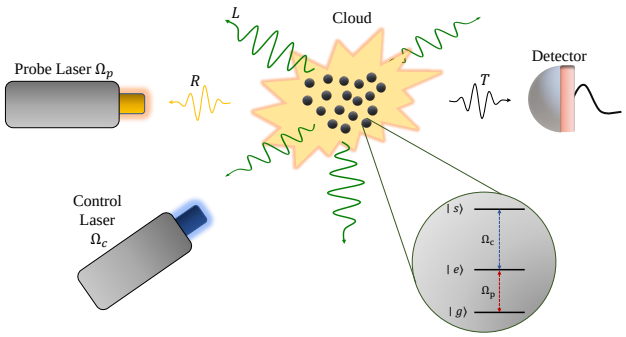

(a) Sketch of the scattering by an atomic 3-level cloud.

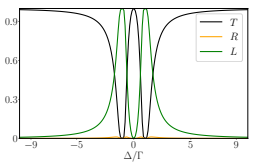

(b) Transmission, reflection and losses of a 3-level ensemble of $OD = 8$.

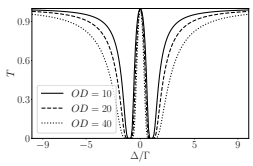

(c) Transmission for different values of the optical depth. $\Omega_c = 1$ in units of Γ.

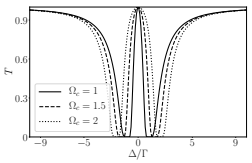

(d) Transmission for different values of the control field. $OD = 20$.

Figure 3.7: 3-level system analysis. The simulations are performed using the effective chain model that will be introduced in section 3.3.2. It is assumed $\Gamma_r = 0.5$.

understand how the propagation of the light takes place inside an EIT medium. How it is even possible to see propagation, considering that the speed of light is so high ($3 \cdot 10^8$ m/s) and that the ensembles of atoms we are referring to are so small (tens or hundreds of microns). How much the atoms can slow down the light.

When a probe field pulse approaches an atomic cloud, at the beginning of the process, only the atoms close to the first edge of the ensemble have been excited to the $|s\rangle$ state, and thus we perceive that the pulse is entering the medium. Then, over time, they get de-excited and the next atoms experience the transition to the $|s\rangle$ state and so on. At a certain point, looking at the population in $|s\rangle$, we can say that the whole pulse is inside the medium and, actually, we can notice that its spatial extension has been compressed. Then, we see the pulse travelling through the medium with a reduced group velocity v_g until it reaches the last edge of it and, eventually, when the atomic population of the storage state is again zero, we can say that it escaped the medium. The time needed by the pulse to cross the ensemble is called EIT-delay time, τ_{EIT}. This is how we see the information crossing the ensemble: it travels on a wave of atomic population in the $|s\rangle$ state of the atoms, that we call *spin wave*.

As above observed, since the dimensions of the clouds are so small compared to the speed of light, it is unrealistic to think that it happens because the light first arrives to the first atoms, then to the seconds and so on. The pulse illuminates the whole medium (all the atoms) at the same time. The reason why we see the spin wave travelling from the beginning to the end of the medium doesn't depend on the amplitude of the pulse, but on the phase information encoded in the propagation. A phase information that is transferred to the coefficients c_s of the atoms. It can be seen by considering a chain of atoms in the CW regime. Let's name z the axis of the chain, and use the apex/subscript n to label the atoms. We know that, in the steady state, the excited state coefficients are zero, and so we simply have [97]: $\Omega_p e^{ikz_n} c_g^n + \Omega_c c_s^n = 0$, where k is the wave vector of the laser field. Thus, the quantum state of the n-th atom results to be $|\psi_n\rangle \propto |g_n\rangle - \frac{\Omega_p}{\Omega_c} e^{ikz_n} |s_n\rangle$, and we clearly see how the phase information of the laser field is transferred to the atoms. Writing down the spin wave in the pulse case is slightly more complicated because it involves the time variation of the coefficients, but the meaning is exactly the same of what we have just seen[16].

[16]Indeed, also in the steady state the information travels through the medium, the only difference is that the amount of light going in and out the ensemble is the same at every instant of

While Ω_p determines the number of excitations inside the medium, Ω_c controls the dynamics of the system. In particular, as we will see in section 3.3.1, $v_g \propto \Omega_c^2$. Exploiting this principle, a quantum memory scheme based on EIT can be implemented. In this protocol, the quantum state encoded in the polarization of an incoming photon is stored in a spin wave, i.e. in a collective superposition of the $|s\rangle$ states of the atoms of the ensemble[17]. Once the whole pulse is well inside the ensemble, we switch off the control field in order to decouple the transition between $|s\rangle$ and $|e\rangle$, and to stuck the population in $|s\rangle$. Once that we switch the control field on again, the excitation can re-start to travel through the medium, in the same direction it was travelling before (since the information on the direction of propagation is also stored in the c_s coefficients).

We easily understand that the storage time of the memory must be smaller than the lifetime of the $|s\rangle$ states, but actually there is another (generally stricter) bound to consider: the dephasing time. In general, the information is stored in the phase relations between the complex amplitudes of the quantum state. When these relations are corrupted by some external factors, such as the interaction with the environment or the finite temperature of the system, we talk of dephasing. In the concrete case of an EIT atomic memory, the finite temperature of the system (around tens of μK) is the dephasing mechanism of highest impact, since it is responsible of the motion of the atoms. This motion changes the phase relations between the c_s coefficients (since the phases depend on z_n) in an unpredictable way, and it results in the loss of a portion of the excitation. Indeed, the transmission at zero detuning doesn't reach 1 anymore, but decreases with the decreasing of the amplitude of the control field. As a matter of fact, to a lower control field corresponds a lower propagation velocity, a bigger propagation time and, thus, the information has more time to dephase[18].

time.

[17] This is why we are indicating the third level of the atoms with $|s\rangle$, it is the storage level.

[18] It is worth mentioning a very well known formulation of the EIT in terms of dark-state polaritons [98, 99]. Here it is shown how the excitation inside the medium is both photonic and atomic, the control field weights these contributions and, when it is zero, the excitation is purely atomic, and so it cannot travel through the medium. The light travelling through the ensemble can be really very slow. In the famous experiment [100], the light speed inside the medium has been slowed down to 17 m/s, which in this mixed picture corresponds to have an excitation inside the medium that is nearly 100 % atomic.

3.3 Modelling Rydberg-EIT

We have already mentioned how complicated modelling quantum light-matter interaction in atomic ensemble is. The difficulties come from many different aspects. For example, the scattering pattern of an atomic cloud is very complicated. The light is multiply scattered in random directions by the random positioned atoms that, in addition, are also moving due to the finite temperature. Moreover, a single 2-level system acts as a nonlinear frequency mixer that can generate a continuum of frequencies from a given one[19]. Following how all these frequency components are evolving along the ensemble is something almost impossible. Eventually, if the quantum dynamics of the atoms wants to be taken into account, there is also a huge computational issue to tackle, the Hilbert space of a 2-level medium made of N atoms has a dimension of 2^N, the one of a 3-level medium grows as 3^N. In both cases, even below 20 atoms, we can run out of memory in a standard computer.

In this section, we describe two ways of facing these issues: the first one is based on Maxwell-Bloch equation (MB), and it is the historical way to study light-matter interaction in atomic ensembles; the second one is called spin model (SM), and it has been developed in recent years. The MB approach is a one-dimensional wave equation model where all the atoms are considered as independent and are modeled in the Maxwell's equation as a single smooth polarization field. Thus, it doesn't allow to include the collective interference phenomena that can take place in the atom dynamics and the multiple scattering patterns. Nevertheless, it is suitable for systems where these behaviours can be neglected, such as dilute gasses, and its complexity doesn't depend upon the optical depth of the system. On the other side, the SM is meant to include all the quantum interferences within the system, by directly solving an effective atom dynamics obtained by tracing out the electromagnetic degrees of freedom. Thus, it is indispensable in the study of dense ensembles and atomic lattices. Its main drawback lies in the fact that its computational cost grows exponentially with the number of atoms and, thus, proper tricks (depending on the number of excitations within the system) must be introduced to

[19] Let's consider two photons of frequency $\omega_1^{(in)}$ and $\omega_2^{(in)}$ approaching a 2-level system. In the scattering process, the conservation of the energy must be verified: $\omega_1^{(in)} + \omega_2^{(in)} = \omega_1^{(out)} + \omega_2^{(out)}$. This constraint doesn't imply that the energy of each photon is conserved, but they can mix and, even if we choose $\omega_1^{in} = \omega_2^{in}$, other frequencies will be generated as output. In particular, since the density of states corresponding to the excited level is a Lorentzian centred at the excited state energy ω_e of width Γ, very luckily a photon would be emitted at the transition frequency and the second would conserve the energy.

study high OD ensemble, e.g. effective Hamiltonian, quantum jumps, Matrix product states and so on.

3.3.1 Maxwell-Bloch approach

A first consideration to simplify the light-matter interaction in atomic ensemble, is to identify the quasi-1D nature that most of the experiments have. This is somehow a consequence of the directionality of the propagation of the laser, but the building of an equivalent 1D model is not straightforward, since it should also effectively capture the physics of the scattering in 4π. The historical way to simplify this problem was to drop off the granularity of the atoms and smooth them in a polarization marmalade, by substituting the polarization operators $\sigma^n_{ge}(t)$ of the single atoms with a single polarization field operator $\sigma_{ge}(z,t)$ for the whole medium. This polarization field becomes a source for the 1D-Maxwell's equations written in the electric laser field operator $E(z,t)$, and it is itself driven by the electric field. This model was first introduced in [101, 102], while a complete description can be found in [99, 103, 104]. In the case of a 2-level system, the Maxwell-Bloch equations can be written as follows [97]:

$$\left[\partial_t + c_0\partial_z\right] E(z,t) = in\sqrt{\frac{c_0\Gamma_1}{2}}\sigma_{eg}(z,t) \tag{3.4}$$

$$\left[i\Delta + \frac{\Gamma}{2} + \partial_t\right] \sigma_{ge}(z,t) = -i\sqrt{\frac{c_0\Gamma_1}{2}} E(z,t)\left[\sigma_{ee}(z,t) - \sigma_{gg}(z,t)\right] \tag{3.5}$$

,

where n is the density of the atoms, and where a factor $e^{ik_0 z}$ has been incorporated in E and σ_{ge}, to let them vary slowly along the ensemble (essentially these are the equations for the envelopes of the fields). In the weak driving regime, i.e. the number of atoms is much higher than the number of photons in the system, $\sigma_{ee} \approx 0$ and $\sigma_{gg} \approx 1$. Thus, the above system of nonlinear coupled PDEs reduces to:

$$\left[\partial_t + c_0\partial_z\right] E(z,t) = in\sqrt{\frac{c_0\Gamma_1}{2}}\sigma_{ge}(z,t) \tag{3.6}$$

$$\left[i\Delta + \frac{\Gamma}{2} + \partial_t\right] \sigma_{ge}(z,t) = i\sqrt{\frac{c_0\Gamma_1}{2}} E(z,t). \tag{3.7}$$

From this system, we can for example recover the Beer's law, i.e. the output intensity I is attenuated of e^{-OD} with respect to the input one I_0. Indeed, in

the CW regime, $\partial_t = 0$ and so we have

$$\partial_z E(z) = i\chi k_0 E(z) \Rightarrow E(z) = e^{i\chi k_0 z} E(0), \tag{3.8}$$

where the susceptibility of the medium χ results to be n times the susceptibility of the single atom:

$$\chi = n\chi_0 = \frac{n\Gamma_1}{2k_0} \frac{1}{\Delta - i\Gamma/2}. \tag{3.9}$$

In particular, at zero-detuning:

$$I = |E(L)|^2 = |e^{-nL\frac{\Gamma_1}{\Gamma}} E(0)|^2 = e^{-OD} I_0, \tag{3.10}$$

where $OD = 2N\frac{\Gamma_1}{\Gamma'} \simeq 2N\frac{\Gamma_1}{\Gamma}$. The (3.8) is telling us that in the far-detuned limit the medium is transparent to light, while at zero-detuning it is absorbing (see figure 3.5(b)). In general, when $\Delta \neq 0$, the imaginary part of the susceptibility determines the attenuation of the electric field, while the real part is responsible for the phase shift. This analysis also shows that considering a polarization field, rather than solving the atom dynamics, brings inevitably to the hypothesis of independent atoms, that is reflected in $\chi = n\chi_0$.

To use this approach to study the EIT case, we must add another polarization field σ_{gs} to the description of the system. Defining $\Delta_s = \omega_s - \omega_g$, we have

$$\begin{aligned}
\left[\partial_t + c_0\partial_z\right] E(z,t) &= in\sqrt{\frac{c_0\Gamma_1}{2}}\sigma_{ge}(z,t) && (3.11)\\
\left[i\Delta + \frac{\Gamma}{2} + \partial_t\right] \sigma_{ge}(z,t) &= i\sqrt{\frac{c_0\Gamma_1}{2}} E(z,t) + i\Omega_c\sigma_{gs}(z,t) && (3.12)\\
\left[i\Delta_s + \partial_t\right] \sigma_{gs}(z,t) &= i\Omega_c\sigma_{ge}(z,t). && (3.13)
\end{aligned}$$

Looking at the CW regime, and tuning the second laser exactly on the $e - s$ transition ($\Delta_s = \Delta$), we have:

$$\begin{aligned}
c_0\partial_z E(z) &= in\sqrt{\frac{c_0\Gamma_1}{2}}\sigma_{ge}(z,t) && (3.14)\\
\left[i\Delta + \frac{\Gamma}{2}\right] \sigma_{ge}(z,t) &= i\sqrt{\frac{c_0\Gamma_1}{2}} E(z,t) + i\Omega_c\sigma_{gs}(z,t) && (3.15)\\
i\Delta\sigma_{gs}(z,t) &= i\Omega_c\sigma_{ge}(z,t), && (3.16)
\end{aligned}$$

and it follows:

$$\partial_z E(z) = \frac{-n\Gamma_1\Delta}{2i\left(\Delta^2 - \Omega_c^2\right) + \Gamma\Delta} E(z) = ik_{eff} E(z), \tag{3.17}$$

where k_{eff} is an effective complex wave vector. Since the transmission is defined as $T = I/I_0$, we have $T = |e^{ik_{eff}L}|^2$. We first notice that $T(\Delta = 0) = 1$. It is a direct consequence of the fact that there is no population in the excited states at zero-detuning (see (3.16)), and that the lifetime of the storage level is much longer than the time scale of the experiment.

Then we can compute the width of the window of transparency Δ_{EIT}, and the parameter of the dispersionless propagation of a pulse centered at $\Delta = 0$ and of frequency spectrum well inside Δ_{EIT}, i.e. the group velocity v_g and the EIT-delay τ_{EIT}. To do that, we can expand k_{eff} up to the second order in the detuning:

$$k_{eff} = \frac{in\Gamma_1\Delta}{\Gamma\Delta + 2i(\Delta^2 - \Omega_c^2)} \simeq -\frac{n\Gamma_1}{2\Omega_c^2}\Delta + i\frac{n\Gamma\Gamma_1}{4\Omega_c^4}\Delta^2. \tag{3.18}$$

From the first derivative we have the parameters of the dispersionless propagation $v_g = (\partial_\Delta k_{eff})^{-1}_{\Delta=0} = \frac{2\Omega_c^2}{n\Gamma_1} = \frac{4\Omega_c^2 L}{OD\Gamma}$ and $\tau_{EIT} = L/v_g = \frac{nL\Gamma_1}{2\Omega_c^2} = \frac{N\Gamma_1}{2\Omega_c^2} = \frac{OD\Gamma}{4\Omega_c^2}$. While the second derivative gives us information on the dispersion along the propagation. To compute Δ_{EIT}, we use the definition $T > 1/e$, and so we get $\Delta_{EIT} = \frac{4\Omega_c^2}{\Gamma\sqrt{OD}}$ (see figures 3.7(c)-3.7(d)). So, a pulse centered at $\Delta = 0$ and whose frequency spectrum is well inside the transparency band propagates through the medium at a reduced group velocity v_g dictated by the control field. And, in particular, the possibility of realizing quantum memories based on this EIT principle is a direct consequence of the fact that $\Omega_c = 0$ implies $v_g = 0$.

Eventually, let us observe that if we want to study the R-EIT case using the Maxwell-Bloch equations, we have to extend the derivation to the double-excitation component of the wave function and we have to introduce an interaction potential between the Rydberg states. The dynamical system becomes more complex. A complete description can be found in the supplementary material of [79].

Symmetry considerations on EIT

Here we want to make some symmetry considerations that could help to understand EIT a bit more. Let's consider a Gaussian pulse of frequency width $\Delta\omega = c\Delta k$ approaching the medium, and let's first focus on the transition from outside to inside. If we keep the parameters of the system fixed in time, the entering the medium is time invariant, in the sense that shifting the time axis doesn't change the physics. It follows the conservation of the energy

and, so, the conservation of $\Delta\omega$ between outside and inside[20]. On the contrary, since the pulse crosses an interface, the system is clearly not space invariant and, thus, Δk do change. Its variation can be easily computed by considering how the dispersion relation changes from outside ($\omega = ck$) to inside ($\omega = v_g k$), and by imposing the conservation of $\Delta\omega$. It follows that $(\Delta k)_{in} = \frac{c}{v_g}(\Delta k)_{out}$, and from here we derive (considering the Fourier indetermination relation between Δz and Δk) the above mentioned compression of the pulse. In particular, the pulse is compressed by a factor given by the ratio between the two group velocities: $(\Delta z)_{in} = \frac{v_g}{c}(\Delta z)_{out}$ (see figure 3.8).

Moreover, also the memory mechanism can be well understood via a symmetry principle. Once that the whole pulse is well inside the medium, we can say that the space is now somehow invariant from the pulse point of view, since it doesn't see interfaces around it anymore. Thus, until it doesn't reach the second edge of the ensemble, $(\Delta k)_{in}$ does not change. On the contrary, if we now change the value of the Rabi frequency of the control field from Ω_{c1} to Ω_{c2}, indicating with v_{g1} and v_{g2} the corresponding group velocities, we have $(\Delta\omega)_{\Omega_{c2}} = \frac{v_{g2}}{v_{g1}}(\Delta\omega)_{\Omega_{c1}}$. In particular, for $\Omega_{c2} = 0$ we get $v_{g2} = 0$, and so $(\Delta\omega)_{\Omega_{c2}} = 0$[21].

We can understand how many spatially separated photons can be stored in an EIT quantum memory at the same time with the following argument. Let's focus on Gaussian pulses, where we know that $\Delta z = 1/\Delta k$. We can compute the maximum number of storable pulses for a given medium of length L by minimizing the denominator of $L/(\Delta z)_{in}$. $(\Delta z)_{in} = 1/(\Delta k)_{in}$ is minimum when $(\Delta k)_{in}$ is maximum and, since $(\Delta k)_{in} = (\Delta\omega)_{in}/v_g = (\Delta\omega)_{out}/v_g$, to maximize it we need to consider the maximum possible frequency width for $(\Delta\omega)_{out}$, namely Δ_{EIT}. So, it follows that the maximum number of Gaussian pulses simultaneously storable inside the medium is $\frac{L}{v_g}\Delta_{EIT} = \tau_{EIT}\Delta_{EIT}$. It proves that the bandwidth-delay product is the figure of merit to consider to quantify this storage concept. Moreover, since $\Delta_{EIT} = \frac{4\Omega_c^2}{\Gamma\sqrt{OD}}$ and $\tau_{EIT} = \frac{OD\Gamma}{4\Omega_c^2}$, we have that $\tau_{EIT}\Delta_{EIT} = \sqrt{OD}$ [22]. Thus, it doesn't depend upon Ω_c and this is an example where the optical depth of the 2-level medium bounds

[20] We consider negligible the portion of the pulse that is reflected back by the medium.

[21] Even if this physics doesn't depend on the fact that we are considering a cloud or a lattice, in the lattice case we can give an extra look at this problem. Indeed, here we have a band structure whose slope, in a given wave number k, is the group velocity of a pulse centred in k and travelling through the medium. This slope is determined by the control field and, when Ω_c goes to zero, the band becomes flat. The conservation of Δk in this process forces $\Delta\omega$ to be 0.

[22] A real number calculation in the 3D ensemble leads to $\tau_{EIT}\Delta_{EIT} \approx 0.2\sqrt{OD}$. In the experiment of [79], where $OD \approx 50$ is reached, it implies that the number of simultaneously

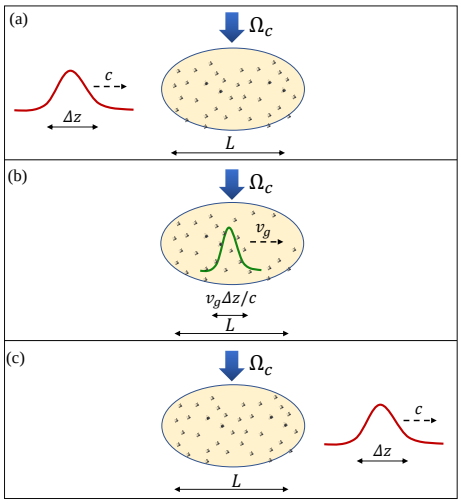

Figure 3.8: Sketch of the slow light propagation and of the pulse compression.

the performance of a concrete device.

3.3.2 Spin Model

[23]Robert Henry Dicke, in 1956, pointed out, for the first time, the importance of the interference phenomena in atomic ensembles. He showed how they could lead to peculiar enhancements of the radiation rate, via the mechanism nowadays known as *superradiance*. From that time on, the focus has been put on finding a way to include interference in the description of such systems. This effort took form in the development of a sophisticated quantization scheme [105, 106] for the electromagnetic field that, contrary to the traditional quantization in free space and in dielectrics [107], is not based on a modal expansion of the electromagnetic field, but it uses only the Green's tensor of the system. Modal expansions are well suited only when few modes are relevant for the dynamics [105, 108], but become quite intricate in other cases. On the contrary, the Green's tensor based method proves to be enlightening.

One of the main consequences of this new quantization scheme is what we call *Spin Model* (SM). The SM faces the complex problem of solving the full

storable photons is between 1 and 2.

[23]We will mostly follow the treatment of [97].

dynamics of the light scattered by fixed position atoms, taking into account all the multiple scattering events and the interference phenomena. It consists of building an effective open quantum model containing *only* the atomic degrees of freedom and the incident field [94, 97, 109]. The spin model consists of two steps: solving an effective dynamics in the atomic degrees of freedom and, then, reconstructing the field via an input-output relation.

Let's start from the input-output relation. A formal derivation of it can be found in [110] but to get an idea, let us consider the scattering by N polarizable classical dipole $\boldsymbol{p}_j(t)$ placed in $\boldsymbol{r}_j$ points of the space. Named $\boldsymbol{E}_p(\boldsymbol{r}, t)$ the input (probe) field, in the frequency domain, the following expression of the total field holds:

$$\boldsymbol{E}(\boldsymbol{r}, \omega) = \boldsymbol{E}_p(\boldsymbol{r}, \omega) + \mu_0 \omega^2 \sum_{j=1}^{N} \boldsymbol{G}\left(\boldsymbol{r}, \boldsymbol{r}_j, \omega\right) \cdot \boldsymbol{p}_j(\omega), \tag{3.19}$$

where $\boldsymbol{G}$ is the Green's tensor, solution of the wave equation

$$\nabla \times \nabla \times \boldsymbol{G}(\boldsymbol{r}, \omega) - \frac{\omega^2}{c_0^2} \epsilon(\boldsymbol{r}, \omega) \boldsymbol{G}(\boldsymbol{r}, \boldsymbol{r}', \omega) = \delta(\boldsymbol{r} - \boldsymbol{r}') \mathbf{1}, \tag{3.20}$$

that is computed taking into account all the features of the surrounding environment. In the vacuum case, $\boldsymbol{G}$ only depends on the distance between the two points ($d = |\boldsymbol{d}| = |\boldsymbol{r} - \boldsymbol{r}'|$) and it has the analytic expression:

$$\boldsymbol{G}(d, \omega) = \frac{e^{ikd}}{4\pi k^2 d^3} \left[\left(k^2 d^2 + ikd - 1\right) \mathbf{1} + \left(-k^2 d^2 - 3ikd + 3\right) \frac{\boldsymbol{d} \otimes \boldsymbol{d}}{d^2} \right]. \tag{3.21}$$

Despite its easy writing, the (3.19) encodes a complex problem, since the $\boldsymbol{p}_j(\omega)$ depend on $\boldsymbol{E}_p(\boldsymbol{r}, \omega)$ and are all coupled together. The (3.19) can be brought to the quantum world promoting $\boldsymbol{p}_j(\omega)$ to the dipole moment operator $\boldsymbol{p}_j(\omega) = \boldsymbol{\mathcal{P}}^*(\omega)\sigma_{eg}^j + \boldsymbol{\mathcal{P}}(\omega)\sigma_{ge}^j$ (where $\boldsymbol{\mathcal{P}}(\omega)$ is the dipole matrix element) and $\boldsymbol{E}(\boldsymbol{r}, \omega)$ to the field operators $\boldsymbol{E}^+(\boldsymbol{r}, \omega)$ and $\boldsymbol{E}^-(\boldsymbol{r}, \omega)$, where the apexes refer to the positive/negative-frequency components [105, 109, 111]:

$$\boldsymbol{E}^+(\boldsymbol{r}, \omega) = \boldsymbol{E}_p^+(\boldsymbol{r}, \omega) + \mu_0 \omega^2 \sum_{j=1}^{N} \boldsymbol{G}\left(\boldsymbol{r}, \boldsymbol{r}_j, \omega\right) \cdot \boldsymbol{\mathcal{P}}(\omega) \sigma_{ge}^j, \tag{3.22}$$

and $\boldsymbol{E}^-(\boldsymbol{r}, \omega)$ is the adjoint operator of $\boldsymbol{E}^+(\boldsymbol{r}, \omega)$. The (3.22) can be simplified observing that the response of an atom is highly picked around the frequency

transition that we are considering $\omega_0 = \omega_{eg} = \omega_e - \omega_g$. Thus, observing that $\boldsymbol{\mathcal{P}}(\omega) \sim \boldsymbol{\mathcal{P}}\delta(\omega - \omega_0)$, we get

$$\boldsymbol{E}^+(\boldsymbol{r},\omega) = \boldsymbol{E}_p^+(\boldsymbol{r},\omega) + \mu_0\omega_0^2 \sum_{j=1}^{N} \boldsymbol{G}\left(\boldsymbol{r},\boldsymbol{r}_j,\omega_0\right)\cdot\boldsymbol{\mathcal{P}}\delta(\omega-\omega_0)\sigma_{ge}^j, \quad (3.23)$$

that in the time domain results to be

$$\boldsymbol{E}^+(\boldsymbol{r},t) = \boldsymbol{E}_p^+(\boldsymbol{r},t) + \mu_0\omega_0^2 \sum_{j=1}^{N} \boldsymbol{G}\left(\boldsymbol{r},\boldsymbol{r}_j,\omega_0\right)\cdot\boldsymbol{\mathcal{P}}\sigma_{ge}^j. \quad (3.24)$$

This approximation is valid when we deal with setups where the retardation between the atoms is negligible [96,112][24] and when the electromagnetic environment doesn't have a very narrow-bandwidth response (e.g. strong coupling in cavity-QED [113]) [97].
The direct inverse transform of (3.22) leads to a convolution relation between the polarization of the atoms and the electric field in the time domain, that has to be taken into account when non-Markovian regimes want to be investigated[25].

For what concerns the effective atom dynamics, it is derived starting from the general density matrix of the system ρ, that encodes both the atomic and the electromagnetic degrees of freedom, and then tracing out the electromagnetic ones. In this way, it is derived the Master equation that dictates the evolution of the reduced density matrix $\rho_A = Tr\left[\rho\right]_{EM}$, which accounts only for the atomic degrees of freedom [97]:

$$\dot{\rho}_A = -\frac{i}{\hbar}\left[\mathcal{H},\rho_A\right] + \mathcal{L}\left[\rho_A\right]. \quad (3.25)$$

[24] In the free-space atom case, the length of a spontaneous emitted photon is in the order of 1 m, thus we simply need $d \ll 1$ m.

[25] Let's for example consider an atom close to a photonic crystal. Here, the dispersion relation $\omega(k)$ exhibits some intervals of k where the band is almost flat, i.e. some regions where the group velocity is almost zero. An emitted photon at these k would not travel away from the atom and would keep on staying close to it, with the consequent probability to be reabsorbed. In this case, all the memory effects are important and cannot be ignored. On the contrary, in free-space, an emitted photon would travel away from the atom at the speed of light [114–117].

In eq. (3.25), the Hamiltonian and the Lindblad operator are[26]:

$$\mathcal{H} = \hbar\omega_0 \sum_{i=1}^{N} \sigma_{ee}^{i} + \hbar \sum_{i,j=1}^{N} J^{ij} \sigma_{eg}^{i} \sigma_{ge}^{j} \tag{3.26}$$

$$\mathcal{L} = \sum_{i,j=1}^{N} \frac{\Gamma^{ij}}{2} \left(2\sigma_{ge}^{j} \rho_A \sigma_{eg}^{i} - \sigma_{eg}^{i} \sigma_{ge}^{j} \rho_A - \rho_A \sigma_{eg}^{i} \sigma_{ge}^{j} \right), \tag{3.27}$$

where

$$J^{ij} = -\frac{\mu_0 \omega_0^2}{\hbar} \boldsymbol{\mathcal{P}}^* \cdot \Re \left[\boldsymbol{G} \left(\boldsymbol{r}_i, \boldsymbol{r}_j, \omega_0 \right) \right] \cdot \boldsymbol{\mathcal{P}} \tag{3.28}$$

$$\Gamma^{ij} = \frac{2\mu_0 \omega_0^2}{\hbar} \boldsymbol{\mathcal{P}}^* \cdot \Im \left[\boldsymbol{G} \left(\boldsymbol{r}_i, \boldsymbol{r}_j, \omega_0 \right) \right] \cdot \boldsymbol{\mathcal{P}}. \tag{3.29}$$

The atom dynamics can also be solved by considering an equivalent description, based on the quantum jump formalism for open systems [120]. It consists of letting the system evolve in a deterministic fashion under an effective non-Hermitian Hamiltonian:

$$\mathcal{H}_{eff} = \hbar\omega_0 \sum_{i=1}^{N} \sigma_{ee}^{i} - \mu_0 \omega_0^2 \sum_{i,j=1}^{N} \boldsymbol{\mathcal{P}}^* \cdot \boldsymbol{G} \left(\boldsymbol{r}_i, \boldsymbol{r}_j, \omega_0 \right) \cdot \boldsymbol{\mathcal{P}} \sigma_{eg}^{i} \sigma_{ge}^{j}, \tag{3.30}$$

and then randomly applying some operators, namely the "quantum jumps", to account for the recycling of the population (represented by the term $\sigma_{ge}^{j} \rho_A \sigma_{eg}^{i}$ in the Lindblad operator). In other words, these quantum jumps are needed because the non-Hermitian evolution of the system violates many properties of the quantum state. In particular, it does not preserve the norm of it: since (3.30) doesn't allow the re-population of the ground state, if an atom of the ensemble decays from $|e\rangle$ to $|g\rangle$, the norm of the quantum state decreases.

Let's notice that the (3.30) has an incredibly simple and beautiful interpretation. Indeed, the interaction term is the sum of contributions that describe how the atoms exchange energy: the atom j, undergoing a transition from $|e\rangle$ to $|g\rangle$, emits a photon at the transition frequency ω_0, that propagates from $\boldsymbol{r}_j$ to $\boldsymbol{r}_i$ via the Green's function and gets absorbed by the atom i.

Weak driving regime

The spin model problem largely simplifies in the weak driving regime. Indeed, when the number of photons in the system is much smaller than the number

[26] We refer to the notation of [97], that in turn refers to [94, 105, 106, 118, 119].

of atoms, the quantum state is mostly $|g\rangle = |g_1\ g_2\ \dots\rangle$, and so, assuming the following expansion for the wave function[27]:

$$\begin{aligned} |\psi\rangle = c_g|g\rangle \quad &+ \quad c_e^1|e_1\rangle + c_e^2|e_2\rangle + \dots + c_{ee}^{12}|e_1\ e_2\rangle + c_{ee}^{13}|e_1\ e_3\rangle + \dots \\ &+ \quad c_{eee}^{123}|e_1\ e_2\ e_3\rangle + c_{eee}^{124}|e_1\ e_2\ e_4\rangle + \dots, \end{aligned} \tag{3.31}$$

in the weak driving regime, we have $c_g \sim 1$. Thus, fixing $c_g = 1$ and tolerating fluctuations of the norm of the wave function around 1, we can avoid the use of the quantum jumps and let the system evolve under the effective non-Hermitian Hamiltonian. Thus, we can correctly describe the physics of the 0-1-2 excitation subspace via the deterministic Schrödinger equation:

$$i\hbar\,\partial_t|\psi\rangle = \mathcal{H}_{eff}|\psi\rangle. \tag{3.32}$$

It is worth noting that, in the weak driving scenario, we are able to simulate the dynamics of a much larger number of atoms, since we do not need to consider the full Hilbert space in the evolution. We can, indeed, truncate it to the 0-1 excitation subspace to study the linear properties, and to the 0-1-2 excitation one to study the correlations. Thus, instead of dealing with a Hilbert space of dimension 2^N, we implement a truncation of it, of dimension $1 + N$ in the first case and of dimension $1 + N + N(N-1)/2$ in the second case. In appendix A, we describe how to represent the quantum operators on these truncation of the Hilbert space. From now on, we will refer only to the weak driving regime.

Effective atomic chain

Now that we have introduced the general features of the SM, we can wonder how exploiting the quasi-1D nature of an experiment in it. This can be done by designing an effective chain of atoms (see figure 3.9) where again, as discussed qualitatively in section 3.2.1, the total decay rate Γ is spitted into two contributions: the decay rate in the driving mode Γ_1 and the decay rate in the noncollectable directions of the space Γ'. In writing the effective Hamiltonian, it is now important to consider the one-dimensional Green's function of the wave equation, since we are assuming that a photon emitted by an atom and reabsorbed by another travels on a line with wave number k_1. By fixing the

[27] We use the notation $|e_n\rangle = \sigma_{eg}^n|g\rangle = |g_1\ g_2\ \dots\ g_{n-1}\ e_n\ g_{n+1}\ \dots\rangle$.

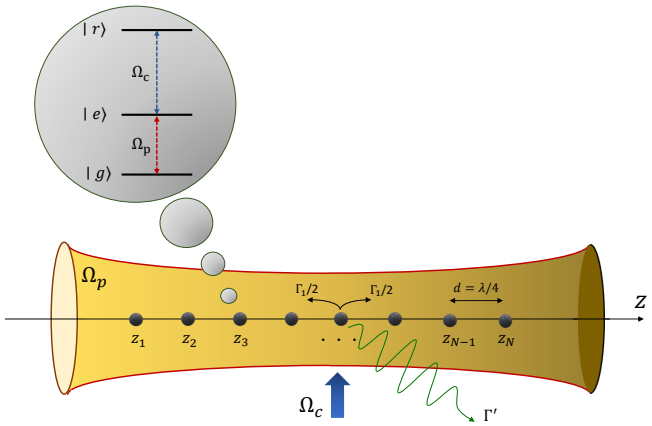

Figure 3.9: Sketch of the effective atom chain model.

polarization of the detection mode, the effective Hamiltonian and the input-output relation read:

$$\mathcal{H}_{eff} = \hbar\left[\omega_0 - i\Gamma'/2\right]\sum_{i=1}^{N}\sigma_{ee}^{i} - i\frac{\hbar\Gamma_1}{2}\sum_{i,j=1}^{N}e^{ik_1|z_i-z_j|}\sigma_{eg}^{i}\sigma_{ge}^{j} \tag{3.33}$$

$$E^{+}(z,t) = E_p^{+}(z,t) + i\frac{\Gamma_1}{2}\sum_{i=1}^{N}e^{ik_1(z-z_i)}\Theta(z-z_i)\sigma_{ge}^{i}, \tag{3.34}$$

where z_i is the position of the atom i along the chain, and where we are working in unit of measure where the electric field has the dimension of a frequency. For such a system, the optical depth results to be $OD = 2N\Gamma_1/\Gamma' = 2N\Gamma_r$ and thus we will make a proper choice of Γ_r and N in order to reproduce the same OD of the experiment that we are studying, and to tackle the numerical issue due to the large dimension of the Hilbert space. In addition, it is important to minimize the back reflection from the chain. This can be done by choosing a proper inter-atomic distance, i.e. $|z_i - z_{i+1}| = n\lambda/4$ with n odd.

Taking all the above requirements, this effective chain of atoms is able to simulate the quasi-1D physics of a real 3D cloud, at least in its main features. Moreover, it is important to mention that it exists a real physical system de-

scribed by the (3.33)-(3.34): a chain of atoms coupled to a nanofiber. The full description of this system can be found in [94, 109].

In the following, we will work in the rotating frame, i.e. $\tilde{c}_e(t) = c_e(t)e^{i\omega_0 t}$ (we will simply write c_e instead of $\tilde{c}_e$), and we will only consider classical probe fields, $E_p^+(z,t) = E_p(z,t) = \Omega_p(t)e^{i\omega_p t + ik_1 z}$. The (3.33)-(3.34) become

$$\mathcal{H}_{eff} = -i\frac{\hbar\Gamma'}{2}\sum_{i=1}^{N}\sigma_{ee}^{i} - i\frac{\hbar\Gamma_1}{2}\sum_{i,j=1}^{N} e^{ik_1|z_i - z_j|}\sigma_{eg}^{i}\sigma_{ge}^{j} \quad (3.35)$$

$$E^+(z,t) = \Omega_p(t)e^{ik_1 z} + i\frac{\Gamma_1}{2}\sum_{i=1}^{N} e^{ik_1(z-z_i)}\Theta(z-z_i)\sigma_{ge}^{i}. \quad (3.36)$$

The (3.35) describes the effective interaction between the atoms, but the full Hamiltonian of the system must include also the contribution of the driving/probe field, that in the rotating frame system reads:

$$\mathcal{H}_p = -\hbar\Delta\sum_{i=1}^{N}\sigma_{ee}^{i} - \hbar\sum_{i=1}^{N}\left[\Omega_p(t)e^{ik_1 z}\sigma_{eg}^{i} + h.c.\right]. \quad (3.37)$$

In the EIT scenario, a term in the Hamiltonian accounting for the control field has to be included:

$$\mathcal{H}_c = -\hbar\Delta_s\sum_{i=1}^{N}\sigma_{ss}^{i} - \hbar\sum_{i=1}^{N}\left[\Omega_c(z_i,t)\sigma_{se}^{i} + h.c.\right], \quad (3.38)$$

and if the storage states are Rydberg states[28], the description must be completed considering also the Rydberg interaction:

$$\mathcal{H}_R = -\sum_{i,j=1}^{N} V(|z_i - z_j|)\sigma_{rr}^{i}\sigma_{rr}^{j}, \quad (3.39)$$

where $V(|z_i - z_j|) \sim |z_i - z_j|^{-6}$. Eventually, the motional dephasing can be effectively included in the description by adding a finite lifetime to the Rydberg states[29].

[28] In the Rydberg case we use the operators σ_{er} and σ_{re} instead of σ_{es} and σ_{se}.

[29] It is worth observing that the effective chain can model cigar shaped clouds where the Rydberg blockade is bigger than the transverse section of the ensemble. Otherwise, more channels for the excitation to travel are opened.

3.3.3 Our numerical choice

Since in the following we will mostly refer to dilute clouds of atoms, both the MB approach and the SM chain are indeed possible and, in particular, it has been proven that the latter provides the same results of the former in the hypothesis of sufficiently small Γ_r and sufficiently large N [109]. To perform the simulations, we use the effective chain of atoms introduced in section 3.3.2, and we truncate the Hilbert space up to the double-excitation subspace. Moreover, to capture the real blockade physics, we consider infinite blockade radius and infinite strength of the Rydberg interaction along the chain. We do that by directly preventing the double Rydberg occupation in the expansion of the wave function:

$$\begin{aligned}|\psi\rangle = |g\rangle + \sum_n c_e^n |e_n\rangle + \sum_n c_r^n |r_n\rangle + \sum_{\substack{n,m \\ n<m}} c_{ee}^{nm} |e_n e_m\rangle \\ + \sum_{\substack{n,m \\ n<m}} c_{er}^{nm} |e_n r_m\rangle + \sum_{\substack{n,m \\ n<m}} c_{re}^{nm} |r_n e_m\rangle,\end{aligned} \tag{3.40}$$

and so we do not need to include (3.39) in the description of the system.

The dynamics is computed by plugging the expansion (3.40) in the Schrödinger equation:

$$\hbar \partial_t \psi = \left[\mathcal{H}_{eff} + \mathcal{H}_p + \mathcal{H}_c\right] \psi. \tag{3.41}$$

The following system of ordinary differential equations for the coefficients is

obtained:

$$\dot{c}_e^n = \left[i\Delta - \frac{\Gamma}{2}\right] c_e^n + i\Omega_c c_r^n + i\Omega_p e^{ik_1 z_n} - \frac{\Gamma_1}{2}\sum_{m\neq n} e^{ik_1|z_n - z_m|} c_e^m + \\ + i\Omega_p \sum_{m\neq n} e^{-ik_1 z_m} c_{ee}^{(mn)} \tag{3.42}$$

$$\dot{c}_r^n = i\Delta_s c_r^n + i\Omega_c c_e^n + i\Omega_p \sum_{m<n} e^{-ik_1 z_m} c_{er}^{mn} + i\Omega_p \sum_{m>n} e^{-ik_1 z_m} c_{re}^{mn} \tag{3.43}$$

$$\dot{c}_{ee}^{nm} = [2i\Delta - \Gamma]\, c_{ee}^{nm} + i\Omega_c \left(c_{er}^{nm} + c_{re}^{nm}\right) + i\Omega_p \left(e^{ik_1 z_n} c_e^m + e^{ik_1 z_m} c_e^n\right) \\ - \frac{\Gamma_1}{2}\sum_{h\neq n,m} e^{ik_1|z_m - z_h|} c_{ee}^{(nh)} - \frac{\Gamma_1}{2}\sum_{h\neq n,m} e^{ik_1|z_n - z_h|} c_{ee}^{(mh)} \tag{3.44}$$

$$\dot{c}_{er}^{nm} = \left[i\Delta_s + i\Delta - \frac{\Gamma}{2}\right] c_{er}^{nm} + i\Omega_c c_{ee}^{nm} + i\Omega_p e^{ik_1 z_n} c_r^m \\ - \frac{\Gamma_1}{2}\sum_{\substack{h\neq n \\ h<m}} e^{ik_1|z_n - z_h|} c_{er}^{hm} + -\frac{\Gamma_1}{2}\sum_{\substack{h\neq n \\ h>m}} e^{ik_1|z_n - z_h|} c_{re}^{mh} \tag{3.45}$$

$$\dot{c}_{re}^{nm} = \left[i\Delta_s + i\Delta - \frac{\Gamma}{2}\right] c_{re}^{nm} + i\Omega_c c_{ee}^{nm} + i\Omega_p e^{ik_1 z_m} c_r^n \\ - \frac{\Gamma_1}{2}\sum_{\substack{h\neq m \\ h>n}} e^{ik_1|z_m - z_h|} c_{re}^{nh} + -\frac{\Gamma_1}{2}\sum_{\substack{h\neq m \\ h<n}} e^{ik_1|z_m - z_h|} c_{er}^{hn}, \tag{3.46}$$

where $c_{ee}^{(nm)}$ is a synthetic notation that stays for c_{ee}^{nm} if $n < m$ and c_{ee}^{mn} if $m > n$. All the energy levels and the interactions involved in the dynamics described by the system (3.42)-(3.46) can be represented graphically as shown in figure 3.10.

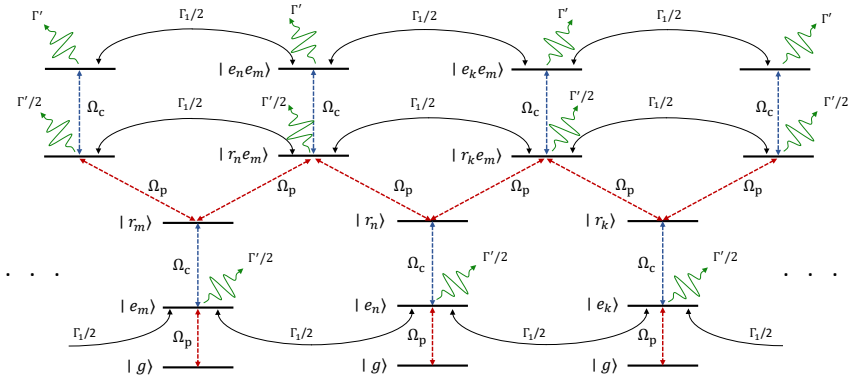

(a) Full representation.

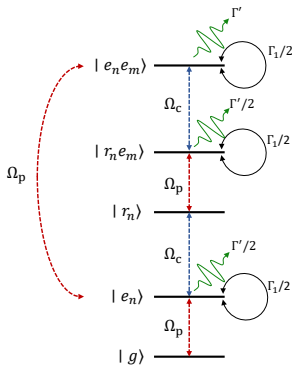

(b) Simplified representation.

Figure 3.10: Graphic representation of the atomic level structure and of the interactions dictated by system (3.42)-(3.46).

3.4 Nonlinearities in Rydberg-EIT

[30]The previous sections have been devoted to the deep understanding of why Rydberg-EIT can be crucial in pursuing the long-standing goal of establishing

[30]In this section, the original analyses of the authors are illustrated.

deterministic nonlinear photon-photon interaction, to a careful treatment of the light-matter interaction in atomic ensembles, and to the development of efficient tools to theoretically study these complex dynamics. We are now ready to quantitatively discuss the nonlinear behaviours exhibited by cold gasses of Rydberg atoms, in the EIT setup. The Rydberg clouds are modeled by the effective atomic SM chains introduced in section 3.3.2, and they are discussed both in the continuous wave regime and in the transient one. With a particular attention on their capability to turn classical light into quantum light. This section represents the core of this thesis chapter.

Second-order correlation function

Let's start by obrserbing that, while in the classical world, a nonlinear system is a system that shows a nonlinear relation between the output and the input fields, at the quantum scale, a nonlinear medium is something able to turn classical light into quantum light. To quantify "how good" a nonlinear behavior at the few photon level is, we consider a coherent probe field (classical light) illuminating the ensemble and evaluate the zero-delay normalized second-order correlation function at the end of the chain, the so-called $g^{(2)}$ function. This positive function is ≥ 1 for classical light (in particular $= 1$ for coherent fields), and < 1 for quantum light (in particular $= 0$ for single photon light). A nonlinear system, thus, turns an input $g^{(2)} = 1$ light into an output $g^{(2)} < 1$ one. Even if a zero $g^{(2)}$ is formally only a necessary condition for a perfect nonlinear system, in the specific case of Rydberg-EIT, the statement "the smaller the output $g^{(2)}$, the better the nonlinearity" can be considered true. It is formally defined as the ratio between the second-order correlation function $G^{(2)}$ and the square of the intensity I:

$$g^{(2)}(t) \doteq \frac{G^{(2)}(t)}{[I(t)]^2} = \frac{\langle\psi(t)|E^-E^-E^+E^+|\psi(t)\rangle}{\langle\psi(t)|E^-E^+|\psi(t)\rangle^2}. \tag{3.47}$$

Theoretically, $I(t)$ and $G^{(2)}(t)$ are the quantum averages of the 1-photon detection operator and of the 2-photon one, respectively. While experimentally $g^{(2)}$ is computed by taking the ratio between the double-photon detection count and the single-photon detection one, after thousands of trials[31]. A quantum state of light is said to be *bunched* if $g^{(2)} > 1$, and we can think of it imagining that, in this case, the photons prefer to travel in groups, while it is said to

[31] An ergodic hypothesis on the system ensures that these two averages coincide.

be *antibunched* when $g^{(2)} < 1$, and in this case they prefer to travel alone[32]. Thus, at the quantum level, a nonlinear system suppresses the 2-photon component of the input quantum state. This is exactly what we imagined the Rydberg blockade would have done: introducing a space-time separation between the photons travelling through the ensemble, that prevents them to cross it in groups.

$G^{(2)}$ is a double-excitation quantity, in the sense that depends on the double-excitation component on the wave function and, in particular, since to detect two photons, two excited states must be populated, it depends on the value of the c_{ee} coefficients. Analogously, I is determined once we know the value of the c_e coefficients. In general, the dynamics of the single-excitation and of the double-excitation components are strictly intertwined, and that makes the general expression of the $g^{(2)}$ not only almost impossible to derive analytically, but also very hard to guess. So, it is important to look for some situations where the two dynamics can be split. In the following, the steady state and the transient analyses of the nonlinearity in the Rydberg ensemble are presented.

3.4.1 Steady state regime

To study the fundamental blockade physics, we send the Rydberg blockade and the Rydberg potential to infinity. In this way, the value of the $g^{(2)}$ can only depend on the optical depth OD and on the control field Ω_c. An easy picture of the problem can be obtained by looking at a simplified version of the two-photon propagation along the medium. We imagine that a first photon can cross the ensemble travelling on the transparency band. This photon, populating the Rydberg states of the atoms, is transmitted on the other side of the ensemble with probability one. Its Rydberg occupation has the effect of shifting the Rydberg levels of the surrounding atoms through the blockade mechanism. Now, due to this blockade, a second photon sees a 2-level medium and gets absorbed by that, with the consequent probability of being transmitted of e^{-OD}. Thus, we expect something like $g_{ss}^{(2)} \sim e^{-OD}$.

However, this simplified look at the problem doesn't highlight the role of the control field. In this sense, we expect that to a slower propagation, i.e. to a smaller Ω_c, would correspond a smaller $g_{ss}^{(2)}$, since the photons would have

[32]Even if the $g^{(2)}$ is not a well-defined probability, since it could be greater than 1, within the contest of quantum lights, it can be somehow considered as if it were the probability of detecting two photons at the same time. In the sense that developing imagination on this idea, even if formally incorrect, is not useless.

more time to interact. As a matter of fact, the real picture is more sophisticated than this. The two photons cross the ensemble at the same time, and so the problem has to be solved in the relative coordinates. In the supplementary material of [79], this analysis has been carefully done using the MB method. They have shown how to trace back the full dynamics to a single partial differential equation in the 2-photon component that, in the limit of large OD, admits the following approximate analytic expression:

$$g_{ss}^{(2)} \approx \frac{4\left[1+(\Omega_c/\Gamma)^2\right]}{\pi OD} \exp\left[\frac{-OD}{\sqrt{1+(\Omega_c/\Gamma)^2}}\right], \tag{3.48}$$

that is not so far from the guessed e^{-OD}, but it points out the role of the control field. The (3.48) also shows that, when $\Omega_c \ll \Gamma$, the control field disappears $g_{ss}^{(2)} \approx \frac{4}{\pi OD} e^{-OD}$.

From the (3.48), we see that the value of the $g^{(2)}$ in the CW regime increases with the control field and decreases with the optical depth. Of course, from the experimental point of view, there are some limitations on the smallest value of the control field and on the biggest value of the optical depth that can be chosen. The motional dephasing forbids an extremely small Ω_c, that would lead to have a zero transmission, even at $\Delta = 0$. While an incredibly high OD results in the trapping of a very long ensemble. This can be done, but then the beam diffraction increases the minimum possible beam waist. And thus, in turn, we need a larger blockade radius to blockade the entire transverse area. Generally, the ensembles used in this contest are cigar shaped and the blocking of the transverse area is fundamental to preserve the quasi-1D nature of the experiment. Indeed, a partial transverse blockade would open another channel for the information to travel, allowing two photons to cross the ensemble in parallel without interacting at all.

In the spin model modelling of R-EIT, in the CW regime, the c_e coefficients of expansion (3.40) are null, and thus $I/\Omega^2 = 1$. While the Rydberg interaction makes the coefficients $c_{ee} \neq 0$, and, in particular, it returns $G^{(2)}/\Omega^4 < 1$. In figure 3.11, we show the SM computation of the $g_{ss}^{(2)}$ for different values of the optical depth and of the control field, having fixed $\Delta = \Delta_s = 0$. They are coherent with the Maxwell-Bloch predictions, showing how the nonlinearity improves as we increase OD, or decrease Ω_c.

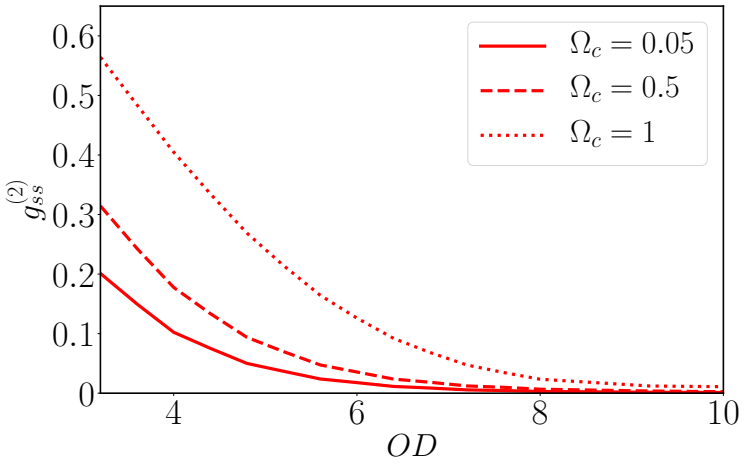

Figure 3.11: Varying of $g_{ss}^{(2)}$ with OD, for different values of Ω_c. It is assumed $\Gamma_r = 0.2$.

3.4.2 Transient analysis

While the CW case has been well-studied and understood, an interesting behavior in the second-order correlation $g^{(2)}(t)$ has recently been observed [80], which still lacks of an explanation. To illustrate, we consider a quasi-square-wave input pulse (see figure 3.12). The duration of the constant part of the pulse is long enough that $g^{(2)}(t)$ equilibrates to the steady-state value during that interval. However, in the rapid turn-on region of the pulse, $g^{(2)}(t)$ starts from a near-classical value $g^{(2)}(t) \approx 1$ and slowly decays to the steady-state value (region FT in the figure 3.12). Perhaps more interestingly, in the rapid turn-off region (EA), $g^{(2)}(t)$ *decreases* below the steady-state value, and seems to approach perfect anti-bunching $g^{(2)}(t) \to 0$ at long times. To the extent that strong anti-bunching is often associated with a large nonlinearity, our goal is to clarify the origin of these transient effects, and to understand in what sense (if any) the turn-off region of the outgoing pulse is "more quantum" or reflects stronger nonlinear interactions.

The physical origin of the decreasing behaviour of the $g^{(2)}$ in the FT region can be understood in the following way. At the beginning of the dynamics, the atoms are in the ground state. Then, the rapid turn-on of the input pulse forces them to move towards the Rydberg-EIT population of the CW regime.

However, no matter how fast the turn-on could be, the redistribution of the atomic population can never be instantaneous. It means that the coefficients of the expansion (3.40) must evolve continuously, and since at $t = 0$ we have $c_e = 0$ and $c_{ee} = 0$, the $g^{(2)}$ starts from 1. In this first transient, before that the steady state regime is reached, the amount of population in the Rydberg levels is less than the CW one, and thus also the blockade mechanism is also less effective. In appendix B, we study this transient evolution in the simplified case of a single atom.

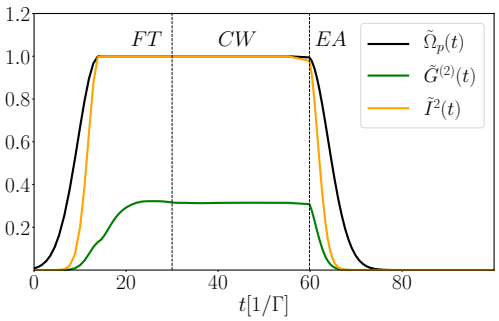

(a) Output $\tilde{I}(t)$ and $\tilde{G}^{(2)}(t)$.

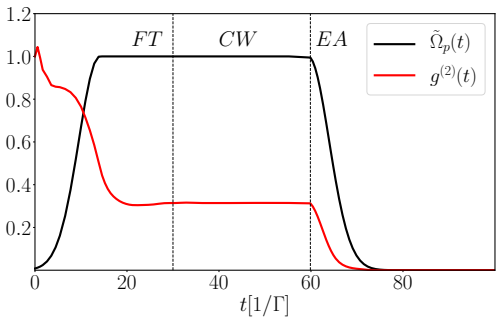

(b) Output $g^{(2)}(t)$.

Figure 3.12: Long square type pulse for $OD = 3.2$ and $\Omega_c = 0.5$. The three regions *first transient*, *CW*, and *extreme-antibunching* are visible. With $\tilde{\Omega}_p(t)$ we indicate $\Omega_p(t)$ normalized to its maximum Ω_p^{max}, $\tilde{I} = I/(\Omega_p^{max})^2$, and $\tilde{G}^{(2)} = G^{(2)}/(\Omega_p^{max})^4$. It is assumed $\Gamma_r = 0.2$.

Since $I(t)$ only depends upon the c_e coefficients and $G^{(2)}(t)$ only on the

c_{ee} ones, an idea to study the EA transient could be the splitting of the dynamics between the single-excitation subspace and the double-excitation one. In general, they are strictly intertwined, but we can construct a particular situation where the two subspaces naturally evolve separately. So we consider the following scheme: the system is initially in the steady state and then we suddenly switch the probe field off. This limit case, even if slightly different from the second transient above considered, contains the key physics of the process. The system (3.42)-(3.46) now gets divided in two, namely:

$$\dot{c}_e^n = -\frac{\Gamma}{2}c_e^n + i\Omega_c c_r^n - \frac{\Gamma_1}{2}\sum_{m\neq n} e^{ik_1|z_n - z_m|}c_e^m \tag{3.49}$$

$$\dot{c}_r^n = i\Omega_c c_e^n, \tag{3.50}$$

for the single-excitation subspace and:

$$\begin{aligned}\dot{c}_{ee}^{nm} = & -\Gamma c_{ee}^{nm} + i\Omega_c\left(c_{er}^{nm} + c_{re}^{nm}\right) - \frac{\Gamma_1}{2}\sum_{h\neq n,m} e^{ik_1|z_m - z_h|}c_{ee}^{(nh)} + \\ & -\frac{\Gamma_1}{2}\sum_{h\neq n,m} e^{ik_1|z_n - z_h|}c_{ee}^{(mh)}\end{aligned} \tag{3.51}$$

$$\begin{aligned}\dot{c}_{er}^{nm} = & -\frac{\Gamma}{2}c_{er}^{nm} + i\Omega_c c_{ee}^{nm} - \frac{\Gamma_1}{2}\sum_{\substack{h\neq n \\ h<m}} e^{ik_1|z_n - z_h|}c_{er}^{hm} + \\ & -\frac{\Gamma_1}{2}\sum_{\substack{h\neq n \\ h>m}} e^{ik_1|z_n - z_h|}c_{re}^{mh}\end{aligned} \tag{3.52}$$

$$\begin{aligned}\dot{c}_{re}^{nm} = & -\frac{\Gamma}{2}c_{re}^{nm} + i\Omega_c c_{ee}^{nm} - \frac{\Gamma_1}{2}\sum_{\substack{h\neq m \\ h>n}} e^{ik_1|z_m - z_h|}c_{re}^{nh} + \\ & -\frac{\Gamma_1}{2}\sum_{\substack{h\neq m \\ h<n}} e^{ik_1|z_m - z_h|}c_{er}^{hn},\end{aligned} \tag{3.53}$$

for the double-excitation one.

Single-excitation component

The dynamics in the single-excitation subspace is somehow analogous to the retrieving of an excitation from a quantum memory. When the quantum memory protocol is implemented (to avoid the frequency dispersion, that would

destroy the shape of the excitation) the spectrum of the incoming pulse, and so of the stored excitation, is centered on $\Delta = 0$ and well inside the EIT-band. In this case, the constant of time that characterizes the retrieving process scales as the EIT-delay time $\tau_{EIT} = \frac{OD\Gamma}{4\Omega_c^2}$. In our auxiliary situation, since we switch the probe field off instantaneously, the retrieved excitation has frequency components spread all over the ω axis.

To estimate the constant of time of this process τ_I, we solve the system (3.49)-(3.50) starting from a steady state initial condition and we compute the full width at half maximum (FWHM) time of the retrieved intensity, i.e. the interval between the two instants of time in which the output intensity crosses the half of the maximum value. We study how τ_I scales with the changing of the optical depth and of the control field in the relevant limit of high OD and low Ω_c. In the intermediate regimes the physics doesn't change, but it is less clean to visualize. For example, when $\Omega_c \sim \Gamma$, the Rabi flopping between $|e\rangle$ and $|r\rangle$ is fast enough to make some oscillating features appear in the retrieved intensity, and this hides the essence of the physics[33]. Since at the steady-state the c_e coefficients are null, $I(t)/\Omega_p^2$ drops from 1 to 0 instantaneously, then it grows fast reaching a pick whose value for high OD is greater than 1, then relaxes to the value of 1 and, eventually, goes down to 0 again at the end of the retrieving. Since the first flash of light is much faster than the timescale of the retrieving, we consider 1 as the maximum value for the retrieved intensity in the computation of the FWHM, as shown in figure 3.13. From the numerical tests, we found that τ_I, as expected, grows with the optical depth and decreases with the control fields. It particular, the scaling laws are the same of τ_{EIT}, i.e. $\tau_I \propto \frac{OD}{\Omega_c^2}$ (see figures 3.14 and 3.15). Thus, the far detuned components do not change the qualitative behaviour of the retrieving.

The maximum of the intensity higher than 1 is mirror of a superradiant behaviour determined by some steady-state constructive interference features along the chain. It can be measured when the driving field is switched off rapidly [80]. This phenomenon is known in the contest of 2-level systems, where the CW suppression of the output intensity is the product of a destructive interference between the input field and the scattered one. The suddenly switching off of the probe field brings to an instantaneous flash of light in the output intensity, generated by the scattered field, that needs some time to abandon the ensemble. The Rydberg flash that we see here, differently from

[33] Nonetheless, in real life experiments, the function $g^{(2)}(t)$ is actually measured as the average of the double-photon detection count over a time window centered around t, and so these oscillations can be averaged out if the time window is large enough.

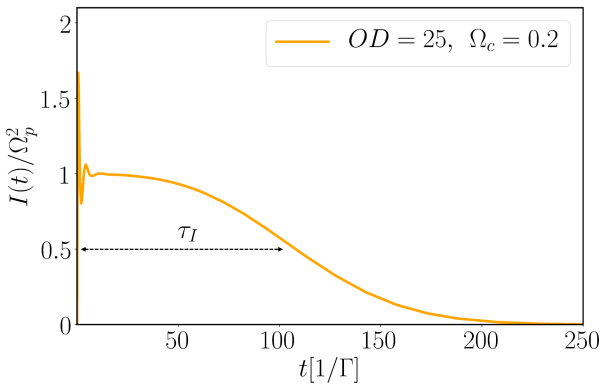

Figure 3.13: Output intensity profile obtained switching Ω_p suddenly off, starting from a steady state initial condition. It is assumed $\Gamma_r = 0.1$.

the 2-level one, doesn't appear at $t = 0$, but slightly after. This can be understood from the fact that at $t = 0$ there is no population in the excited state, and so the system needs some time to populate it. Moreover, this flash can exceed $I/\Omega_p^2 = 1$, while in the 2-level system this cannot happen.

Double-excitation component

To study how the double-excitation component diffuses away from the ensemble, we do what we have already done for the single-excitation one: we compute the FWHM of the retrieved $G^{(2)}$, in the limit of high OD and small Ω_c, starting from a steady state initial condition. Now, since in the CW regime, the c_{ee} coefficients are not null, $G^{(2)}(t)$ starts from the steady state value, that proves to be the maximum value along the dynamics, and then decays to zero. Here, the FWHM is given by the only instant of time where $G^{(2)}(t)/G^{(2)}_{ss}$ crosses $1/2$, and we refer to this constant of time as τ_{II} (see figure 3.16(a)).

We found that τ_{II} decreases as the optical depth increases. On that we can conjecture that it might depend again on some constructive interferences along the ensemble, which become more effective as the OD increases, and that helps the double-excitation to escape the medium faster. Interestingly, we also found that τ_{II} doesn't depend on the control field, for $\Omega_c \ll \Gamma$. Nonetheless, this doesn't mean that the retrieving of the double excitation component can be understood only in terms of diffusion processes in 2-level media. Indeed,

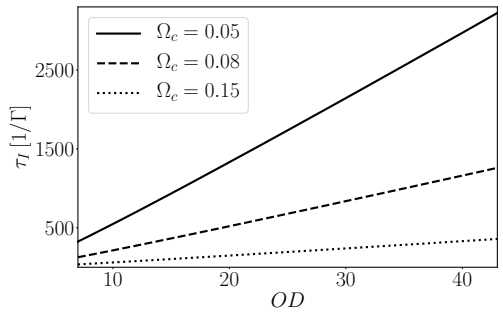

(a) Scaling of τ_I with OD for different values of Ω_c.

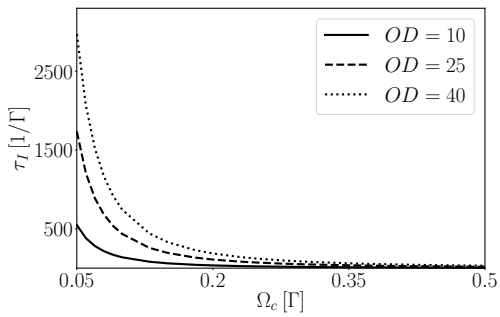

(b) Scaling of τ_I with Ω_c for different values of OD.

Figure 3.14: Scaling of τ_I with OD and Ω_c: $\tau_I \propto OD/\Omega_c^2$. $\Gamma_r = 0.1$ is assumed.

the $|er\rangle$ component of the wave function keeps on feeding the population of the $|ee\rangle$. The easy two-atom model described in appendix B can help in understanding this mechanism. Eventually, as shown in figure 3.16(b), we found that $\tau_{II} \propto \frac{1}{OD}$.

The resultant $g^{(2)}(t)$

This auxiliary scenario has shown that, after the switching off of the probe field, the intensity $I(t)$ and the second order correlation function $G^{(2)}(t)$ go to zero at two different time scales: $\tau_I \propto \frac{OD}{\Omega_c^2}$ while $\tau_{II} \propto \frac{1}{OD}$. For realistic values of Ω_c and OD, these scaling laws perfectly justify the extreme-antibunching observed in the transmission, indeed $\tau_I \gg \tau_{II}$. Moreover, this

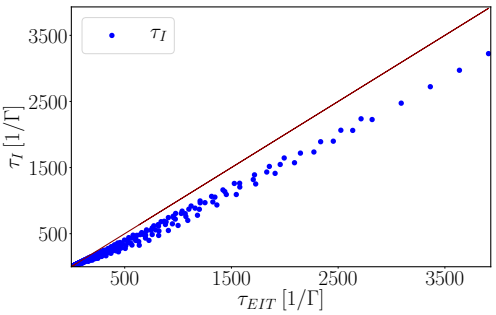

Figure 3.15: Scaling of τ_I with τ_{EIT}. Values obtained by changing OD form 7 to 43 and Ω_c from 0.05 to 0.5.

profound different dependence on the parameters of the ensemble suggests quantitative methods to tailor this extreme-antibunching at the end of the pulse. This could be an interesting perspective for the future developments of the techniques that aim to turn classical light into quantum light.

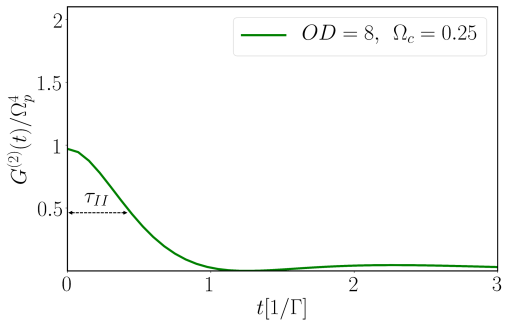

(a) Output $G^{(2)}$ profile obtained switching Ω_p suddenly off, starting from a steady state initial condition.

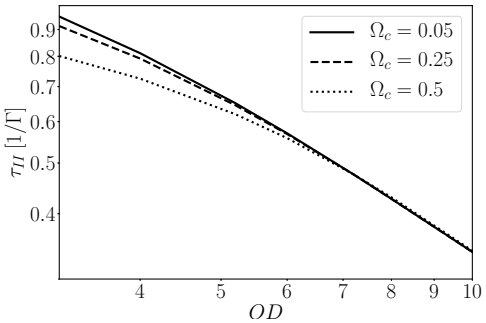

(b) Scaling of τ_{II} with OD and Ω_c: $\tau_I \propto 1/OD$. The plot is in $\log - \log$ scale.

Figure 3.16: Double excitation analysis. $\Gamma_r = 0.2$ is assumed.

Conclusions

In this thesis chapter, we have discussed the nonlinear features exhibited by a cold gas of Rybderg atoms in the electromagnetic induced transparency setup. This medium proved to be nonlinear at the few photon level, appearing transparent to individual photons and absorbing to photon couples. The suppression of the double-photon component is quantified by evaluating the antibunching of the transmitted light. The qualitative results of the CW measurements of [79], and of the transient measurements of [80], have been theoretically analyzed. The numerical tests have been carried out using the spin model in the weak driving regime on effective atomic chains, properly designed to capture

the main physics of the real 3D cigar shaped atomic clouds.

The theoretical analyses have shown that, in the CW regime, the antibunchig can be improved by trapping bigger atomic clouds or by encouraging slower propagations, in order to give the photons more time to interact. Nonetheless, motional dephasing and available experimental resources can constraint these choices and set, a priori, the lowest antibunching achievable. It has been shown that a possible way to tackle these issues is to consider pulse dynamics instead of steady state regimes. Indeed, the very end of a transmitted pulse exhibits a lower antibunching compared to the CW value. These extreme antibunching has been analyzed by considering a test scenario where the single-excitation component of the quantum state and the double-excitation one evolve separately, i.e. the suddenly switching off of the probe field, starting from a steady state initial condition. As a result, it has been shown that the two components leave the ensemble at two different time scales. Such a difference clarifies the physical origin of this peculiar extreme-antibunching, and could represent a starting point for the development of future techniques that aim to exploit this strong photon couple suppression in the quantum technology world.

Appendix A: Numerical implementation

To numerically implement the (3.41), we first have to choose a basis of the Hilbert space V to expand the quantum state $|\psi\rangle$. Then, we have to represent the fundamental operator of the Hamiltonian, e.g. σ_{ee}, σ_{ge}, ..., in this basis. For N atoms we have:

$$V = V^{(0)} + V^{(1)} + V^{(2)} + \cdots + V^{(N)} = \sum_{p=0}^{N} V^{(p)}, \tag{3.54}$$

where $V^{(p)}$ is the p-excitation subspace, whose dimension depends on the number of atomic energy levels L involved in the dynamics. For example, in the case of two-level atoms, i.e. $L = 2$, we have $dim\left[V^{(p)}\right] = \frac{N(N-1)...(N-p+1)}{p!}$. In general, we have $dim\,[V] = L^N$.

Let's focus on the cases of the main test, i.e. $L = 2$ and $L = 3$. $V^{(0)}$ has always dimension 1 and the ground state $|g\rangle$ expands the whole space. $V^{(1)}$ has dimension N for $L = 2$ and $2N$ for $L = 3$, and the natural bases for this subspace are $\{|e_n\rangle\}_n$ and $\{|e_n\rangle, |r_n\rangle\}_n$ respectively. In expanding $V^{(2)}$, we have to remember the indistinguishability of the excitation, e.g. $|e_n e_m\rangle$ and $|e_m e_n\rangle$ are the same state. Thus, $dim\left[V^{(2)}\right] = \frac{N(N-1)}{2}$ for $L = 2$ and $dim(V^{(2)}) = 4\frac{N(N-1)}{2}$ for $L = 3$; and so, to avoid repetitions, as bases of $V^{(2)}$ we choose $\{|e_1e_2\rangle, |e_1e_3\rangle, |e_2e_3\rangle, |e_1e_4\rangle, |e_2e_4\rangle, \dots\}$ for $L = 2$, and $\{|e_1e_2\rangle, |e_1e_3\rangle, \dots\ |e_1r_2\rangle, |e_1r_3\rangle, \dots, |r_1e_2\rangle, |r_1e_3\rangle, \dots, |r_1r_2\rangle, |r_1r_3\rangle, \dots\}$ for $L = 3$. The construction of the bases of the higher excitation subspaces follows the same principle.

In the weak driving regime, the Hilbert space can be truncated up to the single-excitation subspace when we want to study the linear properties of the system and up to the double-excitation one for the study of the blockade. Thus, $dim\left[V^{(0)} + V^{(1)} + V^{(2)}\right] = 1 + 2N + 2N(N-1) = q$, and we have the following expansion for the quantum state:

$$\begin{aligned} |\psi\rangle \;=\; & c_g|g\rangle + \sum_n c_e^n|e_n\rangle + \sum_n c_r^n|r_n\rangle + \sum_{\substack{n,m \\ n<m}} c_{ee}^{nm}|e_n e_m\rangle \\ & + \sum_{\substack{n,m \\ n<m}} c_{er}^{nm}|e_n r_m\rangle + \sum_{\substack{n,m \\ n<m}} c_{re}^{nm}|r_n e_m\rangle + \sum_{\substack{n,m \\ n<m}} c_{rr}^{nm}|r_n r_m\rangle \end{aligned} \tag{3.55}$$

.

To this expansion of the wave function, the following trivial representation

map is associated:

$$r : V \ni |\psi\rangle \longrightarrow r(|\psi\rangle) = \begin{bmatrix} c_g \\ c_e^1 \\ \vdots \\ c_r^1 \\ \vdots \\ c_{ee}^{12} \\ \vdots \\ c_{rr}^{N-1,N} \end{bmatrix} \in \mathbb{C}^q. \tag{3.56}$$

The map (3.56) naturally induces the following representation of the σ operators:

$$r : Aut(V) \ni \sigma \longrightarrow r(\sigma) = \begin{bmatrix} \sigma^{1,1} & \sigma^{1,2} & \dots \\ \sigma^{2,1} & \sigma^{2,1} & \dots \\ \vdots & \vdots & \vdots \end{bmatrix} \in \mathbb{C}^{q,q}. \tag{3.57}$$

Example The representation of σ_{ge}^1 when $N = 2$ is

$$r : End(V) \ni \sigma_{ge}^1 \longrightarrow r(\sigma_{ge}^1) = \begin{bmatrix} 0 & 1 & 0 & 0 & 0 & 0 & 0 & 0 & 0 \\ 0 & 0 & 0 & 0 & 0 & 0 & 0 & 0 & 0 \\ 0 & 0 & 0 & 0 & 0 & 1 & 0 & 0 & 0 \\ 0 & 0 & 0 & 0 & 0 & 0 & 0 & 0 & 0 \\ 0 & 0 & 0 & 0 & 0 & 0 & 1 & 0 & 0 \\ 0 & 0 & 0 & 0 & 0 & 0 & 0 & 0 & 0 \\ 0 & 0 & 0 & 0 & 0 & 0 & 0 & 0 & 0 \\ 0 & 0 & 0 & 0 & 0 & 0 & 0 & 0 & 0 \\ 0 & 0 & 0 & 0 & 0 & 0 & 0 & 0 & 0 \end{bmatrix} \in \mathbb{C}^{9,9}, \tag{3.58}$$

since $\sigma_{ge}^1|\psi\rangle \neq 0$ only if the first atom is excited. Indeed, we have:

$$\begin{bmatrix} 0 & 1 & 0 & 0 & 0 & 0 & 0 & 0 & 0 \\ 0 & 0 & 0 & 0 & 0 & 0 & 0 & 0 & 0 \\ 0 & 0 & 0 & 0 & 0 & 1 & 0 & 0 & 0 \\ 0 & 0 & 0 & 0 & 0 & 0 & 0 & 0 & 0 \\ 0 & 0 & 0 & 0 & 0 & 0 & 1 & 0 & 0 \\ 0 & 0 & 0 & 0 & 0 & 0 & 0 & 0 & 0 \\ 0 & 0 & 0 & 0 & 0 & 0 & 0 & 0 & 0 \\ 0 & 0 & 0 & 0 & 0 & 0 & 0 & 0 & 0 \\ 0 & 0 & 0 & 0 & 0 & 0 & 0 & 0 & 0 \end{bmatrix} \begin{bmatrix} c_g \\ c_e^1 \\ c_e^2 \\ c_r^1 \\ c_r^2 \\ c_{ee}^{12} \\ c_{er}^{12} \\ c_{re}^{12} \\ c_{rr}^{12} \end{bmatrix} = \begin{bmatrix} c_e^1 \\ 0 \\ c_{ee}^{12} \\ 0 \\ c_{er}^{12} \\ 0 \\ 0 \\ 0 \\ 0 \end{bmatrix}. \tag{3.59}$$

Appendix B :some easy analytics

Here we want to compute some easy analytics that can help in understanding the complex many-atom transient dynamics described in the main text.

First transient analysis for a single atom. We have seen that, at the beginning of the pulse, the $g^{(2)}(t) \sim 1$ and then it goes down to the steady state value. We have motivated this behaviour observing that, in this regime, the blockade phenomenon is not at its best, since the atoms need some time to exhibit the atomic EIT population we look for. This can be understood even at the single atom level where we have that (even assuming at $\Delta_s = \Delta = 0$) at the beginning of the dynamics $c_e \neq 0$. Indeed, from:

$$\dot{c}_e = -\frac{\Gamma}{2}c_e + i\Omega_c c_r + i\Omega_p \tag{3.60}$$

$$\dot{c}_r = i\Omega_c c_e, \tag{3.61}$$

we have:

$$\ddot{c}_e + \frac{\Gamma}{2}\dot{c}_e + \Omega_c^2 c_e = i\dot{\Omega}_p \quad \text{or} \quad \ddot{c}_r + \frac{\Gamma}{2}\dot{c}_r + \Omega_c^2 c_r = -\Omega_c\Omega_p. \tag{3.62}$$

From (3.62) we see that, while the population in the Rydberg level depends on the amplitude of the probe field, the one in the excited state is driven by its variations. In the first transient, the population in the excited state is not zero and the population in the Rydberg state, even at the single excitation level, is not maximum and, thus, we imagine that the corresponding blockade is not so effective. Since the natural frequencies of the (3.62) are $\lambda_{1,2} = -\frac{\Gamma}{4} \pm \frac{\mu}{2}$, with $\mu^2 = 4\Omega_c^2 - (\Gamma/2)^2$, the time scale of this single atom transient is given by $\Gamma/2$ (the intensities depend on the square module of c_e).

Extreme-antibunching for two atoms. We have seen that, at the end of the pulse, $g^{(2)}(t)$ exhibits an extreme-antibunched behaviour. The analysis of the transient in the simplified two-atom case can give some good insights of the physics of the phenomenon. The steady state system in the two-atom case, assuming $z_1 = \lambda/4$ and $z_2 = \lambda/2$, and defining $\tilde{c}_{er} = (c_{er} + c_{re})/2$, reduces to:

$$0 = -\Gamma c_{ee} + 2i\Omega_c \tilde{c}_{er} \tag{3.63}$$

$$0 = -\frac{\Gamma}{2}\tilde{c}_{er} + i\Omega_c c_{ee} - \frac{\Omega_p^2}{\Omega_c}, \tag{3.64}$$

and from it we derive $c_{ee} = -\frac{4i\Omega_p^2}{\Gamma^2 + 4\Omega_c^2}$. Now, when at $t = \bar{t}$, we switch Ω_p

suddenly off, the system (3.51)-(3.53) reads:

$$\dot{c}_{ee} = -\Gamma c_{ee} + 2i\Omega_c \tilde{c}_{er} \tag{3.65}$$

$$\dot{\tilde{c}}_{er} = -\frac{\Gamma}{2}\tilde{c}_{er} + i\Omega_c c_{ee}, \tag{3.66}$$

and from it we have:

$$\ddot{c}_{ee} + \frac{3\Gamma}{2}\dot{c}_{ee} + \left(\frac{\Gamma^2}{2} + 2\Omega_c^2\right) c_{ee} = 0. \tag{3.67}$$

The (3.67) must be solved with the initial conditions $c_{ee}(\bar{t}^+) = c_{ee}(\bar{t}^-) = -\frac{4i\Omega_p^2}{\Gamma^2+4\Omega_c^2}$ and $\dot{c}_{ee}(\bar{t}^+) = \dot{c}_{ee}(\bar{t}^-) = 0$, since these quantities must evolve continuously. Thus, we have

$$c_{ee}(t) = 4i\frac{\Omega_p^2}{\Gamma^2}\left(e^{-\Gamma t} - 2e^{-\frac{\Gamma}{2}t}\right), \tag{3.68}$$

and so:

$$G^{(2)}(t)/\Omega_p^4 = \left|-i\frac{\Gamma_1^2}{2}c_{ee}\right|^2 = 4\Gamma_1^4\left|e^{-\Gamma t} - 2e^{-\frac{\Gamma}{2}t}\right|^2. \tag{3.69}$$

Let's notice that from this easy example we can understand why τ_{II}, for Ω_c sufficiently small, doesn't depend on Ω_c. Indeed, when $4\Omega_c^2 \ll \Gamma$, eq. (3.67) becomes:

$$\ddot{c}_{ee} + \frac{3\Gamma}{2}\dot{c}_{ee} + \frac{\Gamma^2}{2}c_{ee} = 0. \tag{3.70}$$

Now, even if in equation (3.70) all the traces of the 3-level structure have disappeared, the problem hasn't been reduced to a 2-level scenario: the third level is still there keeping on feeding the population of the excited states. Indeed, solving the 3-level dynamics (and then observing that for Ω_c sufficiently small the result is independent of it) is deeply different from zeroing Ω_c directly in the (3.65)-(3.66), that would simply lead to $c_{ee}(t) = e^{-\Gamma t}c_{ee}(\bar{t})$.

Bibliography

[1] G.W. Hanson and A.B. Yakovlev. *Operator Theory for Electromagnetics: An Introduction*. Springer New York, 2013.

[2] ESC Ching, PT Leung, A Maassen van den Brink, WM Suen, SS Tong, and K Young. Quasinormal-mode expansion for waves in open systems. *Reviews of Modern Physics*, 70(4):1545, 1998.

[3] Philip Trøst Kristensen and Stephen Hughes. Modes and Mode Volumes of Leaky Optical Cavities and Plasmonic Nanoresonators. *ACS Photonics*, 1(1):2–10, Jan 2014.

[4] Philippe Lalanne, Wei Yan, Kevin Vynck, Christophe Sauvan, and Jean-Paul Hugonin. Light Interaction with Photonic and Plasmonic Resonances. *Laser & Photonics Reviews*, 12(5):1700113, May 2018.

[5] Robert J. Garbacz. Modal Expansions for Resonance Scattering Phenomena. *Proceedings of the IEEE*, 53(8):856–864, 1965.

[6] C. Sauvan, J. P. Hugonin, I. S. Maksymov, and P. Lalanne. Theory of the Spontaneous Optical Emission of Nanosize Photonic and Plasmon Resonators. *Phys. Rev. Lett.*, 110(23):237401, Jun 2013.

[7] Philip Trøst Kristensen, Rong-Chun Ge, and Stephen Hughes. Normalization of quasinormal modes in leaky optical cavities and plasmonic resonators. *Phys. Rev. A*, 92(5):053810, Nov 2015.

[8] David J. Bergman and D. Stroud. Theory of resonances in the electromagnetic scattering by macroscopic bodies. *Phys. Rev. B*, 22(8):3527–3539, 1980.

[9] Carlo Forestiere and Giovanni Miano. Material-independent modes for electromagnetic scattering. *Phys. Rev. B*, 94(20):201406, Nov 2016.

[10] R. Fuchs. Theory of the optical properties of ionic crystal cubes. *Phys. Rev. B*, 11(4):1732–1740, Feb 1975.

[11] R. Rojas and F. Claro. Electromagnetic response of an array of particles: Normal-mode theory. *Phys. Rev. B*, 34(6):3730–3736, Sep 1986.

[12] David J Bergman. The dielectric constant of a composite material—a problem in classical physics. *Physics Reports*, 43(9):377–407, 1978.

[13] D. R. Fredkin and I. D. Mayergoyz. Resonant behavior of dielectric objects (electrostatic resonances). *Phys. Rev. Lett.*, 91(25):253902, 2003.

[14] Isaak D. Mayergoyz, Donald R. Fredkin, and Zhenyu Zhang. Electrostatic (plasmon) resonances in nanoparticles. *Phys. Rev. B*, 72(15):155412, Oct 2005.

[15] Vadim A Markel. Pole expansion of the Lorenz-Mie coefficients. *Journal of Nanophotonics*, 4(1):041555, 2010.

[16] Carlo Forestiere, Giovanni Miano, Gugliemo Rubinacci, and Luca Dal Negro. Role of aperiodic order in the spectral, localization, and scaling properties of plasmon modes for the design of nanoparticle arrays. *Phys. Rev. B*, 79(8):085404, Feb 2009.

[17] Vadim A. Markel. Antisymmetrical optical states. *J. Opt. Soc. Am. B*, 12(10):1783–1791, Oct 1995.

[18] Mariano Pascale, Giovanni Miano, and Carlo Forestiere. Spectral theory of electromagnetic scattering by a coated sphere. *JOSA B*, 34(7):1524, Jul 2017.

[19] Carlo Forestiere, Giovanni Miano, Mariano Pascale, and Roberto Tricarico. A Full-Retarded Spectral Technique for the Analysis of Fano Resonances in a Dielectric Nanosphere. In *Kamenetskii E., Sadreev A., Miroshnichenko A. (eds) Fano Resonances in Optics and Microwaves. Springer Series in Optical Sciences*, volume 219. Nov 2018.

[20] Carlo Forestiere, Giovanni Miano, Mariano Pascale, and Roberto Tricarico. Electromagnetic Scattering Resonances of Quasi-1-D Nanoribbons. *IEEE Transactions on Antennas and Propagation*, 67(8):5497–5506, Aug 2019.

[21] Asaf Farhi and David J Bergman. Electromagnetic eigenstates and the field of an oscillating point electric dipole in a flat-slab composite structure. *Phys. Rev. A*, 93(6):063844, 2016.

[22] Carlo Forestiere, Giovanni Gravina, Giovanni Miano, Mariano Pascale, and Roberto Tricarico. Electromagnetic modes and resonances of two-dimensional bodies. *Phys. Rev. B*, 99(15):155423, Apr 2019.

[23] Mariano Pascale, Giovanni Miano, and Carlo Forestiere. Spectral theory of electromagnetic scattering by a coated sphere. *JOSA B*, 34(7):1524–1535, 2017.

[24] Carlo Forestiere and Giovanni Miano. On the nanoparticle resonances in the full-retarded regime. *J. Opt.*, 19(7):075601, jun 2017.

[25] I.D. Mayergoyz. *Plasmon Resonances in Nanoparticles*. World Scientific series in nanoscience and nanotechnology. World Scientific, 2013.

[26] Carlo Forestiere, Giovanni Miano, Guglielmo Rubinacci, Mariano Pascale, Antonello Tamburrino, Roberto Tricarico, and Salvatore Ventre. Magnetoquasistatic resonances of small dielectric objects. *Phys. Rev. Research*, 2(1):013158, Feb 2020.

[27] Cessenat Michel. *Mathematical Methods In Electromagnetism: Linear Theory And Applications*. Series On Advances In Mathematics For Applied Sciences. World Scientific Publishing Company, 1996.

[28] C.F. Bohren and D.R. Huffman. *Absorption and Scattering of Light by Small Particles*. Wiley Science Series. John Wiley & Sons, 2008.

[29] Uwe Kreibig and Michael Vollmer. *Optical properties of metal clusters*, volume 25 of *Springer Series in Materials Science*. Springer, 1995.

[30] S.A. Maier. *Plasmonics: Fundamentals and Applications*. Springer US, 2007.

[31] Carlo Forestiere, Giovanni Miano, Mariano Pascale, and Roberto Tricarico. Directional scattering cancellation for an electrically large dielectric sphere. *Optics Letters*, 44(8):1972–1975, Apr 2019.

[32] Mariano Pascale, Giovanni Miano, Roberto Tricarico, and Carlo Forestiere. Full-wave electromagnetic modes and hybridization in nanoparticle dimers. *Sci. Reports*, 9(1):14524, Oct 2019.

[33] Carlo Forestiere, Giovanni Miano, Guglielmo Rubinacci, Antonello Tamburrino, Roberto Tricarico, and Salvatore Ventre. Volume Integral Formulation for the Calculation of Material Independent Modes of Dielectric Scatterers. *IEEE Transactions on Antennas and Propagation*, 66(5):2505–2514, May 2018.

[34] Yajie Jiang, Supriya Pillai, and Martin A. Green. Realistic Silver Optical Constants for Plasmonics. *Sci. Reports*, 6(1):30605, Jul 2016.

[35] Arseniy I. Kuznetsov, Andrey E. Miroshnichenko, Yuan Hsing Fu, JingBo Zhang, and Boris Luk'yanchuk. Magnetic light. *Sci. Reports*, 2(1):492, 2012.

[36] M. Kerker, D. S. Wang, and C. L. Giles. Electromagnetic scattering by magnetic spheres. *JOSA*, 73(6):765–767, 1983.

[37] M. Nieto-Vesperinas, R. Gomez-Medina, and J. J. Saenz. Angle-suppressed scattering and optical forces on submicrometer dielectric particles. *JOSA A*, 28(1):54, Jan 2011.

[38] J. M. Geffrin, B. García-Cámara, R. Gómez-Medina, P. Albella, L. S. Froufe-Pérez, C. Eyraud, A. Litman, R. Vaillon, F. González, M. Nieto-Vesperinas, J. J. Sáenz, and F. Moreno. Magnetic and electric coherence in forward-and back-scattered electromagnetic waves by a single dielectric subwavelength sphere. *Nature Communications*, 3(1):1171, 2012.

[39] Yuan Hsing Fu, Arseniy I. Kuznetsov, Andrey E. Miroshnichenko, Ye Feng Yu, and Boris Luk'yanchuk. Directional visible light scattering by silicon nanoparticles. *Nature Communications*, 4(1):1527, 2013.

[40] Steven Person, Manish Jain, Zachary Lapin, Juan Jose Sáenz, Gary Wicks, and Lukas Novotny. Demonstration of Zero Optical Backscattering from Single Nanoparticles. *Nano Lett.*, 13(4):1806–1809, Mar 2013.

[41] Brice Rolly, Brian Stout, and Nicolas Bonod. Boosting the directivity of optical antennas with magnetic and electric dipolar resonant particles. *Opt. Express*, 20(18):20376–20386, Aug 2012.

[42] Wei Liu, Andrey E. Miroshnichenko, Dragomir N. Neshev, and Yuri S. Kivshar. Broadband unidirectional scattering by magneto-electric core–shell nanoparticles. *ACS Nano*, 6(6):5489–5497, 2012.

[43] Wei Liu, Andrey E Miroshnichenko, Rupert F Oulton, Dragomir N Neshev, Ortwin Hess, and Yuri S Kivshar. Scattering of core-shell nanowires with the interference of electric and magnetic resonances. *Optics letters*, 38(14):2621–2624, 2013.

[44] Isabelle Staude, Andrey E. Miroshnichenko, Manuel Decker, Nche T. Fofang, Sheng Liu, Edward Gonzales, Jason Dominguez, Ting Shan Luk, Dragomir N. Neshev, Igal Brener, and Yuri Kivshar. Tailoring Directional Scattering through Magnetic and Electric Resonances in Subwavelength Silicon Nanodisks. *ACS Nano*, 7(9):7824–7832, 2013.

[45] X. Zambrana-Puyalto, I. Fernandez-Corbaton, M. L. Juan, X. Vidal, and G. Molina-Terriza. Duality symmetry and Kerker conditions. *Opt. Lett.*, 38(11):1857–1859, Jun 2013.

[46] R. Alaee, R. Filter, D. Lehr, F. Lederer, and C. Rockstuhl. A generalized Kerker condition for highly directive nanoantennas. *Opt. Lett.*, 40(11):2645–2648, Jun 2015.

[47] Wei Liu, Jianfa Zhang, Bing Lei, Haotong Ma, Wenke Xie, and Haojun Hu. Ultra-directional forward scattering by individual core-shell nanoparticles. *Opt. Express*, 22(13):16178–16187, Jun 2014.

[48] A. Doicu, T. Wriedt, and Y.A. Eremin. *Light Scattering by Systems of Particles. Null-Field Method with Discrete Sources: Theory and Programs*. Springer-Verlag, 2006.

[49] M. S. Tame, K. R. McEnery, Ş K. Özdemir, J. Lee, S. A. Maier, and M. S. Kim. Quantum plasmonics. *Nature Physics*, 9(6):329–340, June 2013.

[50] Huakang Yu, Yusi Peng, Yong Yang, and Zhi Yuan Li. Plasmon-enhanced light–matter interactions and applications. *npj Comput Mater*, 5(1):45, Apr 2019.

[51] Darrick E. Chang, Anders S. Sørensen, Eugene A. Demler, and Mikhail D. Lukin. A single-photon transistor using nanoscale surface plasmons. *Nature Physics*, 3(11):807–812, Aug 2007.

[52] A. Femius Koenderink. Plasmon Nanoparticle Array Waveguides for Single Photon and Single Plasmon Sources. *Nano Lett.*, 9(12):4228–4233, Dec 2009.

[53] Gülis Zengin, Martin Wersäll, Sara Nilsson, Tomasz J. Antosiewicz, Mikael Käll, and Timur Shegai. Realizing strong light-matter interactions between single-nanoparticle plasmons and molecular excitons at ambient conditions. *Phys. Rev. Lett.*, 114(15):157401, Apr 2015.

[54] E. M. Purcell, H. C. Torrey, and R. V. Pound. Resonance absorption by nuclear magnetic moments in a solid. *Phys. Rev.*, 69(1-2):37, Jan 1946.

[55] A. F. Koenderink. On the use of Purcell factors for plasmon antennas. *Optics Letters*, 35(24):4208–4210, 2010.

[56] Roman Kolesov, Bernhard Grotz, Gopalakrishnan Balasubramanian, Rainer J. Stöhr, Aurélien A.L. Nicolet, Philip R. Hemmer, Fedor Jelezko, and Jörg Wrachtrup. Wave-particle duality of single surface plasmon polaritons. *Nature Physics*, 5(7):470–474, May 2009.

[57] Marie-Christine Dheur, Jean-Jacques Greffet, Gaétan Messin, Eloise Devaux, Philippe Lalanne, Thomas Ebbesen, and François Marquier. Wave-particle duality of single surface plasmon polaritons. In *Advanced Photonics 2015*. OSA Technical Digest (online) (Optical Society of America, 2015), paper IS3A.2.

[58] E. Altewischer, M. P. Van Exter, and J. P. Woerdman. Plasmon-assisted transmission of entangled photons. *Nature*, 418(6895):304–306, Jul 2002.

[59] Sylvain Fasel, Franck Robin, Esteban Moreno, Daniel Erni, Nicolas Gisin, and Hugo Zbinden. Energy-time entanglement preservation in plasmon-assisted light transmission. *Phys. Rev. Lett.*, 94(11):110501, Mar 2005.

[60] A. V. Akimov, A. Mukherjee, C. L. Yu, D. E. Chang, A. S. Zibrov, P. R. Hemmer, H. Park, and M. D. Lukin. Generation of single optical plasmons in metallic nanowires coupled to quantum dots. *Nature*, 450(7168):402–406, Nov 2007.

[61] David Pines. A collective description of electron interactions: IV. Electron interaction in metals. *Phys. Rev.*, 92(3):626–636, Nov 1953.

[62] J. J. Hopfield. Theory of the contribution of excitons to the complex dielectric constant of crystals. *Phys. Rev.*, 112(5):1555, Dec 1958.

[63] Julian Crowell and R. H. Ritchie. Radiative decay of coulomb-stimulated plasmons in spheres. *Phys. Rev.*, 172(2):436–440, Aug 1968.

[64] Y. O. Nakamura. Quantization of Non-Radiative Surface Plasma Oscillations. *Progress of Theoretical Physics*, 70(4):908–919, Oct 1983.

[65] Joel Gersten and Abraham Nitzan. Spectroscopic properties of molecules interacting with small dielectric particles. *The Journal of Chemical Physics*, 75(3):1139–1152, 1981.

[66] Andreas Trügler and Ulrich Hohenester. Strong coupling between a metallic nanoparticle and a single molecule. *Phys. Rev. B*, 77(11):115403, Mar 2008.

[67] Edo Waks and Deepak Sridharan. Cavity QED treatment of interactions between a metal nanoparticle and a dipole emitter. *Phys. Rev. A*, 82(4):043845, Oct 2010.

[68] T. G. Philbin. Canonical quantization of macroscopic electromagnetism. *New Journal of Physics*, 12(12):123008, Dec 2010.

[69] E. S. Andrianov, A. A. Pukhov, A. P. Vinogradov, A. V. Dorofeenko, and A. A. Lisyansky. Spontaneous radiation of a two-level atom into multipole modes of a plasmonic nanoparticle. *Photonics and Nanostructures - Fundamentals and Applications*, 12(5):387–397, Nov 2014.

[70] Filippo Alpeggiani and Lucio Claudio Andreani. Quantum Theory of Surface Plasmon Polaritons: Planar and Spherical Geometries. *Plasmonics*, 9(4):965–978, Apr 2014.

[71] Tomáš Neuman, Ruben Esteban, David Casanova, Francisco J. García-Vidal, and Javier Aizpurua. Coupling of Molecular Emitters and Plasmonic Cavities beyond the Point-Dipole Approximation. *Nano Lett.*, 18(4):2358–2364, Apr 2018.

[72] Sebastian Franke, Stephen Hughes, Mohsen Kamandar Dezfouli, Philip Trøst Kristensen, Kurt Busch, Andreas Knorr, and Marten Richter. Quantization of Quasinormal Modes for Open Cavities and Plasmonic Cavity Quantum Electrodynamics. *Phys. Rev. Lett.*, 122(21):213901, May 2019.

[73] Ho Trung Dung, Ludwig Knöll, and Dirk-Gunnar Welsch. Three-dimensional quantization of the electromagnetic field in dispersive and absorbing inhomogeneous dielectrics. *Phys. Rev. A*, 57(5):3931–3942, May 1998.

[74] Carlo Forestiere, Giovanni Miano, Mariano Pascale, and Roberto Tricarico. Quantum Theory of Radiative Decay Rate and Frequency Shift of Surface Plasmons Modes in Arbitrarily Shaped Nanoparticles. *arXiv:2001.11926*, Jan 2020.

[75] M.O. Scully and M.S. Zubairy. *Quantum Optics*. Cambridge University Press, 1997.

[76] G.D. Mahan. *Many Particles Physics, 3E*. Physics of Solids and Liquids. Springer (India) Pvt. Limited, 2008.

[77] A.L. Fetter and J.D. Walecka. *Quantum Theory of Many-particle Systems*. Dover Books on Physics. Dover Publications, 2003.

[78] C. Cohen-Tannoudji, J. Dupont-Roc, and G. Grynberg. *Photons and Atoms: Introduction to Quantum Electrodynamics*. Wiley, 1997.

[79] Thibault Peyronel, Ofer Firstenberg, Qi-Yu Liang, Sebastian Hofferberth, Alexey V. Gorshkov, Thomas Pohl, Mikhail D. Lukin, and Vladan Vuletić. Quantum nonlinear optics with single photons enabled by strongly interacting atoms. *Nature*, 488(7409):57–60, Aug 2012.

[80] Charles Möhl, Nicholas L. R. Spong, Yuechun Jiao, Chloe So, Teodora Ilieva, Matthias Weidemüller, and Charles S Adams. Photon correlation transients in a weakly blockaded rydberg ensemble. *Journal of Physics B: Atomic, Molecular and Optical Physics*, Feb 2020.

[81] Darrick E. Chang, Vladan Vuletić, and Mikhail D. Lukin. Quantum nonlinear optics - Photon by photon. *Nature Photonics*, 8(9):685–694, Aug 2014.

[82] B. Darquié, M. P.A. Jones, J. Dingjan, J. Beugnon, S. Bergamini, Y. Sortais, G. Messin, A. Browaeys, and P. Grangier. Controlled single-photon emission from a single trapped two-level atom. *Science*, 309(5733):454–456, Jul 2005.

[83] Meng Khoon Tey, Zilong Chen, Syed Abdullah Aljunid, Brenda Chng, Florian Huber, Gleb Maslennikov, and Christian Kurtsiefer. Strong interaction between light and a single trapped atom without the need for a cavity. *Nature Physics*, 4(12):924–927, Oct 2008.

[84] K. M. Birnbaum, A. Boca, R. Miller, A. D. Boozer, T. E. Northup, and H. J. Kimble. Photon blockade in an optical cavity with one trapped atom. *Nature*, 436(7047):87–90, Jul 2005.

[85] Nikola Šibalić and Charles S Adams. *Rydberg physics*. IOP Publishing, Nov 2018.

[86] T.F. Gallagher. *Rydberg Atoms*. Cambridge Monographs on Atomic, Molecular and Chemical Physics. Cambridge University Press, 2005.

[87] A. Dalgarno and W. D. Davison. The Calculation of Van Der Waals Interactions. *Advances in Atomic and Molecular Physics*, 2:1–32, 1966.

[88] Mark Fox. *Quantum Optics: An Introduction*. Oxford University Press, 2006.

[89] Inbal Friedler, David Petrosyan, Michael Fleischhauer, and Gershon Kurizki. Long-range interactions and entanglement of slow single-photon pulses. *Phys. Rev. A*, 72(4):043803, Oct 2005.

[90] Alexey V. Gorshkov, Johannes Otterbach, Michael Fleischhauer, Thomas Pohl, and Mikhail D. Lukin. Photon-photon interactions via Rydberg blockade. *Phys. Rev. Lett.*, 107(13):133602, Sep 2011.

[91] Y. O. Dudin and A. Kuzmich. Strongly interacting Rydberg excitations of a cold atomic gas. *Science*, 336(6083):887–889, May 2012.

[92] Hannes Bernien, Sylvain Schwartz, Alexander Keesling, Harry Levine, Ahmed Omran, Hannes Pichler, Soonwon Choi, Alexander S. Zibrov, Manuel Endres, Markus Greiner, Vladan Vuletić, and Mikhail D. Lukin. Probing many-body dynamics on a 51-atom quantum simulator. *Nature*, 551(7682):579–584, Nov 2017.

[93] Haoquan Fan, Santosh Kumar, Jonathon Sedlacek, Harald Kübler, Shaya Karimkashi, and James P Shaffer. Atom based RF electric field sensing. *Journal of Physics B: Atomic, Molecular and Optical Physics*, 48(20):202001, Sep 2015.

[94] A. Asenjo-Garcia, J. D. Hood, D. E. Chang, and H. J. Kimble. Atom-light interactions in quasi-one-dimensional nanostructures: A Green's-function perspective. *Phys. Rev. A*, 95(3):033818, Mar 2017.

[95] Dibyendu Roy, C. M. Wilson, and Ofer Firstenberg. Colloquium: Strongly interacting photons in one-dimensional continuum. *Reviews of Modern Physics*, 89(2):021001, May 2017.

[96] D. E. Chang, L. Jiang, A. V. Gorshkov, and H. J. Kimble. Cavity QED with atomic mirrors. *New Journal of Physics*, 14(6):063003, Jun 2012.

[97] A. Asenjo-Garcia, M. Moreno-Cardoner, A. Albrecht, H. J. Kimble, and D. E. Chang. Exponential improvement in photon storage fidelities using subradiance and "selective radiance" in atomic arrays. *Phys. Rev. X*, 7(3):031024, Aug 2017.

[98] M. Fleischhauer and M. D. Lukin. Dark-state polaritons in electromagnetically induced transparency. *Phys. Rev. Lett.*, 84(22):5094–5097, May 2000.

[99] M. Fleischhauer and M. D. Lukin. Quantum memory for photons: Dark-state polaritons. *Phys. Rev. A*, 65(2):022314, Jan 2002.

[100] Lene Vestergaard Hau, S. E. Harris, Zachary Dutton, and Cyrus H. Behroozi. Light speed reduction to 17 metres per second in an ultracold atomic gas. *Nature*, 397(6720):594–598, Feb 1999.

[101] R. Bonifacio. Theory of Optical Maser Amplifiers. *IEEE Journal of Quantum Electronics*, 1(4):169–178, Jul 1965.

[102] S. L. McCall and E. L. Hahn. Self-induced transparency by pulsed coherent light. *Phys. Rev. Lett.*, 18(21):908–911, May 1967.

[103] Alexey V. Gorshkov, Axel André, Michael Fleischhauer, Anders S. Sørensen, and Mikhail D. Lukin. Universal approach to optimal photon storage in atomic media. *Phys. Rev. Lett.*, 98(12):123601, Mar 2007.

[104] Klemens Hammerer, Anders S. Sørensen, and Eugene S. Polzik. Quantum interface between light and atomic ensembles. *Reviews of Modern Physics*, 82(2):1041–1093, Apr 2010.

[105] Ho Trung Dung, Ludwig Knöll, and Dirk Gunnar Welsch. Resonant dipole-dipole interaction in the presence of dispersing and absorbing surroundings. *Phys. Rev. A*, 66(6):063810, 2002.

[106] S.Y. Buhmann. *Dispersion Forces I: Macroscopic Quantum Electrodynamics and Ground-State Casimir, Casimir-Polder and van der Waals Forces*. Springer Tracts in Modern Physics. Springer Berlin Heidelberg, 2013.

[107] Roy J. Glauber and M. Lewenstein. Quantum optics of dielectric media. *Phys. Rev. A*, 43(1):467–491, Jan 1991.

[108] M. Gross and S. Haroche. Superradiance: An essay on the theory of collective spontaneous emission. *Physics Reports*, 93(5):301–396, Dec 1982.

[109] Tommaso Caneva, Marco T. Manzoni, Tao Shi, James S. Douglas, J. Ignacio Cirac, and Darrick E. Chang. Quantum dynamics of propagating photons with strong interactions: a generalized input–output formalism. *New Journal of Physics*, 17(11):113001, Oct 2015.

[110] Navin A.R. Bhat and J. E. Sipe. Hamiltonian treatment of the electromagnetic field in dispersive and absorptive structured media. *Phys. Rev. A*, 73(6):063808, Jun 2006.

[111] Shanshan Xu and Shanhui Fan. Input-output formalism for few-photon transport: A systematic treatment beyond two photons. *Phys. Rev. A*, 91(4):043845, Apr 2015.

[112] Tao Shi, Darrick E. Chang, and J. Ignacio Cirac. Multiphoton-scattering theory and generalized master equations. *Phys. Rev. A*, 92(5):053834, Nov 2015.

[113] R. J. Thompson, G. Rempe, and H. J. Kimble. Observation of normal-mode splitting for an atom in an optical cavity. *Phys. Rev. Lett.*, 68(8):1132–1135, 1992.

[114] Sajeev John and Tran Quang. Spontaneous emission near the edge of a photonic band gap. *Phys. Rev. A*, 50(2):1764–1769, Aug 1994.

[115] A. G. Kofman, G. Kurizki, and B. Sherman. Spontaneous and induced atomic decay in photonic band structures. *Journal of Modern Optics*, 41(2):353–384, Feb 1994.

[116] J. S. Douglas, H. Habibian, C. L. Hung, A. V. Gorshkov, H. J. Kimble, and D. E. Chang. Quantum many-body models with cold atoms coupled to photonic crystals. *Nature Photonics*, 9(5):326–331, Apr 2015.

[117] Giuseppe Calajó, Francesco Ciccarello, Darrick Chang, and Peter Rabl. Atom-field dressed states in slow-light waveguide QED. *Phys. Rev. A*, 93(3):033833, Mar 2016.

[118] T. Gruner and D. G. Welsch. Green-function approach to the radiation-field quantization for homogeneous and inhomogeneous Kramers-Kronig dielectrics. *Phys. Rev. A*, 53(3):1818–1829, Mar 1996.

[119] Jonathan D. Hood, Akihisa Goban, Ana Asenjo-Garcia, Mingwu Lu, Su Peng Yu, Darrick E. Chang, and H. J. Kimble. Atom-atom interactions around the band edge of a photonic crystal waveguide. *Proceedings of the National Academy of Sciences of the United States of America*, 113(38):10507–10512, Aug 2016.

[120] Vadim A. Markel and Andrey K. Sarychev. Propagation of surface plasmons in ordered and disordered chains of metal nanospheres. *Phys. Rev. B*, 75(8):085426, Feb 2007.